UNIVERSITY OF NAPLES FEDERICO II

DEPARTMENT OF INDUSTRIAL ENGINEERING

- MECHANIC AND ENERGETIC SECTION -

PH.D. SCHOOL IN INDUSTRIAL ENGINEERING – XXXV CYCLE

MIL/HIL SIMULATIONS:

METHODOLOGIES FOR CHECK AND VALIDATION OF SYSTEMS FOR AUTONOMOUS DRIVING

Doctoral Thesis

Ph.D. School Coordinator
prof. Michele Grassi

Academic supervisors:
prof. Renato Brancati
prof. Alfredo Gimelli

Industrial supervisor:
ing. Donato Amoroso (Stellantis N.V.)

International cooperation supervisor:
prof. Simone Battistini (Sheffield Hallam University)

Ph.D. Candidate
Francesco Tufano

Abstract

The innovation in the automotive field due to the Fourth Industrial Revolution pushed towards the integration in vehicles of mechatronic systems. Indeed, while safety systems, such as the electronic stability program, have pioneered the automation of cars, recent advances in the field of electronics have fuelled an increase in this trend. So intelligent transportation systems, advanced driver assistance systems, vehicle handling stability and active safety have increasingly been promoted. However, their implementation depends on accurate vehicle dynamics state information, including those such as the vehicle sideslip angle and the tire inflation pressure, that cannot be measured directly for technical and economical reasons. The thesis is dedicated to the development and testing of algorithms for the estimation of these variables. In particular, research activities have concerned the testing of a tire pressure estimation scheme in Hardware-In-the-Loop (HIL) environment, and the development, in Model-In-the-Loop (MIL) environment, of new algorithms for the estimation of vehicle sideslip angle and tire inflation pressure, respectively. Concerning the tire inflation pressure, several estimation schemes have been proposed to improve accuracy of the indirect Tire Pressure Monitoring Systems (iTPMS). The most common iTPMS actually used in many cars present on the market is based on wheel angular speed signal analysis. There are currently few studies that focus on investigating the possibility to execute the iTPMS integration tests in HIL environment. In particular, modelling and parameterization of simulation platform suitable for testing the iTPMS in HIL environment, especially for wheel speed signal frequency analysis, is a topic worthy of research, that have been addressed in the Thesis. The thesis also deals with the development of new estimation schemes for vehicle sideslip angle and tire inflation pressure. Indeed, even if estimation of these variables has been widely studied, moving to next-generation vehicle control and future autonomous driving require further advances in vehicle dynamics state estimation. Specifically, an innovative algorithm for vehicle sideslip estimation is proposed to deal with critical driving conditions of non-trivial scenarios. Based on the Interacting Multiple Model (IMM) filters, it not requires tire-road friction coefficient knowledge to give a reliable estimation of the sideslip angle, also when vehicle drives under critical road surface conditions. The IMM approach has been also adopted in a new estimation scheme to deal with the estimation of the tire inflation pressure

on roads with highly uneven surface. The advantage of the presented algorithms is that they work only with CAN-BUS data coming from the sensors available on ordinary vehicles. The algorithms have been tested rigorously under all possible conditions in MIL simulation environment. To this purpose, a high-fidelity vehicle dynamics simulation platform has been developed, whose modelling ad validation is described in the Thesis.

Table of contents

List of figures

List of tables

Nomenclature

Roman Symbols

a_1 front semi-wheelbase

a_2 rear semi-wheelbase

A_c tire-road contact area

A_x longitudinal shadow area of the vehicle

a_x, a_y longitudinal and lateral accelerations

$a_{x,max/min}$ maximum longitudinal driver acceleration as well as deceleration

$a_{x,min}$ maxim longitudinal driver deceleration

$a_{z,max/min}$ maximum driver deflection and rebound vertical acceleration

b_e engine brake-specific fuel consumption

$C_x, C_y, C_z, C_{M_x}, C_{M_y}, C_{M_z}$ aerodynamics coefficient

C_α Dugoff parameter

$c_{Fric}, c_{t,t}, c_s, c_{s_{nl}}$ friction, tire torsional, suspension linear and suspension non-linear damping coefficients

c_F linear cornering stiffness of front wheel

c_m amplitude of road excitation multiplier

c_R linear cornering stiffness of rear wheel

d_{CP} tire-road contact point lateral offset perpendicular to the road reference line

dp_i non-dimensional pressure increment

e unit vector

$f(\cdot)$ process function

$F_{Aero,x}, F_{Aero,y}, F_{Aero,z}$ aerodynamics forces

f_{ratio} final drive ratio

$F_{sp}, F_d, F_{stab}, F_{St_{Fric,Stat}}, F_{z,bom}$ suspension spring, suspension damper, suspension stabilizer, static friction and bottoming forces

F_x, F_y, F_z Force in longitudinal, lateral and vertical directions

G_d Road roughness PSD

g_{ratio} gear ration of current gear

$h(\cdot)$ output function

h_g height of vehicle's center of mass

$J_{Vehicle}, J_{ICE}, J_{wheel}, J_1, J_2$ vehicle, engine, wheel assembly, wheel mantle, and wheel rim moments of inertia

$k_{Fric}, k_{t,z}, k_{t,t}, k_s, k_{s_{nl}} k_{z,btm}$ friction, tire vertical, tire torsional, suspension linear, suspension non-linear and bottoming stiffness coefficients

K_{TC} torque converter capacity factor

L_y tire relaxation length

M generalized mass matrix

$m_{Vehicle}, m_{fuel}, m_{chassis}, m_s, m_{us}, m_{load}$ vehicle, fuel, chassis, sprung, unsprung and loading masses

n_{GG} g-g diagram exponent used to form different driving patterns

P covariance

p_{eff}, p_0 effective and nominal tire inflation pressure

p_{Fz_1} coefficient representing the pressure effect on vertical stiffness

P_{ICE} engine power

$p_{Ty1}, p_{Ty2}, F_{z0}, p_{ky3}, V_0, q_{re0}, q_{v1}, q_{v2}, q_{Fcx}, q_{Fcy}, q_{Fz1}, q_{Fz2}$ Magic formula micro-parameters

Pos position

Pos_{CP} coordinate of tire-road contact point

q generalized degree of freedom

Q_τ process noise covariance matrix

Q_L generalized forces and torques in the direction of the relevant degrees of freedom

r yaw rate

r_0 unloaded tire radius

r_ω free tire rolling radius

R_τ measurement noise covariance matrix

r_d tire dynamic radius

r_{rim} wheel rim radius

$r_{road,y}$ road horizontal curvature

$r_{road,z}$ vertical road curvature

s IMM filter mode

s_{CP} tire-road contact point distance long the road

$S_{Preview,LatCtrl}$ preview distance lateral control

$S_{Preview,LongCtrl}$ preview distance longitudinal control

$s_{Vehicle}$ distance driven by vehicle on road

SC_{CP} road surface condition at tire-road contact point

t time

t_1 front track width

t_2 rear track width

$t_{Preview}$ preview time

$Trq_{Aero,x}, Trq_{Aero,y}, Trq_{Aero,z}$ aerodynamics torques

$Trq_{ICE}, Trq_{TC_p}, Trq_{TC_t}, Trq_{Fric}, Trq_{gear}, Trq_{Wheel}, Trq_{Brake}, Trq_{Tire}$ engine, torque converter pump, torque converter turbine, friction, gearbox, wheel, brake and tire torques

u control law

v velocity

$v_{x,lim}$ tangential component of the driving velocity

$v_{x,ref}$ driver reference speed

x state vector

x_{Wheel} suspension x-displacement

y output vector

y_t reduced order model output

y_{Wheel} suspension y-displacement

z_{CP} road height at tire-road contact point

z_r road excitation

$z_{sp}; z_d; z_{stab}$ vertical displacement of the spring joint points; damper joint points of front left and front right wheel; vertical displacement of the stabilizer left joint point relative to the right joint point

z_s, z_{us} sprung and unsprung masses vertical displacement

z_W vertical displacement of each wheel

Greek Symbols

α roll angle

α_{road} road generation model parameter

α_{slip} tire slip angle

α_{Wheel} suspension rotation about x-axis

β pitch angle

β_{road} road pitch angle

$\beta_{Sideslip}$ vehicle sideslip angle

β_{Wheel} suspension rotation about y-axis

$\Delta q_{Compl,Fx}, \Delta q_{Compl,Fy}, \Delta q_{Compl,Trqx}, \Delta q_{Compl,Trqz}$ suspension compliance

δ_{btm} tire bottoming offset

$\delta_{Steering}$ wheel steering angle

δ_v steering angle

η_{ICE}, η_{max} engine efficiency and maximum engine efficiency

γ tire inclination angle

γ_{Wheel} suspension rotation about z-axis

$\hat{\omega}_{wheel}$ wheel speed output of reduced order model

Λ likelihood function

$\lambda_{Fz0_i}, \lambda_{Ly_i}$ Magic formula micro-parameters

μ friction coefficient

ν process noise

Ω spatial frequency

$\omega_{ICE}, \omega_{TC_p}, \omega_{TC_t}, \omega_{gear}, \omega_{Clutch}, \omega_{FL,FR,RL,RR}$ engine, torque converter pump, torque converter turbine, gearbox, clutch and wheel angular velocities

ω_n natural frequency

Π Probability transition matrix

ρ_{Air} density of air

ρ_{Tire} tire normal deflection

σ standard deviation

τ time step

τ_{Wind} angle of incidence of wind

Θ inertia tensor

θ twist angle

υ probability vector

φ yaw angle

ρ measurement noise

ξ time-varying IMM switching signal

ζ damping ratio

Acronyms / Abbreviations

ABS Anti-lock Braking System

ADAS Advanced Driver-Assistance System

ASM Automotive Simulation Model

DOF Degree Of Freedom

ECU Electronic Control Unit

EKF Extended Kalman Filter

ESP Electronic Stability Program

FFT Fast Fourier Transformation

GA Genetic Algorithm

GPS Global Positioning System

HIL Hardware-In-the-Loop

IMM Interacting Multiple Model

IMU Inertial Measurement Unit

KF Kalman Filter

MBS Multibody Simulation

MF Magic Formula

MIL Model-In-the-Loop

PSD Power Spectral Density

QC Qarter Car

RMSE Root Mean Square Error

TPM Transition Probability Matrix

TPMS Tire Pressure Monitoring System

UKF Unscented Kalman Filter

VSA Vehicle Sideslip Angle

Chapter 1

Introduction

1.1 Motivation

The modern day automobile not only represents a means of transport, but it also forms an integral part of human society. Since its invention in the early 20th century, it has been ingrained in our daily lives with the passage of time. Increasing research interest in the field of automotive relies in the development of solutions to achieving, among others, one of the main goals of future mobility: safety driving. As can be seen from Figure 1.1, approximately 1.35 million people die each year as a result of road traffic crashes, resulting to be the 8th leading cause of death for people of all ages [11]. To effectively respond to 50% reduction

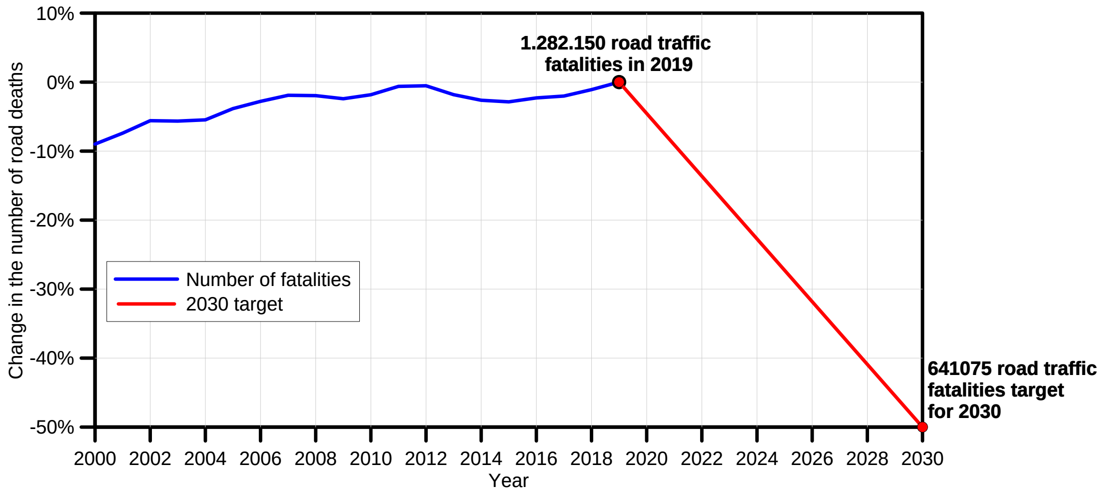

Fig. 1.1 Change in the global number of road deaths as a function of year.

target for road deaths established by the UN General Assembly, vehicle driving automation systems can be innovative solutions to support addressing of this challenge. Indeed, the innovation in the automotive field due to the Fourth Industrial Revolution, enhanced by technological advances of Artificial Intelligence, automation, Internet of Things and fifth-generation wireless technology, gives to car manufacturers the opportunity to improve vehicle's attributes towards the use of Advanced Driver-Assistance Systems (ADAS) and Autonomous Driving Systems (ADS) [12]. ADAS and ADS contribute to achieving the goals of future mobility [13], since they are designed to automate, adapt, and enhance vehicle technology for safety driving [14, 15]. A literary review allows to clarify the role of these technologies. Masello et al. in [16], using safety reports from the United Kingdom (UK), have investigated safety effectiveness of ADAS across several driving contexts and accident types (results are shown in Figure 1.2), estimating that a full deployment of the six most common ADAS would reduce the road accident frequency in the UK by 24%. These data

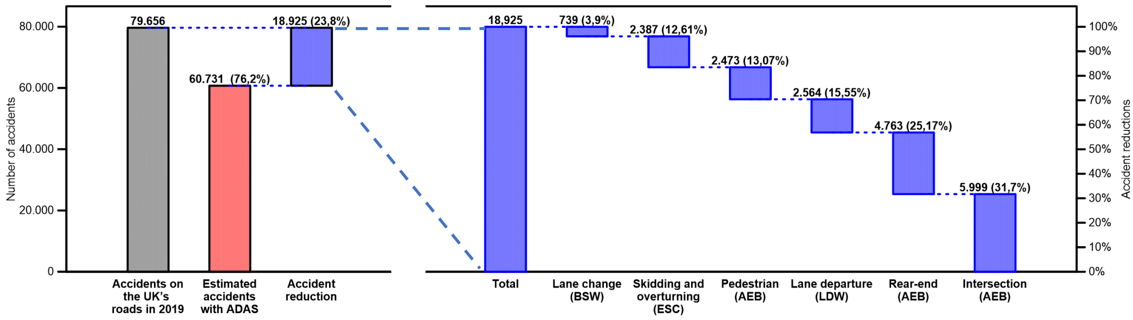

Fig. 1.2 Overall accident reductions using ADAS by accident types. Each bar represents the conservative estimated accident reductions, and the values are accumulated until reaching the total accident reduction of 18925. Above each bar, the figure shows the decrease in accidents, followed by its percentage of the total decline.

made vehicle driving automation systems an attractive option to address the mentioned challenge. In general, as shown in Figure 1.3, the ADAS and ADS can be summarized in three parts: perception, planning and control. Perception refers to the ability of automated driving systems to collect information and extract relevant knowledge from the environment. Planning refers to the process of making purposeful decisions in order to achieve the vehicle's higher order goals. Finally, the control competency, refers to the vehicle's ability to execute the planned actions that have been generated by the higher level processes. The perception part, which is the pioneering component in the whole automated driving systems, through a variety of on-board sensors (camera, lidar, millimeter wave radar, GPS, inertial sensors, etc.), recognizes the surrounding environment and status of the controlled vehicle (Ego vehicle). It provides the initial and boundary conditions for the planning part. Initial and boundary conditions are usually provided in terms of road geometry, limitations given by regulations, ego-vehicle and obstacles current positions, and velocities. Concerning the Ego vehicle status,

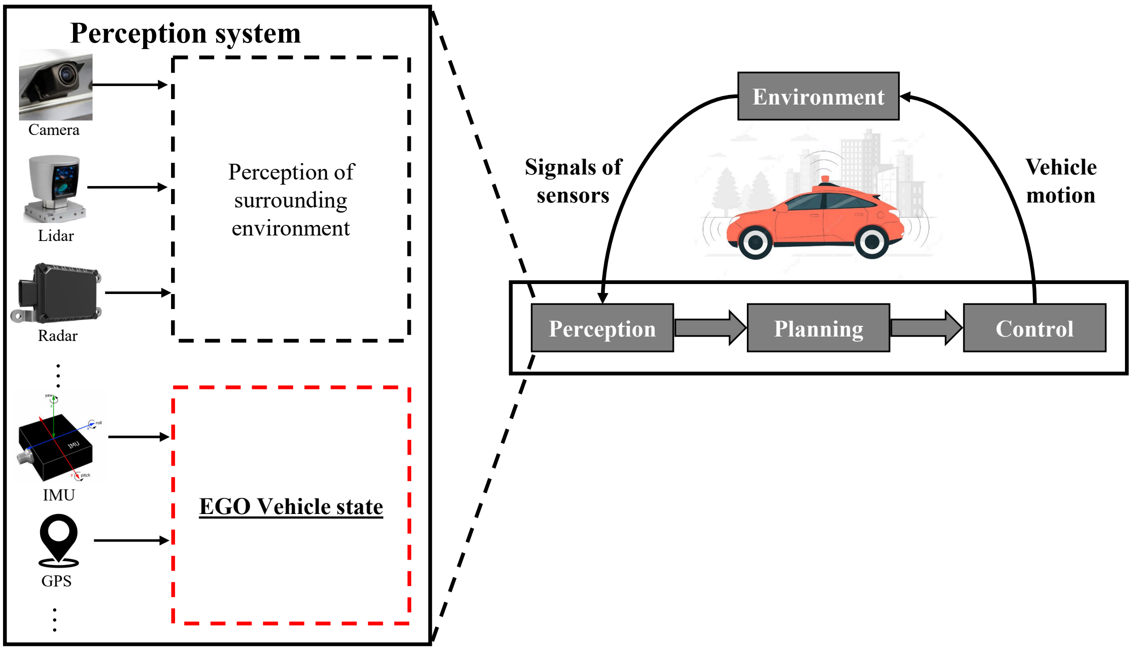

Fig. 1.3 Schematic of automated driving system architecture.

knowledge of quantities, such as of vehicle sideslip angle, yaw rate, position and orientation, as well as tire inflation pressure, is fundamental, especially for vehicle dynamics control systems. In particular, some of these quantities, such as sideslip angle and tire inflation pressure, are usually estimated indirectly rather than acquired with a direct measurement, for both technical and economical reasons. It currently forms a big part of the research and development effort that goes into creating a modern automated driving car. An overview of ADAS systems, and in particular on vehicle dynamics control systems, is presented in the following section, that allows to better understand the key role of vehicle dynamics states estimation.

An Overview of ADAS and Vehicle Dynamics Control Systems

The importance of vehicle states estimation has increased starting from 90*s*, when it became a fundamental task for the incoming active safety systems like Anti-lock Braking System (ABS) and Electric Stability Program (ESP) [17]. The ABS helps vehicles avoid locking their wheels when braking, which improves the vehicle's stopping distance. The system's Electronic Control Unit (ECU), processing speed signals of the four wheels measured by dedicated wheel speed sensors, releases the brake pressure of an individual wheel when its locking is detected. The ESP generally can be seen as an extension to ABS for further augmenting vehicle safety [18], which, other than ABS, comprises the functions of the traction control system for improving the vehicle lateral stability. Furthermore, the ESP also monitors the vehicle states and tries to keep their values within desired thresholds, such as for the sideslip angle: the EPS, acting on brake and engine torque demand, prevents the sideslip angle from becoming large enough to digress into the tire saturation range, reducing loss of traction and improving vehicle's stability. Both ABS and ESP are reactive systems as they intervene only when the vehicle is operating near to unstable conditions. Active control systems, instead, work continuously in order to influence the dynamics behaviour of a vehicle, such as adaptive dampers, active aerodynamics, torque vectoring and rear wheel steering. The first, by changing the damping in the four suspensions, toggles between the opposite objectives of comfort and road holding improvement. The active aerodynamics working principle consists of varying aerodynamic drag and vehicle downforce according to the actual manoeuvre. The torque vectoring, controlling the yaw moment of a vehicle through the traction/braking torque across the four wheels, influences the lateral dynamics response of the vehicle and obtain better vehicle handling performance. The rear wheel steering system, controlling the steering of the rear wheels of the vehicle, enhances the vehicle handling performance. Control logic of all these active systems regulates the vehicle states with respect to some sub-objectives on the basis of measurement and estimation of the actual vehicle states, such as yaw rate and sideslip angle. Furthermore, the vehicle sideslip angle is also important to improves the stabilization performances and path tracking capabilities for ADAS/ADS systems [19], [20], specifically in the vehicle lateral control stability in critical driving conditions [21], [22]. Vehicle ADAS suite also includes a Tire Pressure Monitoring System (TPMS). Based on direct measurement of tire inflation pressure, or on indirect estimation of tire inflation pressure by other sensors measurement, detects tire pressure losses. Indeed, deflated tires are known to cause increased forward drag, that lead to the increment of vehicle fuel consumption. On the other hand, it have also effects on lateral steering behaviour of vehicle, which are commonly the cause of driver loss of control and subsequent vehicular accidents [23]. As seen, the implementation of ADAS, as well as vehicle dynamics control systems, depends on accurate vehicle dynamics states information. Conventionally, these information are measured by available onboard sensors, which accuracy are relatively low and could do not satisfy the requirements of vehicle control systems. In addition, considering the cost of mass-production vehicles, many sensors are too expensive to equip [24]. To obtain more accurate and reliable vehicle dynamics states information a promising technique is to estimate the vehicle dynamics states by employing estimation schemes. In this thesis, two estimation schemes are described, for vehicle sideslip angle and tire inflation pressure, respectively. An overview of the sensor configuration schemes used for the estimation of these quantities is presented in the following section.

Sensor Configuration Schemes

In this section is discussed the sensor configurations used to estimate the vehicle sideslip angle and tire inflation pressure. Generally, the sensor configuration scheme varies with respect to the vehicle dynamics state to be estimated, which, in turn, influence the choice of the estimation method and vehicle model. To determine the specific sensor configuration scheme, precision and the cost of sensor equipment must be defined: low-cost sensors are usually adopted when estimation accuracy is not influenced. As described above, real-time information of the sideslip angle is fundamental in many active vehicle safety systems, such as yaw stability control [25], rollover prevention [26], and lane departure avoidance [27]. Sideslip angle estimation has become a hot topic of research because its measurement requires a suite of optical and GPS-based sensors, hardly available on-board of ordinary vehicle due to economical reasons [28]. Sensor configuration schemes for the sideslip angle estimation are listed in Table 1.1. Some sensor configuration schemes consider only measurements representative of the lateral dynamics of vehicles, such as in [29], where the wheel steering angle $\delta_{Steering}$ and yaw rate r are measured to estimate the sideslip angle. In [30], instead, the steering wheel angle and lateral acceleration a_y are taken as measurements in the moving horizon estimation scheme (MHE). These estimation scheme reliable estimate the sideslip angle in manoeuvres where the longitudinal interactions have small effects, and so can be neglected in the dynamics equations used. Otherwise, measurement that characterize the longitudinal dynamics should be considered, such as wheels angular speed ω_i and longitudinal acceleration a_x. The most widely applied sensor configuration on actual ordinary cars that is used to estimate the sideslip angle is described in [31], where all the mentioned measurement are used. In contrast to this popular sensor configuration scheme, the suspension deflection Δ_{sus} and roll rate p are measured in [32]. Also *GPS* measurements, such as the *GPS* tracking angle φ_{GPS} and *GPS* ground velocity v_{GPS} are used in [33] to estimate the sideslip angle for a wide range of maneuvers. For what concern real-time information of the tire inflation

Table 1.1 Sensor configuration, vehicle model, and estimation method for sideslip angle estimation.

Sensor configuration	Model	Estimation method	Ref.
$\delta_{Steering}$, r	2DOF single-track model	EKF, NLO, SMO	[29]
$\delta_{Steering}$, a_y	2DOF two-track model	MHE	[30]
$\delta_{Steering}$, r, a_y	2DOF single-track model	UKF, EKF	[34]
$\delta_{Steering}$, ω_i, r, a_y	3DOF two-track model	UKF	[35]
r, a_x, a_y	kinematic model	EKF	[36]
$\delta_{Steering}$, ω_i, r, a_x, a_y	3DOF single-track model	SMO, EKF, NLO	[31]
$\delta_{Steering}$, ω_i, r, a_x, a_y, Δ_{sus}, p	4DOF two-track model	EKF, UKF	[32]
$\delta_{Steering}$, ω_i, r, a_x, a_y, v_{GPS}, φ_{GPS}	kinematics/2DOF single-track model	KEKF, DEKF	[33]
$\delta_{Steering}$, r, GPS	2DOF single-track model	KF	[37]

pressure, as explained in previous section, it is fundamental for the tire pressure monitoring systems to detects deflated tire, which causes not only changes in vehicle steering behaviour, and a worsening of ride quality, but also increases vehicle fuel consumption, uneven wear of tire, and road pavement deterioration. Indeed, for every 0.2 *bar* under normal inflation levels, fuel consumption can increase and the tire lifetime can decrease by 20% [38]. Furthermore, a lower tire pressure significantly affects pavement damage and decreases the fatigue life of the asphalt surface layers by up to 200% and 300%, respectively [39]. On the basis of sensor configuration scheme used, two main types of TPMS are known: direct TPMS (dTPMS), which employs pressure sensor on each wheel to measure tire pressure; and indirect TPMS (iTPMS), which exploits the measurement of other sensors already present in the vehicle. The dTPMS is generally highly precise, but it has high costs. Each sensor is equipped with a battery that has to be replaced or recharged periodically. Winter tires also need their own sensors. Therefore, a puncture or replacement requires an additional activity for the tire dealer and additional costs. The iTPMS is a cost-effective alternative which outperforms the dTPMS in cost, life and maintenance. It does not rely on direct measurement of the air pressure within the tire, and instead performs an indirect estimation of the pressure using information from other sensors already present in the ordinary vehicles. Sensor configuration schemes for the tire inflation pressure estimation are listed in Table 1.2. Most of iTPMS available on the market are based on measurement of wheels angular velocity ω_i, such as the method proposed by Personn [38], that, by comparing the four angular speeds, identifies the wheel that losses pressure. Wheels angular velocity are also used in iTPMS which provide for tire pressure loss detection by frequency analysis wheels speed signals. Indeed, due to the roughness of the road and the torsional deformation of the tire, an oscillation of the angular velocity is induced. Tire stiffness is affected by inflation pressure so, as the pressure value changes, so does the wheel speed oscillation frequency. Others algorithms estimate estimate tire inflation pressure using the wheel $\ddot{z}_{Wheel}$ and sprung vehicle body $\ddot{z}_{Body}$ vertical accelerations, such as in [40], where a frequency analysis on these vertical acceleration has been performed to detect tire pressure losses. Another class of estimation algorithms exploit the ESP measurement. In particular, Solmaz [41] starts from the measurements of lateral acceleration a_y, yaw rate r, steering angle $\delta_{Steering}$ and vehicle speed $v_{x,Vehicle}$ available by ESP system to estimate lateral vehicle dynamics state, together with the tires cornering stiffness, from which tire pressure drops have been detected. Reina [42] also starts from the ESP measurements, but he exploits the vehicle vertical dynamics to build the prediction model of a Kalman filter estimator for tire stiffness. An overview of the existing estimation schemes on sideslip angle and tire inflation pressure estimation, together with their research gaps, is presented in the following section.

Table 1.2 Sensor configuration, model, and estimation method for tire inflation pressure estimation.

Sensor configuration	**Model**	**Estimation method**	**Ref.**
ω_i	speed ratio, diagonal and relative differences	wheel speed comparison	[38]
ω_i	2DOF torsional wheel oscillation model	wheel speed spectral analysis	[43]
$\ddot{z}_{Wheel}$, $\ddot{z}_{Body}$	2DOF quarter car model	vertical wheel acceleration spectral analysis	[40]
$\ddot{z}_{Wheel}$, $\ddot{z}_{Body}$	2DOF quarter car model	KF, tire vertical stiffness estimation	[42]
a_y, r, $\delta_{Steering}$, $v_{x,Vehicle}$	2DOF two-track model	quadratic optimization, tire cornering stiffness estimation	[41]

1.2 Literature Review

Most ADAS, and especially vehicle dynamics control systems, include in their architecture sensors which collect information about the vehicle's current state. Ordinary vehicles on the market are equipped with a sensor cluster present in the ESP system which includes lateral, longitudinal and vertical accelerometers, yaw rate, wheel speed and steering angle sensors. Other common sensors consist of *GPS*, and sensors of suspension control system, such as a vertical wheel accelerometer [44]. These measurement signals can be acquired from the controller area network (CAN) bus upon which the majority of intra-vehicular communication takes place [45], [46]. Starting from these and other measurements, using estimation schemes, quantities for which sensors are unavailable like the vehicle sideslip angles and the tire inflation pressure need to be estimated [47]. Generally, the development of estimation schemes is carried out in Model-In-the-Loop (MIL) environment. The validation of estimation schemes, instead, is performed in Hardware-In-the-Loop (HIL) environment, with the aim to check the system functions relative to the software requirements. Testing of iTPMS based on wheel speed spectral analysis in HIL environment presents some critical issues concerning the development of simulation platform, making this a topic worthy of research. All these issues listed above are studied and presented in the following subsections to obtain an idea of the state of the art. Research limitations from the literature review are then presented at the end of each subsection to clearly project the objective and scope of work.

1.2.1 Simulation Platform for Testing iTPMS with Wheel Speed Sensors

The iTPMS based on wheel speed measurement is a cost effective solution adopted in many models of car bands, including Audi, BMW, Mazda, Toyota, Alfa Romeo, Fiat, Lancia, Citroen, Peugeot, etc.
It detects tires pressure losses combining two analyses:

- dynamic rolling radius analysis;
- tire oscillation analysis.

The dynamic rolling radius analysis detects tire pressure loss by comparing the relative speeds of the four wheels. The tire oscillation analysis, on the other hand, estimates frequency characteristics of the tire included in the wheel speed signal. The iTPMS combines the advantages of this two different analysis, summarized in Table 1.3, to improve the reliability of the pressure loss detection. Analyses based on wheel speed differences require low computational effort compared to the spectral analysis methods. Furthermore, the wheel speeds relative differences and the wheel speed ratios show a good response to the size of deflection. Otherwise, the spectral analysis of wheel speed is more sensitive to disturbances [48]. Dynamic rolling radius analysis is able to detects the deflation of a single tire. A deflation of all tires therefore cannot be detected. This feature can be, however, achieved with the tire oscillation analysis. To reduce the experimental effort required by conventional

Table 1.3 Properties of indirect tire pressure monitoring system with wheel speed sensors (+ positive, ++ very positive, − negative).

Estimation method	**Size of deflection**	**Disturbance sensitivity**	**Relative tire deflation**	**Absolute tire deflation**	**Computational effort**
Wheel speed relative difference	++	−	+	−	+
Wheel speed diagonal difference	+	+	+	−	++
Wheel speed ratio	++	++	+	−	+
Wheel speed spectral analysis	+	−	+	+	−

approaches both in the early phase of the iTPMS development and for the validation of software functions during the integration of iTPMS with vehicle systems, many simulation methods can be used to replace the vehicle test on road. In particular, models used must be able to simulate the tire behavior, both inflated and deflated. When a deflation occurs two pressure-dependent phenomena are observed by the iTPMS: the change of rolling radius and

the change of natural frequency contained in the wheel angular speed. The change of rolling radius can be easily represented in the simulation. Instead, simulation of the tire frequency behavior at pressure loss is a critical issue. Indeed, the simulation platform should integrates models capable to simulate the tire vibration effects on wheels speed on any road surfaces, in order that simulated wheels speed spectrum must be comparable to the one measured in real-world tests. This is a key requisite for testing the wheel speed spectral analysis in a simulation environment. These requirements involve modelling at component level, i.e. the tire, axle level, and full vehicle level [49]. The tire model is the key element of the simulation: it should be able to represent the typical tire vibration behavior at different inflation pressures, as a function of tire properties, depending by construction, rubber compound etc.
A tire model implemented in many commercially available vehicle dynamics simulation platforms is the FTire model. It consider a physical approach to modeling the tire and road surface interaction. FTire applies a flexible ring approach to the tire's structure, which allows it to be unconstrained by single point contact limitations. In particular, a finite number of belt elements are connected by stiff springs in both in-plane and out-of-plane directions. To every belt element, a number of mass-less tread blocks are appended, which carry stiffness and damping in radial, tangential and lateral direction. FTire can be used to calculate modal response up to 200 Hz on short and large-waved road surface unevenness [50]. Automotive industry widely adopt also CDTire, a multi-physics tire model that includes mechanical, thermal, and cavity modeling. The model predicts large deformations and frictional contact under loaded conditions. In particular, calculates the tire belt angles and uses them as a parameter to predict influence on force generation and structural integrity. This model also implements Euler's ideal gas law theory, coupled with cleat impact response, to model the internal pressure cavity mode during cleat impacts, generally above 200 Hz [51]. Generally, the Ftire and CDTire models, integrated into a MIL environment, are suitable for simulation to investigate pressure-dependent properties of tires as a function of influencing factors (tire size and structure, drivetrain, etc.), that is important at an early phase of development process of iTPMS. However, these models are poor adequate to functionally test iTPMS's software in HIL environment. Indeed, due to their high complexity a long simulation time is needed, and therefore result to be inconsistent with real-time simulation required by HIL environment. To address this issue, Ftire and CDTire version for real-time simulation have been developed, adopting, however, many simplification assumptions. The rigid ring tire model [52] is the most common solution to represent the tire vibration behavior at pressure loss, while reducing the computing time. Assuming the tire belt as a rigid ring, coupled to the rim by springs and dampers in radial direction and torsional direction, it calculates rigid vertical and longitudinal tire in-plane vibration modes up to 100 Hz [53]. A key simulation requirements for iTPMS

virtual development is that models can be able to reproduce tire vibration behaviour on any road surface. Since the rigid ring is a single point contact model, it can be used only on surfaces with random unevenness or on road with long wavelength irregularities [52]. To implement the rigid ring model for simulation with short wavelength road unevenness the enveloping model in needed, that allows to predict the dynamic tire and road surface interaction [54]. The parameterization process of rigid ring model is often a challenge for a high-quality simulation. Model's parameters can be determined by different kinds of rig tests, especially cleat test. However to virtually test the iTPMS, more complex model are needed, which include the suspension model, in order to investigate in simulation the influence of axle kinematics and compliance on tire vibration behavior, since the axle parameters have a significant influence on the natural frequency of the tire in-phase vibration modes [49]. In general, full vehicle simulation must be considered to test the iTPMS [55]. It must reliable emulate the real-world vehicle test in a simulation environment. This allows to evaluate the effects of vehicle influence factors (see Table 1.4) on frequency characteristics inherent in the wheel angular speed by vehicle systems. Given the complexity of the vehicle system that makes parameterization process very hard, the accumulation of the deviation and tolerance of each parameter is not negligible. This, together with the uncertainties due to he several influence factors, can undermine the accuracy of the model, and the final simulation result may well not be perfect. Due to the high requirements on the accuracy of the simulation model (pressure losses result in change of resonance frequency between 0.5 and 2 Hz), the parameterization on test rig is not sufficient. Model parameterization through optimization methods can make the simulation result very close to the test result. However, the physical meaning of each parameter can not be guaranteed.

Research Gaps in HIL Testing of iTPMS with Wheel Speed Sensors

A full vehicle simulation can be used to execute virtual test on iTPMS based on the wheel speed spectral analysis, which involve modelling of tire, suspension, and any other vehicle's system influencing the iTPMS. The key element of the simulation is the tire: most of the tire models present in literature are capable to investigate the tire influencing factors (i.e. tire construction, rubber compound, etc.) on the tire vibration behaviour, but are time-consuming, and not adequate for real-time simulation. The most common model with real-time simulation capability is the rigid ring with enveloping model. However, some issues are related to its parameterization. The simulation results need to be comparable with the data from vehicle road test, with a high accuracy. Usually, this requirement can not be achieved only with conventional parameterization process on test rig. Otherwise, optimization methods can be used to obtain models parameterized in such a way that simulation result very close

Table 1.4 Vehicle factors influencing the iTPMS with Wheel Speed Sensors. Rating: 1 - small; 2 - mid; 3 - big.

Factor	**Rating**
Vehicle weight (LLVW and GVW)	
Total vehicle weight	2
Axle weight distribution (front and rear)	3
Difference of weight, weight distribution between LLVW and GVW	3
Geometrical data	
Wheel base and track width (front and rear)	2
Position of Centre of Gravity (x/y/z)	1
Drive shaft length (left and right)	2
Engine	
Type (petrol, diesel, CNG, LPG, hybrid, ...)	2
Power, torque, max speed	2
Number of cylinder	3
Gear box	
Type (MT, MTA, automatic, ...)	2
Number and ratio of transmissions	2
Drive system	
Concept (FWD, RWD, 4WD const./variable torque distribution)	3
Hybrid	depends on the system
Suspension/ Damper system	
Type (air-sus, steel-sus, hydro-pneumatic, ...)	2
Structure (McPherson, multi-link, ...)	2
Suspension control	2
Suspension/ damper tuning	1
Spring rate (Front/Rear)	1
Stiffness of whole suspension	2
Chassis System	
Active torque distribution on drive axle	3
Active body control	1
Rear wheel steering	2
Power steering (e.g. hydraulic PS, electric PS)	1
Wheel Speed Sensor	
Type (e.g. AMR/ GMR, Hall)	3

to the vehicle road test measurement. In general, research related to the development, parameterization and validation of simulation platform to test iTPMS tire oscillation analysis in HIL environment is less common in the literature. There is a need to define methodology to develop models which provide a sufficiently good representation in HIL simulation of the tire vibration behaviour inherent in wheel speed signal: simulation must generate inputs for the iTPMS of such quality that any inconsistencies or implausibility can not be detected. Particular important is the investigation on parameterization process based on optimization methods, analysing pros and cons of using model with poor physical meaning to test the functionality of iTPMS software in HIL environment.

1.2.2 Tire Inflation Pressure Estimation

Tire pressure has a significant influence on the behaviour of vehicles, especially in terms of safety, consumption and wear. In 2007, the National Highway Traffic Safety Administration (NHTSA) in the USA had already published a legal regulation (FMVSS 138) requiring the installation of a tire pressure monitoring system in light vehicles. In 2012, the European Union also issued a similar regulation. Starting from 2014, the TPMS is mandatory in USA and in some European countries. An underinflated tire induces: a reduction of tire-road interaction forces; an undesirable steering behaviour; an increase of fuel consumption; or an unexpected blowout due to high temperature. An overinflated tire induces an undesirable steering behaviour and an uneven wear. The NHTSA estimates that about 55% of vehicles have at least one underinflated tire causing the waste of 2.8 billion gallons of fuel and about 260,000 accidents per year. Moreover, a low inflating pressure in tires reduces tire tread life by 15% and increases the frequency of tire changes [56]. Respect to direct pressure measurement system, which have some backwards in terms of cost, life and maintenance, the indirect TPMS is a cost-effective solution that exploits measurement by sensors available on-board the vehicle to estimate the tire inflation pressure. The most common estimation scheme is based on the comparison of the four wheels angular speed [57], [58]. The main limitation of this estimation scheme is that it can detects low pressure of one to three tires; if all four tires have the same pressure reduction, it is not possible to detect the tires deflation. In that case, the resonant frequency of the wheel speed can be used to estimate the tire inflation pressure, as it correlates with tire pressure [59], [60]: a decrease in a tire pressure reduces stiffness of tire, which lead to a change in frequency response of tire to road surface unevenness, in particular to lower torsional resonance frequency. Therefore, tire deflation can be detected by comparison of estimated resonance frequency with the one in normal pressure [61], [62]. In this kind of analyses the effects of influence factors on resonance frequency, such as engine noise, undermine the reliability of the estimation, which, can be mitigated through compensation methods [43]. Frequency analysis is applied to wheel vertical acceleration in [40] to estimate the inflation pressure. Hybrid solutions that combine at least two of the mentioned methods are presented in [48], with the aim to take the advantages of different methods in a single estimation scheme, improving the reliability of deflated tire detection. Other methods are based on the correlation between tire stiffness and inflation pressure. For example, in [63] a self-adaptive nonlinear filter with an optimal finite impulse response derivative was designed to estimate the tire longitudinal stiffness related to the tire pressure. Solmaz [41], instead, starts from the measurements available by ESP system to estimate tire cornering stiffness, through which detects tire deflation. Reina [42] also starts from the ESP measurements, but he exploits the vehicle vertical dynamics to build the prediction model

of a Kalman Filter (KF) estimator for tire vertical stiffness. Road roughness is a critical unknown input for the model-based estimator [64], but often it is overlooked in the previously proposed estimation techniques.
Recently, Lee [65] addressed this problem and proposed an iTPMS based on Adaptive Extended Kalman Filter (AEKF) that can estimate both the pressure and the roughness of the road.

Research Gaps in Tire Inflation Pressure Estimation

As described in previous section, theoretical and practical results have been obtained from iTPMS. However, only a few examples have been turned into commercial products [66], because there is still room for improvement in terms of accuracy and reliability. In particular, most promising estimation scheme concerns with the vertical tire stiffness estimation with model-based approach. However, existing estimators (belonging to the Kalman Filter family) are based on a single dynamical model that, since the vertical vehicle dynamics is characterized by great complexity and can further vary unexpectedly with the road roughness, exhibit poor closed-loop performances. As a result, it may be subject to significant estimation errors. Therefore, approaches which exploit multiple models have to be investigated to deal with abruptly change of vehicle vertical dynamics due to variation of road surface unevenness level.

1.2.3 Vehicle Sideslip Angle Estimation

A proper vehicle dynamics control system design requires a large amount of information, e.g. yaw rate, sideslip angle, and longitudinal velocity, just to name a few. A dedicated full sensor set is not practically attainable, mainly due to high costs. Therefore, state estimation methods for measurement information based on low-cost sensors have been widely exploited and applied in the automotive industry. Indeed VSA is not measured directly for a series production vehicle, since could be measured by means of high-cost sophisticated laboratory devices (e.g, optical sensors such as the Corrsys-Datron [67]) - that present issues in terms of compatibility with vehicle packaging, cost, reliability, accuracy, and robustness to environmental conditions - rather than a production vehicles sensor [68]. It follows that the estimation of VSA has been often investigated in the literature due to its high potential in improving the performance of vehicle motion control systems, such as stabilization and path tracking capabilities or vehicle lateral control stability in critical driving conditions[69, 70]. Among the different proposed approaches, kinematics-based estimators have raised large interest since they do not require tire parameters. However, they are reliable only for transient maneuvers due to the progressive integral drifting caused by sensor errors [71]. Conversely, data-driven approaches are model-free [72] and independent of sensor errors [71] since they exploit deep neural networks and their capability of serving as universal function approximator [73], but their main drawback is the low reliability of the estimate when conditions are not sufficiently close to the ones of the training set [67]. Some techniques involve GPS signals, such as in [74] and [75] where GPS information have been combined with Inertial Measurement Unit (IMU) using Kalman filters for the estimation of the sideslip angle, further evaluating estimation errors due to signal latency of the GPS module, which operates at 5 Hz or 10 Hz. In [76] the sideslip angle has been estimated using measurement of a carrier based differential GPS [76]. The main issue for GPS based estimation techniques relies in the need to have satellite signals constantly, while in urban environments loss of communication are frequent Moreover, GPS systems are expensive [77]. These issues still make the model-based estimation methods the most attractive solution adopted nowadays. These use low-cost sensors measurement such as gyroscopes and accelerometers to estimate the sideslip angle. In [78] and Extended Kalman Filter (EKF) based on a 4DOF vehicle dynamics model and magic tire formula has been used to estimaate the sideslip angle. Instead, in [79] the EKF is based on a 3DOF vehicle model and Dugoff tire model. Also the use of unscented Kalman Filter has been investigated in [32], that based on a 4DOF vehicle model and a Dugoff tire model, has been used to estimate the sideslip angle for manoeuvres with constant speed. The accuracy of mode-based approaches rely heavily on a reliable modelling of the vehicle. The most crucial part of modelling the vehicle is to successfully represent the tire cornering stiffness as incorrect modelling tends to generate steady state errors. In particular, the challenging task in the tire modelling is that the cornering stiffness is influenced by time varying parameters, which act as unknown inputs of the system's model. Indeed, despite VSA estimation has been greatly promoted in recent years, its estimation with unknown inputs is still an interesting issue that requires further research study [80]. A critical unknown input that should be obtained first to predict the VSA is the tire-road friction coefficient [81]: unmodeled effects of road surface conditions can worsen the reliability of the estimation, since it can be only carried out if the tire model truly reflects the actual conditions. Many researcher have addressed this issue using adaptive Kalman filters to estimate, together with the sideslip angle, also the cornering stiffness, both for linear [82] and non-linear [83] tire models. In this case, the tire stiffness can be modelled as the state variable for random walk model, that varies the parameters at every sample time according to a random Gaussian noise [84]. In [31] tire lateral and longitudinal forces have been estimated with an EKF with a sliding mode observer and variable covariance matrices depending upon tire actual operating conditions. As seen model-based model based estimator based on Kalman Filter ared widely used to estimate the sideslip angle. However, when the vehicle dynamics are characterized by great complexity and vary unexpectedly, an estimator based on a single dynamical model can exhibit poor closed-loop performance. To deal with this aspect, Multiple Model (MM) approaches designed according to different vehicle behaviors, each characterizing specific driving conditions, can achieve more accurate estimation performance than a solution based on a single model.

Out of the various proposed solutions based on the MM paradigm, the Interacting Multiple Model (IMM) algorithm is the most popular due to its high accuracy, low computational burden, and best cost-effectiveness [85]. Note that, due to its features, it has become the mainstream solution for the state estimation problem of hybrid systems and it found application in maneuvering target tracking, fault detection and diagnosis, and navigation. The usual IMM structure is composed of a bank of multiple filters, each set on a specific dynamical model, that operates in parallel to obtain a better state estimate of targets. A model management algorithm, governed by an underlying Markov transition matrix, is in charge of the switching behavior among the multiple models. The estimation state-of-art proposes different versions of the IMM, ranging from the use of linear KF to its nonlinear extensions, e.g., Extended Kalman Filter, Unscented Kalman Filter, and so on.

An IMMUKF was used in [86] to estimate lateral tire–road forces and VSA, considering the changing of driving conditions in which a vehicle can be operated. In particular, this integrate the estimates from a four-wheel nonlinear vehicle dynamics model with two kinds of tire models: a linear tire model and a nonlinear Dugoff tire model. Another IMMUKF for VSA estimation is also proposed in [87], consisting of 3 UKFs based on a 7DOF nonlinear vehicle dynamic model combined with Magic Formula tire model, differing for noise covariance matrices. VSA estimation is carried out on the basis of previous step road condition estimation by a Strong Tracking Unscented Kalman filter (STUKF). Furthermore, a Self-Correction Data Fusion (SCDF) algorithm is developed to integrate results of IMM estimator and direct integral method. [88] uses an adaptive parameter Interacting Multiple Model unscented Kalman filter algorithm (IMMAUKF) for vehicle state estimation purpose. It consists of two UKF algorithms based on vehicle kinematics model: one is established according to Constant Turn Rate and Acceleration (CTRA) theory, while the other use a simplified version of the CTRA model to overcome the problem of estimator failure when the yaw rate is close to zero. In addition, AUKF algorithm is implemented by combining the UKF and Sage-Husa filtering algorithms to reduce noise.

Beyond the aforementioned approaches that leverage the UKF theory, other extensions of the classical KF method can be deployed to realize an IMM solution. Specifically, in the VSA estimation problem, can be found different interesting algorithms. For example, in [89] an

IMM based on three Square-root Cubature Kalman filter (SCKF) is used to estimate the yaw rate, sideslip angle, and the longitudinal and lateral vehicle speeds from a 3DOF nonlinear vehicle dynamic model, combining with the brush tire model. Instead, the same approach is investigated in [71], where a receding horizon paradigm is introduced to obtain a new algorithm referred to as the Square-root Cubature Receding Horizon Kalman filter (SCRHKF), improving the robustness w.r.t. the model uncertainties losing, however, in convergence speed performances. Particularly interesting are also the approaches that exploit the Cubature Kalman Filter (CKF) to develop a specific version of IMM. In the automotive context, among the most relevant works, we cited the strategy proposed in [90] where two filters are used in parallel: one with linear tire model for normal driving conditions and the other with nonlinear Dugoff tire model for extreme driving conditions. The corrections of lateral acceleration, road adhesion coefficient and cornering stiffness are taken in history to mitigate the effects of gravity on the banked road on the accelerometer in the y direction. According to preliminary investigations, the IMM seems a promising solution to address unknown inputs for sideslip angle estimators, such as the unknown tire-road friction coefficient [91]. In general, the state transitions between the models are described through a Markov matrix with constants elements, although the use of variable matrices has been recently proposed [92].

Research Gaps in Vehicle Sideslip Angle Estimation

Most of reviewed work based on model-based estimator involve techniques that estimate the vehicle sideslip angle with all inputs known. Several issues arise that have not been addressed yet. These include the estimation of the sideslip angle while dealing with the unknown tire-road friction coefficient according to the actual road surface condition (dry, damp, wet and snowy asphalt). Some articles have addressed the problem estimating the tire cornering stiffness. Another estimation approach to deal with unknown inputs is to use the multiple model algorithm designed specifically to deal with systems whose model can change abruptly according to actual road surface condition. However, few works have investigated this kind of approach. Furthermore, IMM algorithms that consider Markov matrix with variable coefficients should be analysed to improve sideslip angle estimation accuracy in scenarios where the friction coefficient randomly changes. Indeed, the Transition Probability Matrix (TPM) has a crucial role in the definition and operation of the IMM algorithm, and its tuning remains a difficult task to be accomplished by leveraging a priori information and/or dedicated analysis. Therefore, the usual solution adopted in the current literature considers the probabilities of the state transitioning among models as constant values. However, this setting method tends to be quite conservative and degrades the estimation accuracy of the IMM system, since it relies on two strong hypotheses, namely: *i*) the assumption that time-varying probability of the TPM transitioning among models can be well represented by a constant value; *ii*) constant probability value is well a priori known. Indeed, if the transition probabilities could be adapted online according to the current system model information, the performance of the IMM algorithm can be improved. In this perspective, examples can be found in the aeronautic field, where target tracking of the kinematic variables of a ballistic missile is improved by exploiting different TPM with time-varying probabilities of the state transitioning that relies on physical considerations on the phases of flight [93], [92].

1.3 Objectives and Scope

The primary objective of the work presented in this thesis is to develop and validate algorithms to indirectly estimate the vehicle sideslip angle and tire inflation pressure.
Concerning the tire inflation pressure estimation, most of algorithms use wheel speed signal in two parallel analyses: tire rolling radius analysis, and tire oscillation analysis. This estimation scheme is implemented in current commercially available indirect tire pressure monitoring systems. During the development of this system a lot of parameters must be tuned. It is a very challenge task due to many factors that influence the two analyses on wheel speed signal, which inevitably cause a degradation of algorithm sensitivity to tire deflation. Therefore, many versions of iTPMS software are released for subsequent parameters adjustment, and functionality of each of them need to be validate with integration test. A well-known cost-effective alternative to vehicle road tests for validating embedded software on ECU is the HIL testing. However, few researches have investigated HIL testing of iTPMS, especially for the tire oscillation analysis. In particular, there is a need to define a methodology to develop and parameterize simulation platform suitable for testing the iTPMS in HIL environment. The most promising approach to improve estimation accuracy of tire inflation pressure consist of using a model-based estimator, based on vertical dynamics of vehicle. It estimates the vertical tire stiffness, that can be used to evaluate the tire inflation pressure through an experimental relationship. However, critical issue of this estimation scheme is that road surface roughness acts as an unknown input to the vehicle vertical dynamics model, undermining the reliability of the estimation. Similarly, one of most important issue of model-based algorithms for sideslip angle estimation are unknown inputs, in particular the time-varying tire road friction coefficient, that, under critical road surface condition, makes the modelling of tire cornering stiffness incorrect, worsening the accuracy of estimation. The specific objectives are enumerated below.

1. **HIL Testing of iTPMS with wheel speed sensors**
   Main objective is to define a methodology for developing simulation platforms to

be used in HIL environment for executing functional tests on iTPMS software. In particular, two goals:

- enabling virtual check of iTPMS during learning phase, dedicated to calculate compensation coefficients and he resonance frequencies of each tire at normal pressure;
- enabling virtual check of iTPMS during detection of tire deflation.

2. **Estimation of Vehicle Sideslip Angle and Tire Inflation Pressure**

   - Developing estimation algorithms able to estimate vehicle sideslip angle under critical driving conditions, considering scenario with randomly time-varying and unknown tire-road friction coefficient.
   - Similarly to sideslip angle, developing an estimation algorithm to estimate tire inflation pressure considering scenario with randomly time-varying and unknown road surface roughness level.
   - To facilitate onboard integration, the estimation algorithms should not be computationally intensive. Furthermore, the algorithms should only use low cost sensors generally available on ordinary vehicles whose signals are present on the vehicle CAN network.

1.4 Thesis Contributions

This thesis provides with several contributions in the field of vehicle state estimation. Most of the results have been validated with a vehicle dynamics high-fidelity simulation platform developed during the research activity. The contributions of the thesis are listed as follows:

1. **HIL Testing of iTPMS with wheel speed sensors**

   - A methodology to develop models for real-time simulation has been defined, which provide a reliable representation of wheel dynamics effect on wheel speed signal respect to real-word test, while minimizing the effort for model parameterization.
   - A parameterization process based on optimization methods has been investigated.
   - The model has been validated verifying successfully testing of a real iTPMS ECU in HIL environment, concerning learning and tire deflation detection phases.

2. **Estimation of Tire Inflation Pressure**

- Exploiting the 2-DOF quarter car model with a road surface profile synthesis model, an IMM filter for tire inflation pressure estimation was developed, which is able to deal with unknown and time-varying road surface unevenness level.
- The quarter car model parameter identification for four different road roughness level according to ISO 8608 classification is considered.
- A constant transition probability matrix is proposed, which assigns to each filter mode the same probability.
- Am IMM filter solutions based on the unscented Kalman estimation technique is presented.
- The IMM is tested on a high-fidelity co-simulation platform. First a Monte Carlo simulation was carried out to compare tire inflation pressure estimation accuracy by the IMM with respect to a single UKF. Then, the capability of the IMMUKF to deal with abruptly change of road surface profile class and tire inflation pressure was verified.

3. **Estimation of Vehicle Sideslip Angle**

- Exploiting the 2-DOF single-track vehicle model with a Dugoff tire model, an IMM filter-based vehicle state estimation algorithm was developed, which is able to cope with different vehicle driving conditions, unlike a single model filter.
- The Dugoff tire model parameter identification for four different tire-road friction scenarios is considered. The benefit of this approach is that it avoids online estimation of tire-road contact models parameters [87, 83].
- A time-varying TPM is proposed, which is able to realize on-line self-learning via a novel model switching algorithm, without any a priori information. TPMs are generally assumed constant and their values are chosen based on a priori information and/or dedicated analysis, posing a challeng on the IMM setup.
- Two IMM filter solutions based on the nonlinear Kalman estimation technique are presented. The first is based on the EKF and the second is based on the UKF. Their performance is assessed and compared in non-trivial driving scenarios, along with a single model filter and an IMM with constant TPM, to validate the time-varying Multiple Model solution proposed.
- The IMM with the most accurate performance is tested on a high-fidelity co-simulation platform based on the MATLAB/Simulink, in order to assess the estimation capability in realistic driving environments.

1.5 Dissertation Outline

The thesis is organised into two sections. The first section deals with the development of a high-fidelity simulation platform. The second section elaborates on the design and validation of algorithms for vehicle state estimation. Chapters 2 and 3 are part of the first section, whereas Chapters 4 and 5 form the second section. The brief description of all the chapters are presented below. The y-axis of some plots reported in the Thesis are normalized respect to the maximum value and other sensitive data are hidden to respect the confidentiality of data of the industrial partner.

Chapter 2: Road Vehicle Modelling and Validation

This chapter presents the high-fidelity vehicle dynamics simulation platform used in Chapter 3 to simulate the vehicle in HIL environment, and to test the estimation algorithms described in Chapter 4 and 5. A description of simulation requirements and modelling approaches adopted are provided, such as a validation process with respect to a high-order model with several degrees of freedom, about 10^2, and validated with experimental data by the industrial partner of the PhD program.

Chapter 3: Vehicle Dynamics Modelling for Testing iTPM with Wheel Speed Sensors in HIL Environment

This chapter presents the modelling approach adopted to simulate the two pressure-dependent phenomena analysed by iTPMS based on wheel speed sensors: reduction of wheel rolling radius; changes of natural frequencies inherent in the angular speed due to tire vibration. A model to simulate effects on wheels dynamics by tire vibration due to its interaction with road roughness has been described. A vector optimization problem was solved to parameterize the model, in order to obtain reliable real-time simulation of wheels angular speed, whose spectrum comply with vehicle road test. Then, a real iTPMS ECU has been tested in HIL environment to verify the functionality of the software release.

Chapter 4: Tire Inflation Pressure Estimation

This chapter presents a novel Interacting Multiple Model Unscented Kalman Filter to estimate VSA without tire-road friction coefficient information. It, integrating four Nonlinear Kalman Filters, each of them with a different set of parameters for vehicle dynamics tire model, is capable to deal with VSA estimation when vehicle driving on different road conditions (dry, wet, damp and snowy asphalt). The efficiency of the proposed estimating scheme in realistic driving scenarios is tested via the high-fidelity co-simulation platform presented in Chapter 2.

Chapter 5: Vehicle Sideslip Angle Estimation

This chapter presents an innovative approach to estimate tire pressure indirectly, without actual road surface roughness information. A quarter car model is used to build four unscented Kalman filters, parameterised to represent vertical vehicle dynamics when driving on a certain level of road surface roughness. These estimators are combined following the Interacting Multiple Model approach, which gives an acceptable estimation of tire stiffness through a weighted average obtained from a probabilistic model. A known linear static relationship between the tire stiffness and inflation pressure is utilized to indirectly estimate the tire inflation pressure. The efficiency of the approach is tested via the high-fidelity co-simulation platform presented in Chapter 2.

Chapter 6: Conclusions

The conclusions of PhD thesis work are presented, and possible future research are proposed.

Chapter 2

Road Vehicle Modelling and Validation

2.1 Simulation platform

Today, computer simulations have become an essential tool to develop and test new and enhanced existing systems for autonomous driving of road vehicles. Usually they are developed in Model-In-the-Loop (MIL) and tested in Hardware-In-the-Loop (HIL) environments. Both environments require a complex simulation platform, whose characteristics can vary considerably from application to application. Basically, it consists of:

- full vehicle model, so that every physical component accurately represents and mimics their real behaviors;
- maneuver and driver model, for providing driving instructions for accelerating, braking, and steering the vehicle model;
- road model, that provides information on the road the vehicle moves on;
- fellow vehicles model, needed for simulation of various traffic situations and complex scenarios;
- models for moving objects, like pedestrians, and static objects, like variable traffic signs, traffic lights, parked vehicles, houses;
- sensors models, to simulate perception of surrounding environment;
- models for radio interference, as well as shadowing by static and moving obstacles, needed for network simulation.

Research purpose is to develop and test algorithms for estimating dynamics state of the ego-vehicle. Simulation requirements correspond to those on which are based vehicle dynamics simulation platforms, typically used for testing vehicle dynamics ECUs. Therefore, it must involve full vehicle, road, maneuver and driver models. Indeed, these are strictly need to predict the movements of the simulated vehicle on a particular road in response to both control and disturbance inputs, generating so inputs and measurements suitable for vehicle dynamics state estimation purpose. Models for road traffic and network simulation, as well as sensors models for surrounding environment perception are not considered to avoid unnecessary complexity. The simulation platform, developed with the tool suite of dSPACE software Automotive Simulation Model (ASM), is schematized in Figure 2.1. It is composed of three layers, i.e. the driver layer, vehicle layer and road layer.

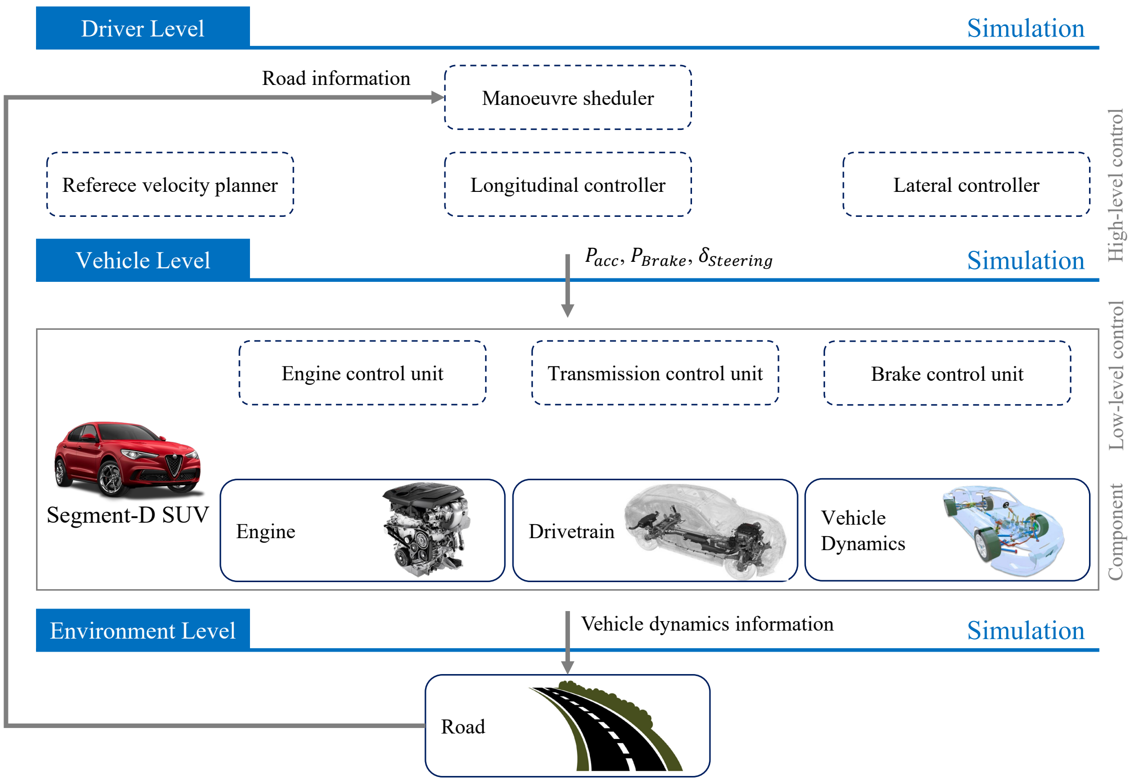

Fig. 2.1 Schemtic of simulation platform.

2.1.1 Driver Model

The first consists of models essential to perform maneuvers, i.e. predefined sequences of driving instructions for simulating a variety of driving situations with the vehicle model. It controls accelerator pedal, brake pedal and steering wheel in such a way that the vehicle follows a given reference velocity while driving on an arbitrary road. The task of controlling the vehicle is split into sub-tasks for longitudinal control, lateral control, and reference velocity calculation for driving on roads.

Longitudinal Controller

The longitudinal controller controls accelerator pedal, brake pedal and selector lever. The controller strategy, proposed in [94], comprises feed forward and feedback control. The feed forward controller calculates the accelerator and brake pedal positions according to the required driving situation using a simplified inverse dynamics model of the vehicle. The feedback controller decreases the velocity error by closing the control loop. A conditionally driven state machine, schematized in Figure 2.2, is implemented to continuously check the driving situation and set selector lever to the right position.

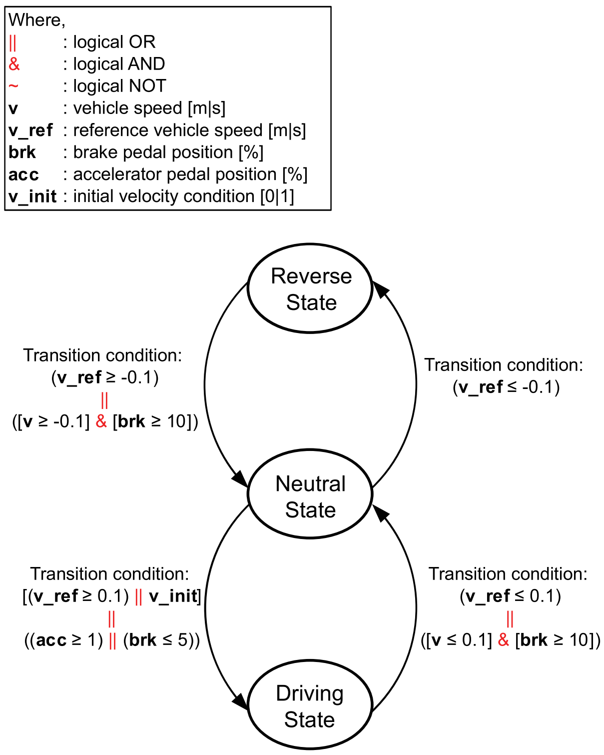

Fig. 2.2 Conditionally driven transition from one state to another for the selector lever.

Reference Velocity Calculation

Model are also implemented for the calculation of the reference velocity for the longitudinal controller [94]. The vehicle must be prevented from cornering too fast while following a road. Suitable vehicle speeds in road curves and suitable accelerations are needed. Velocity profile generation starts by determining the velocity limits for road turns (horizontal road profile) and slopes (vertical road profile) ahead. For simplification purposes, the road friction and bank angle are neglected, which leads to the following equation:

$$v_{x,lim} = \sqrt{\frac{a_{y,max}}{r_{road,y}}} \tag{2.1}$$

where, $v_{x,lim}$ is the tangential component of the driving velocity limit, $a_{y,max}$ is the maximum lateral driver acceleration, and $r_{road,y}$ is the road horizontal curvature. The generated reference speed is also adapted according to the vertical road profile according to the following equation:

$$v_{x,lim} = \sqrt{\frac{a_{z,max/min} cos\left(\beta_{road}\right)}{r_{road,z}}} \tag{2.2}$$

where, $a_{z,max/min}$ is the maximum driver deflection and rebound vertical acceleration, β_{road} is the road pitch angle, and $r_{road,z}$ is the vertical road curvature. The reference speed $v_{x,ref}$ is then found by integrating the following differential equation, obtained by combining the above equations:

$$dv_{x,ref}\left(s_{Vehicle}\right) = \pm \frac{a_{x,max/min}}{v_{x,ref}\left(s_{Vehicle}\right)} \sqrt[n_{GG}]{1 - \left(\frac{v_{x,ref}\left(s_{Vehicle}\right)^2 r_{road,y}\left(s_{Vehicle}\right)}{a_{y,max}}\right)^{n_{GG}}} ds_{Vehicle} \tag{2.3}$$

where, $s_{Vehicle}$ is the distance driven by vehicle on road, $a_{x,max/min}$ is the maximum longitudinal driver acceleration as well as deceleration, and n_{GG} is the *g*-*g* diagram exponent used to form different driving patterns. The driving style depends on the driver parameters and takes effect when the vehicle is approaching a stop or a turn, during cornering, after leaving a turn, and when accelerating from lower to higher vehicle speeds. At this point, a *g*-*g* diagram is used in an idealized form to characterize the driver. This adapted form of the *g*-*g* diagram is written as follows:

$$\left(\frac{a_x}{a_{x,max/min}}\right)^{n_{GG}} + \left(\frac{a_y}{a_{y,max/min}}\right)^{n_{GG}} \leq 1 \tag{2.4}$$

where, a_x is the longitudinal acceleration, and a_y is the lateral acceleration generated by the curved path. Adapting $a_{x,max/min}$, $a_{y,max}$, and n_{GG} produces different driver characters [1], as shown in Figure 2.3. To find the maximum velocity to cover a road distance according to the driver parameters, the road horizontal curvature $r_{road,y}$ of the upcoming road is collected

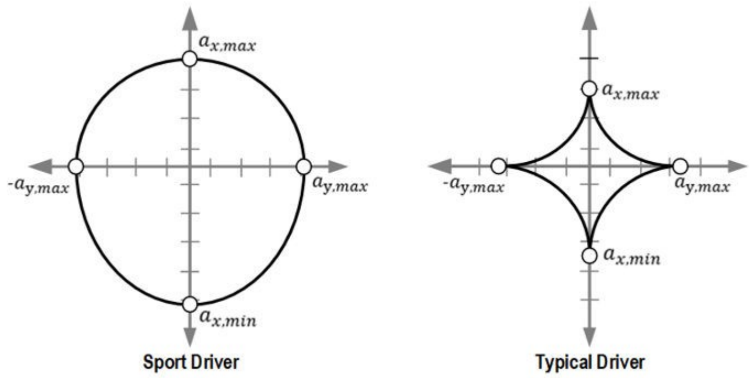

Fig. 2.3 Conditionally driven transition from one state to another for the selector lever [1].

from the Road model according to a preview distance

$$s_{Previev,LongCtrl} = \frac{v_{x,Vehicle}^2}{2|a_{x,min}|} \tag{2.5}$$

where, $v_{x,Vehicle}$ is the longitudinal vehicle velocity, and $a_{x,min}$ is the maximum longitudinal driver deceleration.

Lateral Controller

The implemented lateral controller was proposed in [95] and [2]: based on linear optimal control theory, controller algorithm keeps the vehicle on the road by controlling the steering wheel. Figure 2.4 is a schematic of the control concept. It uses preview information and and is based on a linear single-track model. Defined $v_{x,Vehicle}$ and $v_{y,Vehicle}$ the components of vehicle velocity $v_{Vehicle}$, $Pos_{x,Vehicle}$ and $Pos_{y,Vehicle}$ the vehicle position, $\varphi_{Vehicle}$ the yaw angle, and treating $v_{x,Vehicle}$ as fixed, the linear single-track model in state space form becomes:

$$\begin{aligned} \dot{x} &= Ax + Bu \\ y &= Cx, \end{aligned} \tag{2.6}$$

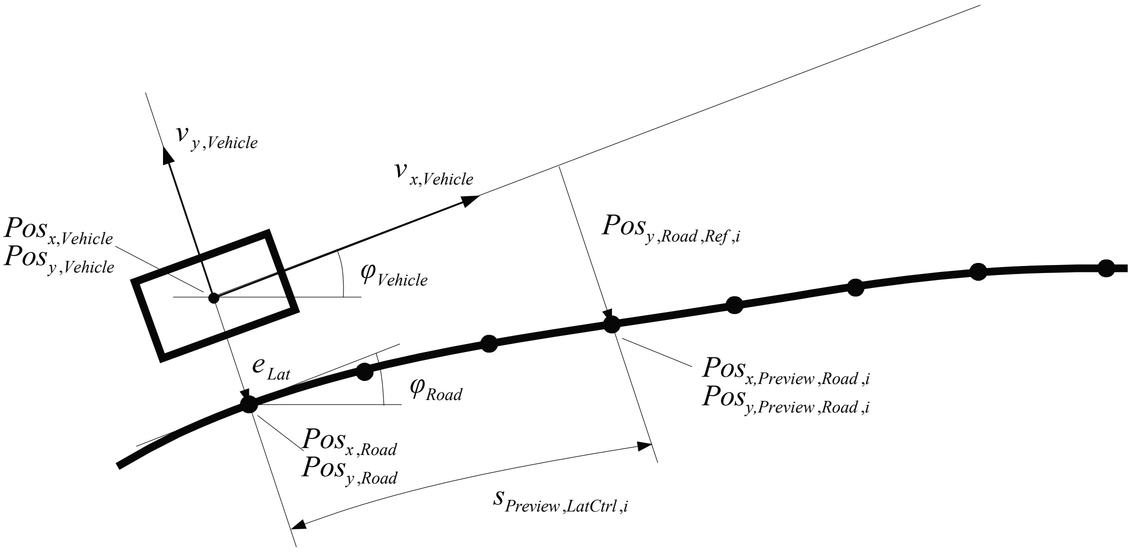

Fig. 2.4 Scheme of the lateral control concept [2].

where, $x = \left[Pos_{y,Vehicle}, v_{y,Vehicle}, \dot{\varphi}_{Vehicle}, \varphi_{Vehicle}\right]^T$ is the state vector, while $y = Pos_{y,Vehicle}$ is the output signal. The linearized model equations are [96]:

$$\dot{x} = \begin{bmatrix} 0 & 1 & 0 & v_{x,Vehicle} \\ 0 & \frac{-2(c_F+c_R)}{m_{Vehicle}v_{x,Vehicle}} & \frac{2(a_2c_R-a_1c_F)}{m_{Vehicle}v_{x,Vehicle}} - v_{x,Vehicle} & 0 \\ 0 & \frac{2(a_2c_R-a_1c_F)}{J_{Vehicle}v_{x,Vehicle}} & \frac{-2\left(a_1^2c_F+a_2^2c_R\right)}{J_{Vehicle}v_{x,Vehicle}} & 0 \\ 0 & 0 & 1 & 0 \end{bmatrix} x + \begin{bmatrix} 0 \\ \frac{2c_F}{m_{Vehicle}} \\ \frac{2a_1c_F}{J_{Vehicle}} \\ 0 \end{bmatrix} \delta_{Steering} \tag{2.7}$$

where, c_F and c_R are the cornering stiffness for front and rear wheels, a_1 and a_2 are the front and rear semi-wheelbases, $m_{Vehicle}$ is the vehicle mass, $J_{Vehicle}$ is the inertia moment of the vehicle about the z-axis, and $\delta_{Steering}$ is the wheel steering angle. Given a sample time T and a number of $n_{LatCtrl}$ preview points, at discrete time points $i_{LatCtrl}T$ is known to be

$$y\left(i_{LatCtrl}T\right) = C\Phi\left(i_{LatCtrl}T\right)x(0) + C\Gamma\left(i_{LatCtrl}T\right)Bu(0) \tag{2.8}$$

where, $\Phi(kT) = e^{Ai_{LatCtrl}T}$, and $\Gamma\left(i_{LatCtrl}T\right) = \int_0^{i_{LatCtrl}T}\Phi(t)\,dt$. The controller minimizes the following objective function, defined as the sum at a number of $n_{LatCtrl}$ preview points of the weighted difference between output signal and reference signal, y_{Ref}, [95]:

$$J = \sum_{i_{LatCtrl}=1}^{n_{LatCtrl}} \left(y_{Ref}\left(i_{LatCtrl}T\right) - y\left(i_{LatCtrl}T\right)\right)^2 W_k \tag{2.9}$$

The controller uses as reference signal the y-component of the reference positions in vehicle coordinates, $y_{Ref} = Pos_{y,Road,Ref,i}$, calculated as:

$$\begin{aligned} Pos_{y,Road,Ref,i} = & \left(Pos_{y,Preview,Road,i} - Pos_{y,Vehicle}\right) cos\varphi_{Vehicle} \\ & - \left(Pos_{x,Preview,Road,i} - Pos_{x,Vehicle}\right) sin\varphi_{Vehicle} \end{aligned} \tag{2.10}$$

where, $Pos_{x,Preview,Road,i}$ and $Pos_{y,Preview,Road,i}$ are x and y coordinates for the preview points in earth coordinates, evaluated from the road model

$$\begin{bmatrix} Pos_{x,Preview,Road,i} \\ Pos_{y,Preview,Road,i} \end{bmatrix} = Road\left(s_{Vehicle} + s_{Preview,LatCtrl,i}\right) \tag{2.11}$$

according to the preview distance $s_{Preview,LatCtrl,i}$, calculated as the distance the vehicle moves in the preview time $t_{Preview}$

$$s_{Preview,LatCtrl,i} = i_{LatCtrl} T v_{Vehicle} t_{Preview} \tag{2.12}$$

After derivation of J with respect to $u(0)$, $\frac{dJ}{du(0)}$, the control law can be calculated in closed form, assuming that the control input is kept constant over the whole preview interval. In the implemented controller, a number of $n = 10$ preview points are used, with a preview time $t_{Preview} = 1\ s$, resulting in a sample time $T = 1/10\ s = 0.1\ s$. With $u(0) = \delta_{Steering}$ the control law is

$$u(0) = \frac{\sum_{i_{LatCtrl}=1}^{10} \left(Pos_{y,Road,Ref,i} - C\Phi\left(i_{LatCtrl}T\right)x(0)\right)\left(C\Gamma\left(i_{LatCtrl}T\right)BW_k\right)}{\sum_{i_{LatCtrl}=1}^{10} \left(\left(C\Gamma\left(i_{LatCtrl}T\right)B\right)^2 W_k\right)} \tag{2.13}$$

2.1.2 Road Model

The Road model provides information about the road the vehicle moves on. This information is forwarded to both the vehicle and driver models. Roads are described in terms of horizontal profile, vertical profile, lanes and road surface conditions, modelled as junctions and road elements. On junction elements, the road properties are described as a function of the local x and y coordinates on the junction plate. The following properties can be defined for junction elements: shape of the junction border line; lane properties of connection points; height of the junction plate; special surface properties such as low friction areas or bumps; position markers. On road elements, the position of any point near the road is described by the distance traveled along the reference line, measured from the start point of the road, and the distance perpendicular to the reference line, as shown in Figure 2.5. All properties of road elements are defined as a function of this distance along the reference line, independently of the particular segments that define the horizontal profile. The following properties can be

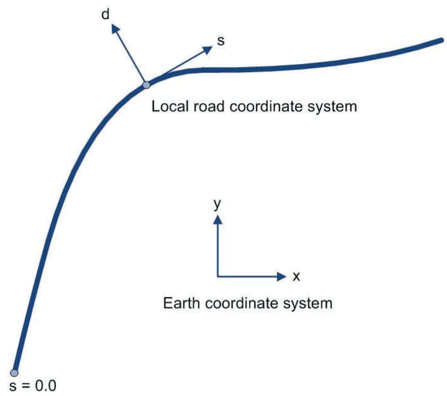

Fig. 2.5 Points position on road elements.

defined for each road element: height profile; lateral slope profile; lane sections; road scenery sections; special surface properties such as low friction areas or bumps. The road model computes preview points to forward to driver controllers information on upcoming road. It also supplies tire-road contact point information. On junction elements, the properties are calculated in the local coordinate system of the junction plate. Since for road elements the properties are defined as a function of the distance along the road, the road model first calculates the distance along the road s_{CP} and the lateral offset perpendicular to the road reference line d_{CP} that corresponds to the x- and y-position of the tire contact point on the horizontal plane, $Pos_{x_{CP}}$ and $Pos_{y_{CP}}$, respectively, i.e.

$$[s_{CP}, d_{CP}] = f\left(Pos_{x_{CP}}, Pos_{y_{CP}}\right) \tag{2.14}$$

The following variables at the tire-road contact point are then calculated:

- road height $z_{CP} = f\left(s_{CP}, d_{CP}\right)$;
- unit vector in the direction of road normal $e_{zCP} = f\left(s_{CP}, d_{CP}\right)$;
- road friction coefficient $\mu_{CP} = f\left(s_{CP}, d_{CP}\right)$;
- surface condition $SC_{CP} = f\left(s_{CP}, d_{CP}\right)$.

2.1.3 Full Vehicle Model

The full vehicle model plays a key role for the simulation platform. It must provides a good representation of the vehicle system to be controlled, in order that any inconsistencies or implausibility can not be detected. For this purpose, model of each component the whole vehicle system must be developed, including engine, drivetrain, vehicle body and four wheels, which all come together with component-level control models (Soft ECUs) to create the full vehicle model. The developed full vehicle model concerns conventional vehicle with internal combustion engine and automatic transmission. It consists of:

- Engine model, the power source of the drivetrain, that computes the torque resulting from both the combustion and the engine speed;
- Drivetrain, that transfers the torque from the engine to the wheels. The drivetrain model simulates several components, i.e.
  - Torque converter, that transfers the engine torque to the transmission system;
  - Gearbox, that converts the engine speed and engine torque with different gear ratios to the rest of the drivetrain;
  - Differentials, that transmits the power from the transmission to the wheels.
- Vehicle dynamics, that manages the following systems:
  - Aerodynamics, represented by aerodynamics forces and torques acting on the vehicle sprung mass;
  - Axle dynamics/kinematics, result of suspension kinematics and suspension forces in the spring, shock absorber, and stabilizer;
  - Tire, that generates tractive and/or cornering forces;
  - Steering, that transfers the steering wheel angle defined by the driver to a movement of the steering rod.
  - Brake, that generates brake torque at each wheel.
  - Wheel dynamics, represented by the rotational wheel movement, which is function of torques applied to the wheel axle;
  - Vehicle body dynamics, represented by the motion of the vehicle and the vertical wheel movements, which are functions of tires, aerodynamics, suspension, and mass forces and torques.

To run properly the vehicle components models, four Soft ECUs models are needed, which simulate the performance of ECUs. In detail:

- Soft ECU engine, that controls the engine torque to a desired value by the driver, as a function of actual engine speed and accelerator pedal position;

- Soft ECU transmission, that manages the gearshift process of an automatic transmission. It controls the lockup clutch engagement, the gear according to a predefined shift strategy, and a torque reduction while shifting gears;
- Soft ECU body, that controls the engine start button to start and shut down the engine;
- Soft ECU brake, that controls the brake pressure to a desired value by the driver, as a function of brake pedal position.

Developing the component models that best represent the vehicle systems involved several topics, including:

- Defining the needs for each subsystem's modeling and simulation. The model should rigorously adhere to these constraints, both functional and non-functional, in order to achieve desired behavior and accuracy without adding needless complexity.
- Defining the interfaces the model will use to send and receive information from other models and controllers.
- Determining how and what physical effects should be modeled. This is essential for making the model function correctly and for deciding the kind of model that will be developed.
- Identifying what assumptions and restrictions will be taken into account and applied to the model. These will enable models to be appropriately adjusted using reasonable techniques.

All of the component models address each of the bulleted points. These lay the groundwork for a complete vehicle model that can satisfy all of its requirements. Throughout next Chapter the vehicle system components are explored in regards to their requirements and the development of their model.

2.2 Road Vehicle Modelling

The model components are outlined in this chapter. Implementation variants, the importance of components models for the testing purposes, and modeling tools are described in individual cases. In particular, the individual requirements for vehicle component model, interfaces, physical effects to be modeled, and assumptions and limitations were derived from a variety of sources including an estimation on the level of fidelity needed, and available data on the real-world subsystem. The modelled road vehicle is a segment-D compact crossover SUV produced by the industrial partner of the Ph.D. course, equipped with a 2.2 L I4 Multijet II 210 CV AT8 Q4 engine, a 8-speed automatic transmission with torque converter, a double wishbones suspension in the front axle, and a multi-link suspension in the rear axle.

2.2.1 Engine Model

Engine Simulation Requirements

The engine model was made to mimic a real-world internal combustion engine. To create such a model, requirements relating to both the functionality and the constraints of the system were defined. For vehicle dynamics investigations, as well as for energy consumption analyses, only fuel, torque, and speed needed to be obtained from an engine model. Indeed, the model of the combustion process is not needed to simulate the amount of energy used and torque produced and transferred to the drivetrain. Specifically, the engine model must be able to receive a torque request and a speed as inputs. These would be used along with static maps to find outputs such as, torque, fuel rate used and engine efficiency. Real system constraints, such as the maximum and the minimum speed, the maximum torque output, and the maximum fuel rate possible, must be taken into account for engine modeling. Setting these restrictions, utilizing suitable performance maps, and putting in place suitable Input/Output interfaces led to the creation of an engine model that could replicate actual expected behavior.

Engine Model Development

During the research activity, the Diesel engine 2.2 L I4 Multijet II 210 CV AT8 Q4 has been modelled, whose main characteristics are reported in Table 2.1, and full-load torque and power data are shown in Figure 2.6. To test vehicle dynamics control systems, a simple

Table 2.1 Datasheet of Diesel engine 2.2 L I4 Multijet II 210 CV AT8 Q4.

Type	Characteristic	Type	Characteristic
Configuration	Inline-4	Stroke/Bore	99×83.8 mm
Displacement	2143 cm^3	Compression Ratio	15.5:1
Valvetrain	DOHC	No. valves per cylinder	4
Turbocharger	Variable-geometry	Fuel system	Common Rail
Max. power @ rpm	154 kW @ 3750 rpm	Max. torque @ rpm	470 Nm @ 1750 rpm

look-up table based combustion engine is needed, and was created to be low fidelity. The model only contains signals and information pertinent to the engine, while no actuator or sensor logic are included. In particular, a first order engine map-based model was developed,

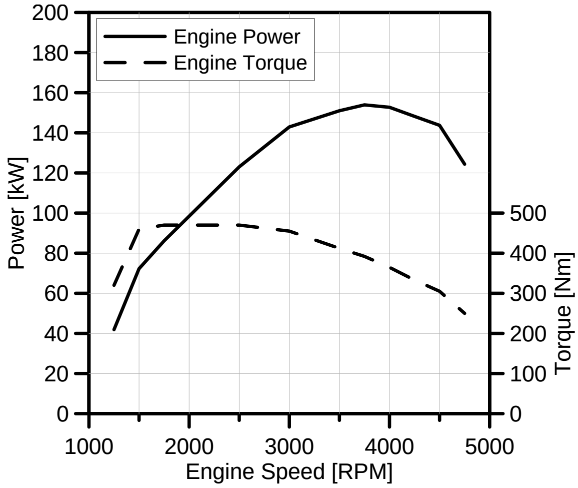

Fig. 2.6 Engine full-load torque and power.

consisting of only one state ω_{ICE}, engine angular velocity, ignoring the intake manifold filling dynamics. The dynamics of ω_{ICE} is given by

$$J_{ICE}\dot{\omega}_{ICE} = Trq_{ICE} - Trq_{load} \tag{2.15}$$

where, J_{ICE} is the engine crankshaft equivalent inertia, Trq_{ICE} is the effective internal combustion engine torque exerted on the crankshaft, and Trq_{load} is the load torque from the torque converter. The transient values of Trq_{ICE} as manifold pressure in the intake manifold varies and reaches steady state are ignored. To obtain an estimation of fuel rate, the energy flows within the powertrain and the vehicle are reproduced. In particular, a forward modeling approach is used, which reproduces the physical causality of the system, and so computes the evolution of vehicle speed as the result of the dynamic simulation, and not prescribed a-priori, as shown in Figure 2.7. Each powertrain component is modeled using an efficiency map, a power loss map, or a brake-specific fuel consumption map: these give a relation between the losses in the component and the actual operating conditions (averaged during the desired time interval). The fuel mass flow rate $\dot{m}_{fuel}$ is then computed by multiplying the brake-specific fuel consumption b_e with the engine power:

$$\dot{m}_{fuel} = Trq_{ICE}\,\omega_{ICE}\,b_e \tag{2.16}$$

Then, by integrating this value (divided by fuel density) over time, it is possible to obtain the total fuel consumption. Regarding the specific fuel consumption b_e, an analytical model is used [97], rather then a brake-specific fuel consumption map. In particular, the engine

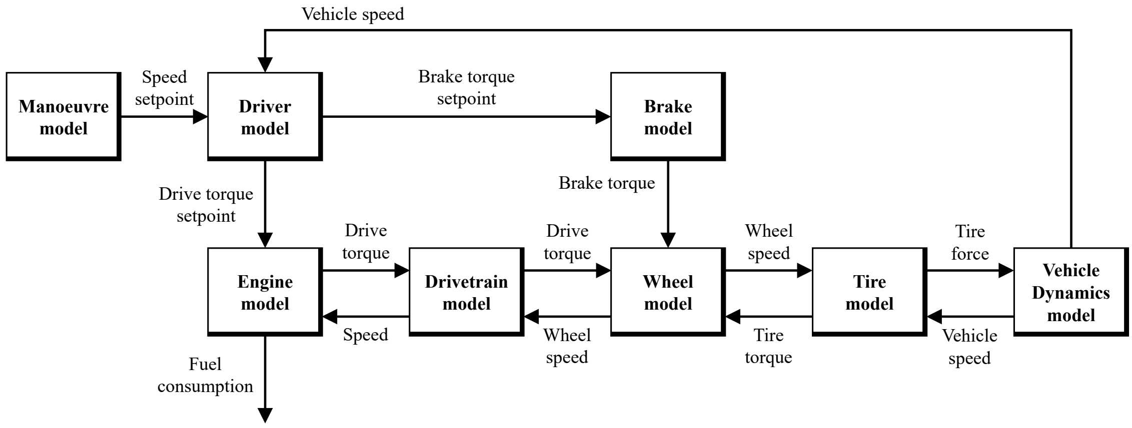

Fig. 2.7 Information flow with the forward approach.

efficiency is computed as a function of engine load and speed through two coefficients, μ_P and μ_n respectively. Defined the maximum engine efficiency as η_{max}, the instantaneous engine efficiency η_{ICE} is given by:

$$\eta_{ICE} = \eta_{max}\mu_P\mu_n \tag{2.17}$$

where $\mu_P = f\left(P_{ICE}/P_{ICE_{max}}\right)$ expresses the influence of the degree of power utilization on the engine efficiency, while $\mu_n = f\left(\omega_{ICE}/\omega_{ICE_{max}}\right)$ expresses the influence of the engine speed on the efficiency. To evaluate these two coefficients, the dependency of engine efficiency by instantaneous engine power P_{ICE_i} and speed ω_{ICE_j} must be determined. To this purpose, experimental data of several diesel engines at full and partial loads, with max. power and displacement comparable with the engine to be modelled, were used. Specifically, in this analysis experimental data-set of five Diesel engines have been used, listed in Table 2.2. For each of them, the efficiency map has been determined. Figure 2.8 shows efficiency

Table 2.2 Experimental data-set of Diesel engines.

Engine	Max. power	Ref.
3.0 L TDI	255 hp	[3]
2.5 L TDI	174 hp	[98]
1.6 L TDI	110 hp	[99]
2.5 L TDI	140 hp	[100]
3.0 L TDI	249 hp	[101]

map of the 3.0 L TDI 255 hp engine, for example purpose. The three-dimensional surface of the form $\eta_{ICE} = f\left(P_{ICE}, \omega_{ICE}\right)$ has been split into two two-dimensional vectors of the form $\eta_{ICE_P} = f\left(P_{ICE}\right)$ and $\eta_{ICE_\omega} = f\left(\omega_{ICE}\right)$. To determine the dependency of efficiency by instantaneous engine power the two-dimensional vector η_{ICE_P} has been used. Specifically,

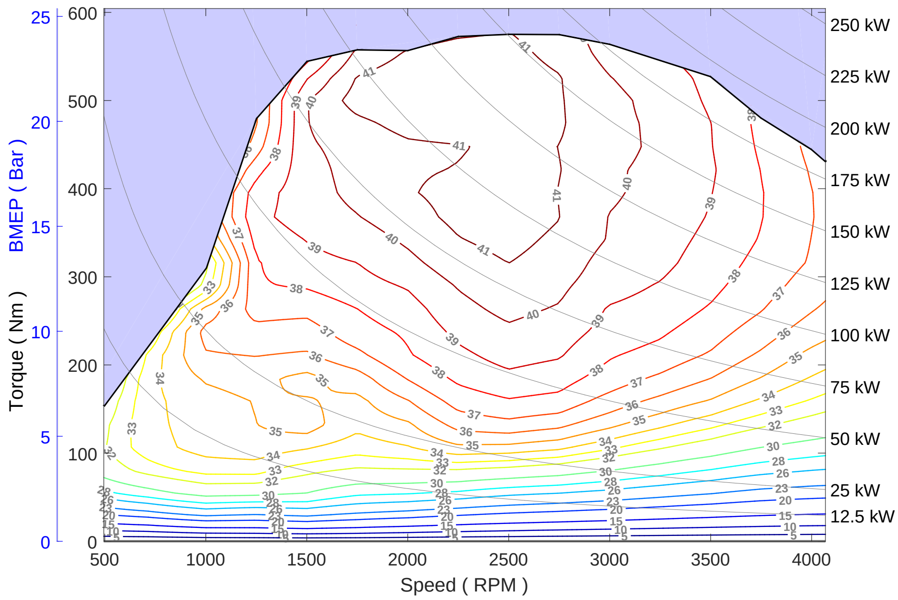

Fig. 2.8 3.0 L TDI 255 hp efficiency map [3]

fixed the engine speed to a specific value ω_{ICE_j}, defined $P_{ICE_{max,j}}$ the maximum engine power achievable at ω_{ICE_j}, and defined $\eta_{ICE_{P,max,j}}$ the maximum engine efficiency achievable at ω_{ICE_j}, it is possible to evaluate the trend of the engine efficiency normalized with respect to the maximum value $\eta_{ICE_P}/\eta_{ICE_{P,max,j}}$ as a function of the engine power normalized with respect to the maximum value $P_{ICE_j}/P_{ICE_{max,j}}$, as shown in Figure 2.9a. Repeating the procedure for all other engine speeds, an average $\eta_{ICE_P}/\eta_{ICE_{P,max}}$ trend can be computed over the entire engine operating range, as shown in Figure 2.9b. Figure 2.10 shows the range that includes the average trends $\eta_{ICE_P}/\eta_{ICE_{P,max}}$ as a function of $P_{ICE}/P_{ICE_{max}}$ for the five engine considered. In turn, their average (dashed black line), that well approximates the whole range of values and, therefore, considered suitable also for the engine to be simulated, can be used to compute the coefficient μ_P. Specifically, μ_P has been numerically reconstruct though third order polynomial:

$$\mu_P = a_P + b_P\left(\frac{P_{ICE}}{P_{ICE_{max}}}\right) + c_P\left(\frac{P_{ICE}}{P_{ICE_{max}}}\right)^2 + d_P\left(\frac{P_{ICE}}{P_{ICE_{max}}}\right)^3 \tag{2.18}$$

where, the coefficients a_P, b_P, c_P and d_P have been tuned to reproduce the average trend, as shown in Figure 2.11a. The same calculation scheme has been applied to determine the dependency of efficiency by instantaneous engine speed, this time using the two-dimensional vector η_{ICE_ω}. So the trend $\eta_{ICE_\omega}/\eta_{ICE_{\omega,max}}$ as a function of $\omega_{ICE}/\omega_{ICE_{max}}$, averaged over the

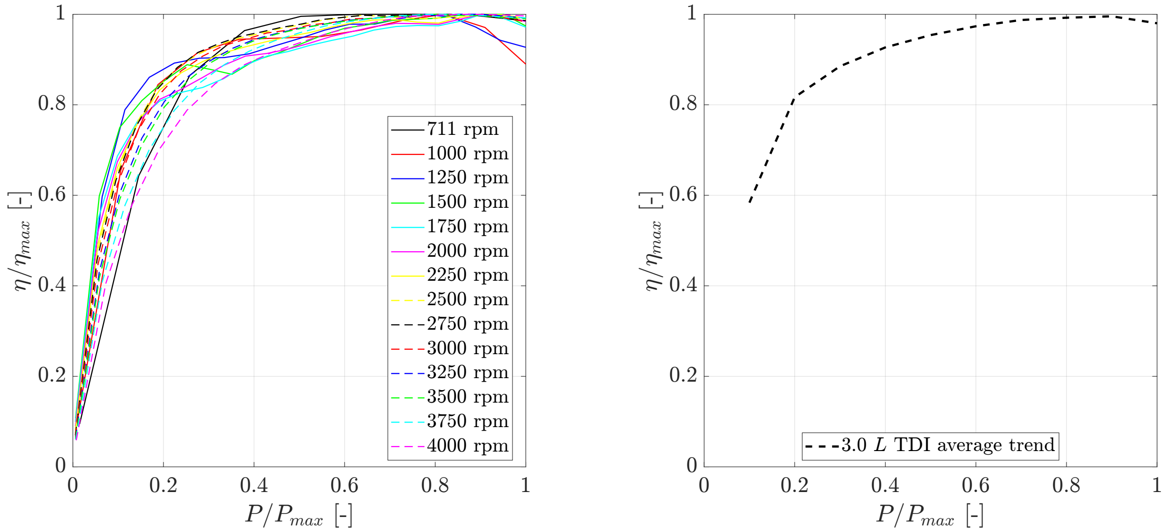

(a) Normalized engine efficiency trend for several speeds.

(b) Normalized engine efficiency trend averaged over several speeds.

Fig. 2.9 Efficiency of 3.0 L TDI 255 hp engine as function of load.

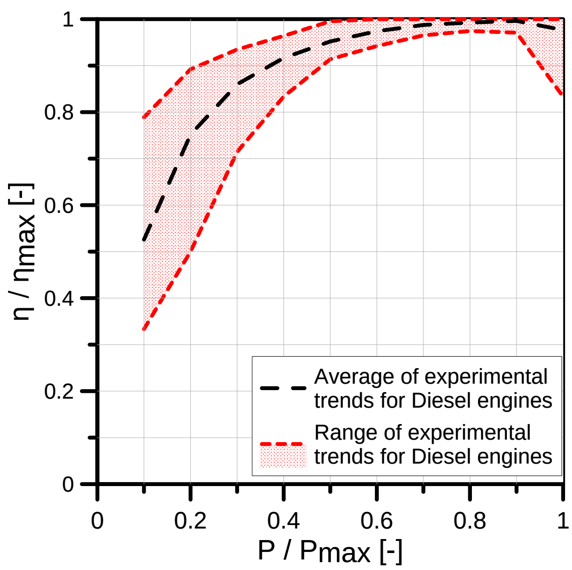

Fig. 2.10 Experimental data of five Diesel engines at full and partial loads: efficiency as function of load.

five diesel engines, have been determined, and used to numerically reconstruct μ_n, as:

$$\mu_n = a_n + b_n \left(\frac{\omega_{ICE}}{\omega_{ICE_{max}}}\right) + c_n \left(\frac{\omega_{ICE}}{\omega_{ICE_{max}}}\right)^2 + d_n \left(\frac{\omega_{ICE}}{\omega_{ICE_{max}}}\right)^3 \tag{2.19}$$

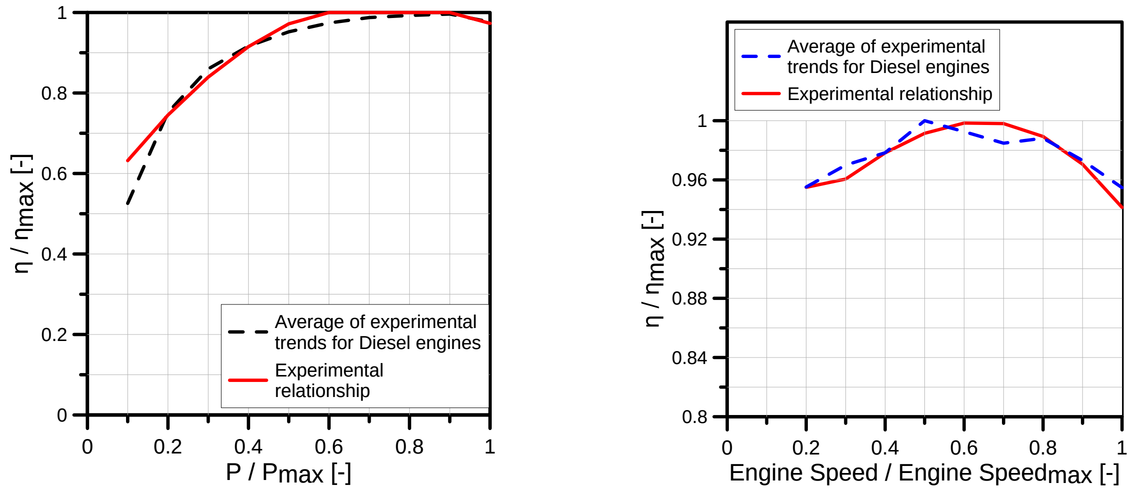

(a) Engine efficiency as function of load. (b) Engine efficiency as function of speed.

Fig. 2.11 Reconstruction of the average normalized efficiency trends.

where, the coefficients a_n, b_n, c_n and d_n have been tuned to reproduce the average trend, as shown in Figure 2.11b. The analytical model for the computation of engine efficiency allows to determine the efficiency over the entire operating range of the engine starting from the only knowledge of maximum efficiency η_{max}, as shown in Figure 2.12.

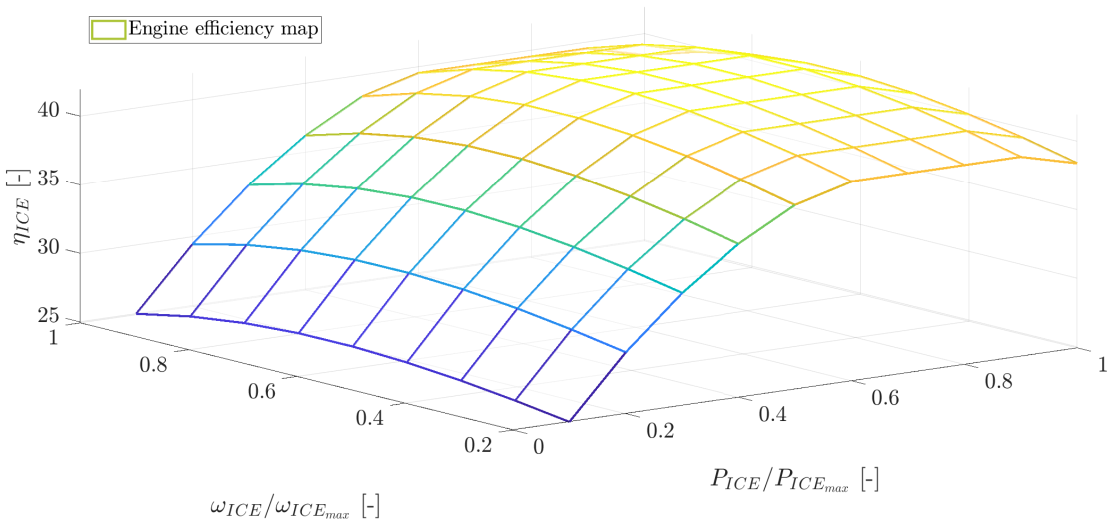

Fig. 2.12 Analytical modelling of the engine efficiency map.

2.2.2 Drivetrain Model

Drivetrain Simulation Requirements

The simulation of drivetrain, based on torque converter, gearbox, and differential models, have to mimic the real-world systems at low fidelity. It only must converts the engine speed and engine torque with different gear ratios to the wheels. The torque converter has the functional requirement to transfer the engine torque to the gearbox. It must allows the car come to a complete stop without stalling the engine, and must gives the car more torque when it accelerates out of a stop. In particular, as the speed increases, the transmission catches up to the engine with, however, difference in speeds, which result in wasted power. Therefore, when the two halves of the torque converter get up to speed, a lockup clutch must rigidly connects the engine crankshaft to the input shaft of gearbox, avoiding constant slipping at high speed. The automatic transmission model need to use the gear command that is set by the Soft ECU of transmission to select the proper gear ratio. The model is required to have the proper gear ratios for each gear selection and it also needed to apply the gear ratio multiplication to the torque being transferred through the model. An efficiency to the torque was also required to take into account the transmission losses. The drivetrain configuration is Rear Wheel Drive (RWD), where the torque is transferred from the gearbox output shaft to the rear wheels throughout a differential. In particular, the differential has three tasks: to transfer the engine power to the rear wheels; to act as the final gear reduction in the vehicle, e.g. by slowing the rotational speed of the transmission before it reaches the wheels; to transmit the power to the wheels while allowing them to rotate at different speeds; this is mainly needed for driving in a curve with the outer wheels having to run faster than the inner wheels. The non-functional requirements for each model were directly related to the functional requirements. Having the correct gear ratios and the correct efficiency ensured that the model was constrained within the real-world limitations on the transmission.

Drivetrain Model Development

This section contains a description of models used to reproduce the behaviour of the principal drivetrain components. Figure 2.13 shows the scheme of the modelled system, composed of an 8-speed automatic transmission ZF 8HP75 750 Nm, whose main characteristics are reported in Table 2.3, and a final drive in RWD configuration, where a differential gives a final drive ratio of $f_{ratio} = 3.27$ [-]. The automatic transmission is composed of a model of the torque converter to compute the torque transferred from the engine to the gearbox, and a gearbox model that changes the gear ratio from the engine to the rest of the drivetrain. The final drive is composed of a differential model, that computes the torque transferred

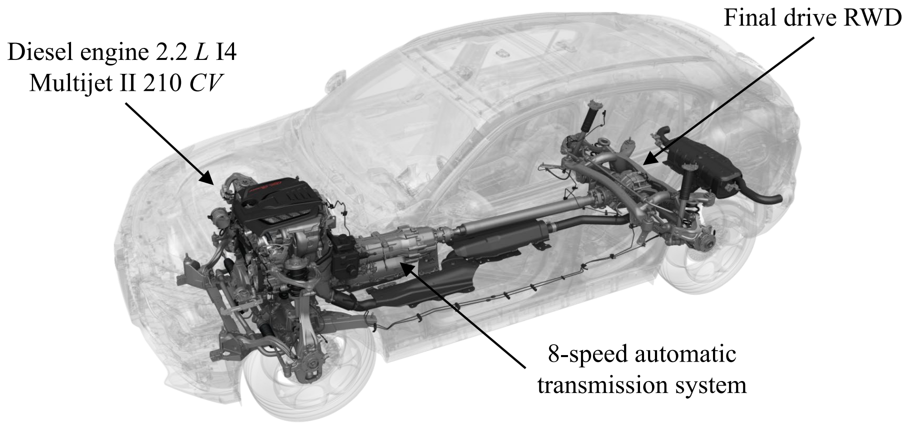

Fig. 2.13 Drivetrain scheme [4].

Table 2.3 Main characteristics of the ZF 8HP75 750 Nm.

Gear	Ratio	Planetary gear-set: Teeth
1	5.0000	
2	3.2000	Sun 1:48 Ring 1:96
3	2.1429	
4	1.7200	Sun 2:54 Ring 2:96
5	1.3139	
6	1.0000	Sun 3:60 Ring 3:96
7	0.8221	
8	0.6400	Sun 4:24 Ring 4:96
R	-3.4560	

from the transmission system to the rear wheels. Modelling approach adopted for all these elements is suitable for energy flow analysis, as shown in Figure 2.14, neglecting component dynamics. Detailed behavioral models accurately accounting for dynamic effect are beyond the objectives of the simulation. The torque converter, through a fluid coupling mechanism,

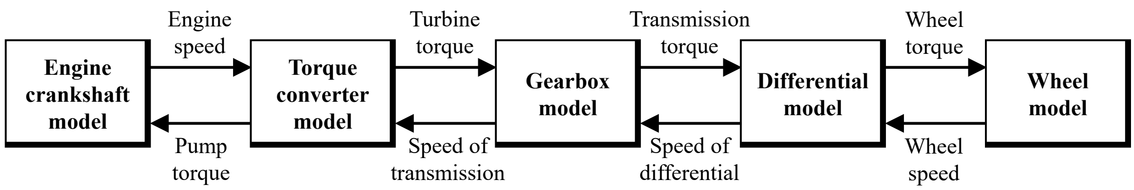

Fig. 2.14 Information flow in vehicle drivetrain.

is utilized to transfer motion from the engine to the input shaft of the gearbox. Since engine torque is transferred by fluid-dynamic forces rather than friction or pressure, it can multiply engine torque and has extremely high dampening capabilities. A pump, a turbine, and a stator in between make up the torque converter. The coupling between the turbine and the pump is through a transmission fluid. The pump is mounted on the engine crankshaft and accelerates the oil flowing to the turbine inside the converter. From the turbine, the oil flows through the stator back to the pump. If the pump speed is greater than turbine speed, the torque converter increases the turbine torque. If the pump speed is nearly equal to the turbine speed, the converter works as a hydraulic clutch and transmits the pump torque to the turbine shaft. The engine's flywheel is attached to the pump's fins; therefore, the pump rotates with a speed ω_{TC_p} equal to the engine one, $\omega_{TC_p} = \omega_{ICE}$, and, similarly, the pump torque Trq_{TC_p} is equal to the engine torque, $Trq_{TC_p} = Trq_{ICE}$. The gearbox is coupled to the turbine, so, as the same manner of the pump, the turbine speed ω_{TC_t} is equal to the input shaft speed of gearbox $\omega_{gear_{in}}$, $\omega_{TC_t} = \omega_{gear_{in}}$, as well as the turbine torque Trq_{TC_t} is equal to the input shaft torque of gearbox $Trq_{gear_{in}}$, $Trq_{TC_t} = Trq_{gear_{in}}$. The torque at the turbine is multiplied with respect to the pump torque, thanks to the presence of the stator which modifies the flow characteristics inside the converter. The torque multiplication increases with the speed difference between the pump and the turbine. However, this difference in speed wastes power, therefore a lockup clutch model is opportunely controlled to reduce the slippage and improve the efficiency. The torsional damper assembly of the torque converter is here neglected. Figure 2.15 shows a schematic of a torque converter. A torque converter

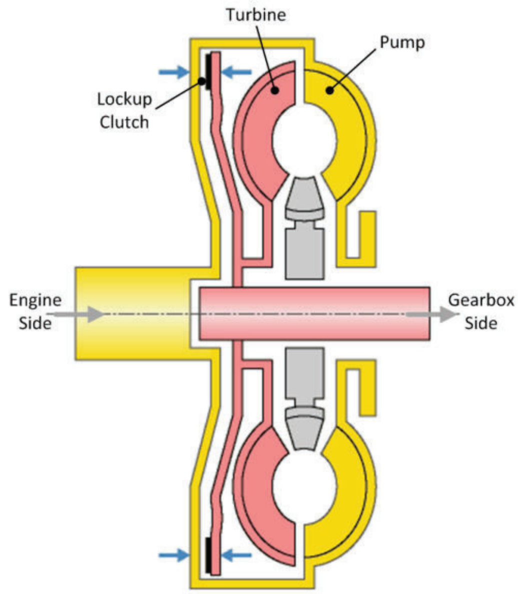

Fig. 2.15 Schematic of a torque converter [5].

static model is used [102] because of its simplicity, and since it has a reasonable agreement with the real system behaviour for a fairly wide range of operating conditions. It is based on tabulated characteristics of torque ratio Trq_{TC_t}/Trq_{TC_p} and capacity factor K_{TC} versus speed

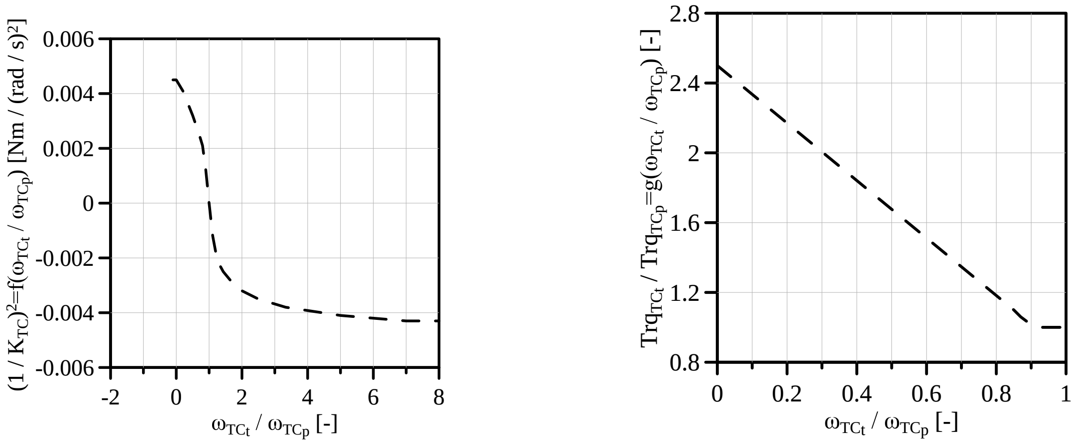

(a) K_{TC} map.

(b) Torque ratio map.

Fig. 2.16 Torque converter characteristic curves.

ratio $\omega_{TC_t}/\omega_{TC_p}$. The capacity factor, defined as

$$K_{TC} = \frac{\omega_{TC_p}}{\sqrt{Trq_{TC_p}}} \tag{2.20}$$

is a measure of how much torque the torque converter can transmit, which can be determined by its characteristic curve reported in look-up table of Figure 2.16a. Then, the pump torque cab be calculated as:

$$Trq_{TC_p} = \left(\frac{1}{K_{TC}^2}\right)\omega_{TC_p}^2 = f\left(\frac{\omega_{TC_t}}{\omega_{TC_p}}\right)\omega_{TC_p}^2 \tag{2.21}$$

Using the characteristic curve of the torque ratio reported in look-up table of Figure 2.16b, it is possible to compute the turbine torque as:

$$Trq_{TC_t} = g\left(\frac{\omega_{TC_t}}{\omega_{TC_p}}\right)Trq_{TC_p} \tag{2.22}$$

A model of lockup clutch is used to mechanically connect and disconnect the engine to and from the rest of the drivetrain. It is modeled as two plates, and the torque is transferred via friction between them. In this model, no torsion spring is used. The bristle friction model [103] is used to model the friction torque which arises between the plates. The model is based on the assumption that the contact between the two surfaces acts like elastic bristles. As a result of the exerted torque, each bristle can deflect and the deflection torque can be

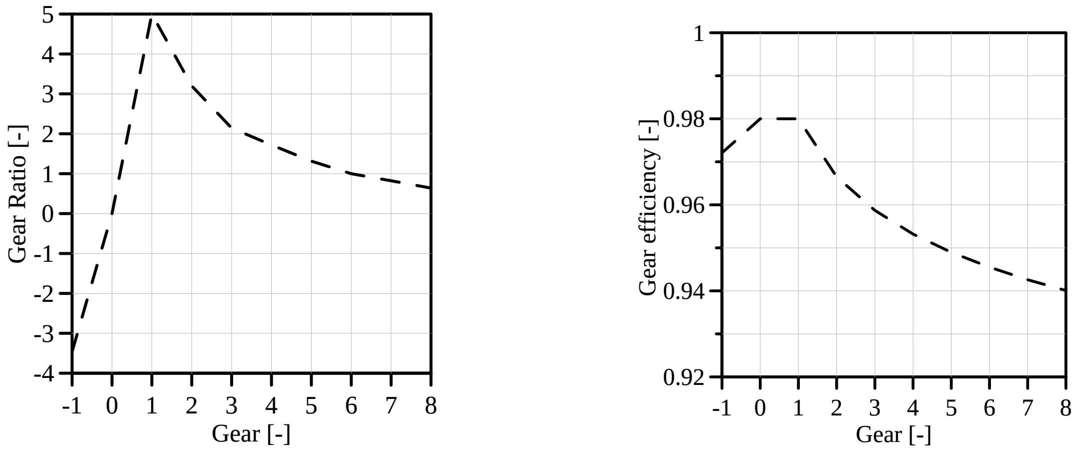

(a) Gear ratio map.

(b) Gear efficiency map.

Fig. 2.17 Gearbox model look-up tables.

described by a damper and a spring. The friction torque Trq_{Fric} can be formulated as follows:

$$Trq_{Fric} = k_{Fric}\Delta\theta_{Clutch} + c_{Fric}\Delta\omega_{Clutch} \tag{2.23}$$

where, k_{Fric} is the equivalent stiffness coefficient of the friction model, c_{Fric} is the equivalent damping coefficient of the friction model, $\Delta\theta_{Clutch}$ is the twist angle difference between the input and output side of the lockup clutch, and $\Delta\omega_{Clutch}$ is the relative velocity between the input and output side of the lockup clutch. The resulting friction torque is limited by the lockup clutch torque capacity $Trq_{Fric_{Lim}}$, which is a function of the maximum clutch torque $Trq_{Fric_{Max}}$ and the clutch pedal position P_{Clutch}:

$$Trq_{Fric_{Lim}} = \frac{100 - P_{Clutch}[\%]}{100} Trq_{Fric_{Max}} \tag{2.24}$$

The engagement and disengagement of the lockup clutch is controlled by the transmission soft ECU: when it is engaged the friction torque is summed to both turbine and pump torques. The turbine torque Trq_{TC_t}, output of the torque converter model, is the input of the gearbox model. A simple map-based gearing model is used, which involve two look-up tables for the evaluation of the gear ratio of current gear g_{ratio}, in Figure 2.17a, and gear efficiency η_{gear} to take into account of power losses due to friction, in Figure 2.17b, respectively. This efficiency is only considered for the torque calculation, i.e., speed-dependent efficiency is neglected. At steady state operation under a specific gear of the transmission, the torque of the gearbox $Trq_{gear_{out}}$ is calculated as:

$$Trq_{gear_{out}} = \begin{cases} \eta_{gear} g_{ratio} Trq_{gear_{in}}, & \text{if } g_{ratio} Trq_{gear_{in}} \geq 0 \\ \frac{g_{ratio} Trq_{gear_{in}}}{\eta_{gear}}, & \text{if } g_{ratio} Trq_{gear_{in}} < 0 \end{cases} \tag{2.25}$$

while, the relation between the gear ratio and gearbox speed $\omega_{gear_{out}}$ is:

$$\omega_{gear_{in}} = g_{ratio} \omega_{gear_{out}} \tag{2.26}$$

To describe the dynamics during a gear change, the gear ratio in eq. 2.25 and 2.26 is replaced according to the following 1st order equation during a gear change:

$$\tau_{sync} \dot{g}_{ratio} + g_{ratio} = g_{ratio_{unsync}} \tag{2.27}$$

where, τ_{sync} is the synchronization time constant, and $g_{ratio_{unsync}}$ is the unsynchronized gearbox transmission ratio. A rule-based gear shift strategy is used to control the vehicle transmission. In particular, strategy's rules are derived solving a multi-objective optimization. Figure 2.18 shows the results of the optimization task, reporting the gearshift logic used for the automatic transmission gearbox. The final drive is modelled in RWD configuration, in Figure 2.19a,

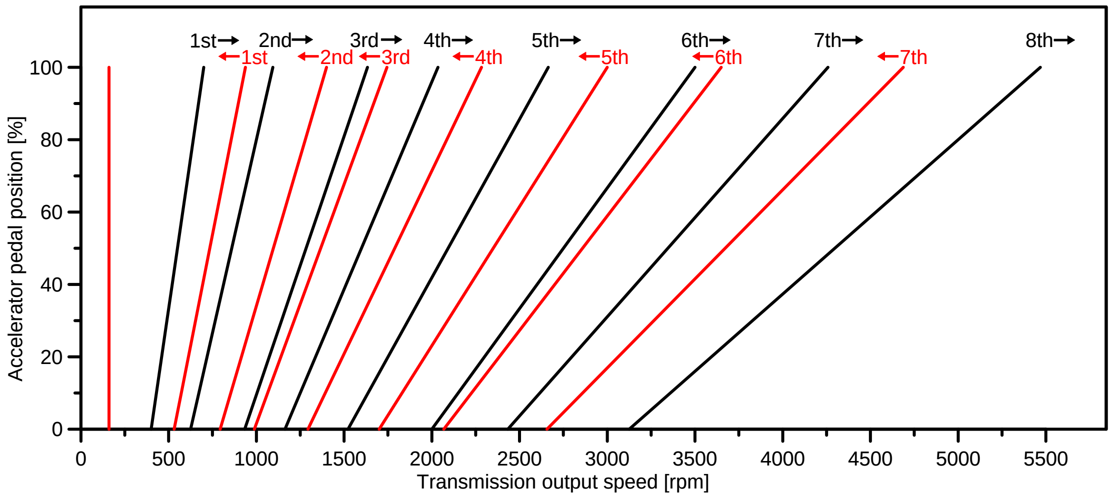

Fig. 2.18 Automatic transmission gearshift logic.

and consists of a model of the differential with a constant torque distribution ratio to transfers torque from a transmission to the wheels, in Figure 2.19b. The following simple model is

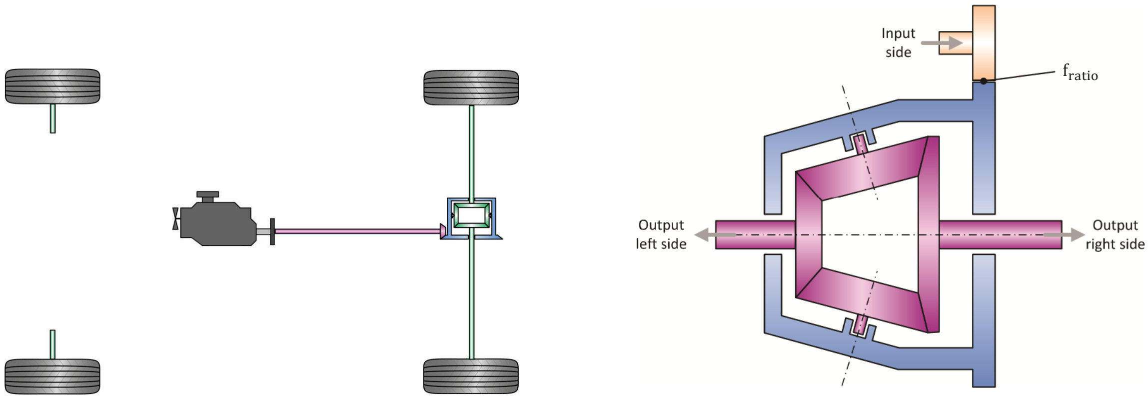

(a) Drivetrain configuration. (b) Schematic of the differential.

Fig. 2.19 Schematic of the final drive [6].

used to simulate and analyze system performance:

$$Trq_{Wheel_{RL}} = Trq_{Wheel_{RR}} = \frac{1}{2} Trq_{gear_{out}} f_{ratio} \tag{2.28}$$

$$\omega_{gear_{out}} = \frac{1}{2} \left(\omega_{RL} + \omega_{RR}\right) f_{ratio} \tag{2.29}$$

where, f_{ratio} is the final drive ratio, $Trq_{Wheel_{RL}}$ and $Trq_{Wheel_{RR}}$ are the torques transferred at shafts of left and right rear wheels, respectively, $\omega_{Wheel_{RL}}$ and $\omega_{Wheel_{RR}}$ are the speeds of left and right rear wheels, respectively.

2.2.3 Vehicle Dynamics Model

Vehicle Dynamics Simulation Requirements

The vehicle dynamics simulation plays a key role to develop and test algorithms for estimating dynamics state of the vehicle. It must reliable predicts the movements of the simulated vehicle on a particular road in response to both control and disturbance inputs, in order that any inconsistencies or implausibility can not be detected. The output of the simulation, i.e. the predicted vehicle dynamics states, set the stage for testing estimation algorithms, since can be used for generating variables of input needed by the algorithms to operate, as well as reference generation for evaluation of estimation accuracy. The main components in vehicle dynamics simulation are complex systems and demanded more in-depth models than did the other systems in the vehicle. In particular, the model simulates a passenger car composed of 5 bodies, vehicle body and four wheels, characterized by 15 Degrees of Freedom (DOF): 6

DoF for vehicle body motion; 4 DOF for wheel vertical relative motion; 1 DOF for steering; 4 DOF for wheel rotation. In detail, the vehicle dynamics is recreated by seven models:

- vehicle movement model, where the multibody system (MBS) technique is used to write the equation of motion, in order to calculate the motion of the vehicle and the vertical wheel movements as functions of tires, aerodynamics, suspension, and mass forces and torques;
- aerodynamics model, that computes equivalent aerodynamic forces and torques as a function of vehicle velocity, air density, velocity and incidence angle of wind;
- suspension model, represented by multidimensional look-up tables, computes suspension kinematics, i.e. the relative position of the wheel center, the orientation of the wheel, the spring-damper-stabilizer movements of two generalized coordinates (vertical wheel movements of left and right sides) and steering rod displacement for both front and rear suspension. The movements of the spring, damper, and stabilizer are calculated to determine the forces that they exert through a map-based approach;
- tire model, where, starting from wheel states (i.e., velocity and orientation), the contact point states are calculated and passed on to a semi-empirical model to calculate the tire forces and moments. According to the orientation of the contact point coordinate system, these forces and moments are then oriented in the vehicle reference system;
- wheel speed model, that computes the wheel speed from a 1^{st} order equation describing its dynamics;
- steering model, composed of a steering column, steering transmission, and steering rod, computes a steering torque at the steering column from the relative angle coming from the driver and the steering gear that is calculated from the steering rod dynamics. A simple one degree of freedom steering model is considered, where the generalized degree of freedom is the displacement of the steering rod, since detailed behavioral, models which include electronic power steering model, are beyond the objectives of the simulation;
- brake model, that consists of a simple model that computes an additional torque that reduces the net torque acting on the tire as a function of the brake input signal. Detailed model of the brake hydraulics are beyond the objectives of the simulation.

To ensure the proper representation of real-world behavior in all the models, the use of real performance data is necessary. The limitations that vehicle dynamics systems would see in use in the vehicle needed to be included in the models as well. Figure 2.20 shows a schematic of the main components in vehicle dynamics simulation. During the research activities a

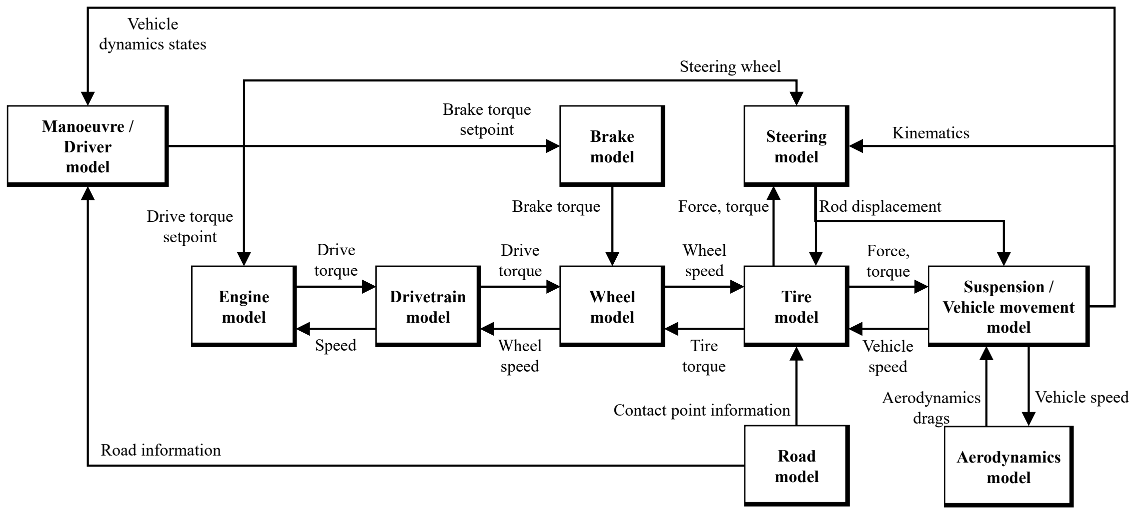

Fig. 2.20 Schematic of the main components in vehicle dynamics simulation.

segment-D compact crossover SUV has been modelled, based on Giorgio platform, with double wishbones suspension in the front, and multi-link suspension in the rear, whose main characteristics are listed in Table 2.4. Following Sections describe the main components in

Table 2.4 Segment-D SUV vehicle characteristics.

Quantity	Value	Quantity	Value
Mass $m_{Vehicle}$	1788 kg	Height of the center of mass h_g	0.6 m
Front semi-wheelbase a_1	1.347 m	Rear semi-wheelbase a_2	1.471 m
Front track width t_1	1.606 m	Rear track width t_2	1.6364 m
Yaw moment of inertia $J_{Vehicle}$	3230 kgm^2	Weight distribution	50/50 [-]
Drag coefficient C_x	0.32 [-]	Frontal area A_x	2.75 m^2
Front suspension	double wishbones	Rear suspension	multi-link
Tires	235 65 R17 104W Michelin	Steering ratio	5625 deg/m

vehicle dynamics simulation.

Vehicle Movement Model Development

The model simulates the motion of the vehicle body and the vertical wheel movements. To this purpose, the vehicle is modelled by multibody system. The vehicle body is modeled by one rigid body with 6 DOF, as well as each of the wheels is modelled by one rigid body with 1 DOF in vertical direction. Figure 2.21 shows the four coordinate systems, all rotating clockwise, used to describe the kinematics of vehicle dynamics:

- earth coordinate system, index E represents the fixed reference system;

- vehicle reference coordinate system, index V is fixed to the vehicle body. Its origin is at zero position at mid-point between the front wheel centers. The x-axis is in the longitudinal direction of the vehicle and points forwards, the y-axis points towards the vehicle's left side, and the z-axis direction follows the right-hand rule and points upwards;
- wheel coordinate system, index W is at the wheel center. Its orientation is determined by the wheel orientation, which depends on the suspension kinematics;
- contact point coordinate system, index CP its origin is at the contact point. The x-y plane is parallel to the road local plane.

To be note that, in symbols used the superscript of a variable indicates the coordinate system in which the variable is described, while, the subscript indicates the relevant body of the variable. The generalized degrees of freedom are listed in detail below. The translatory

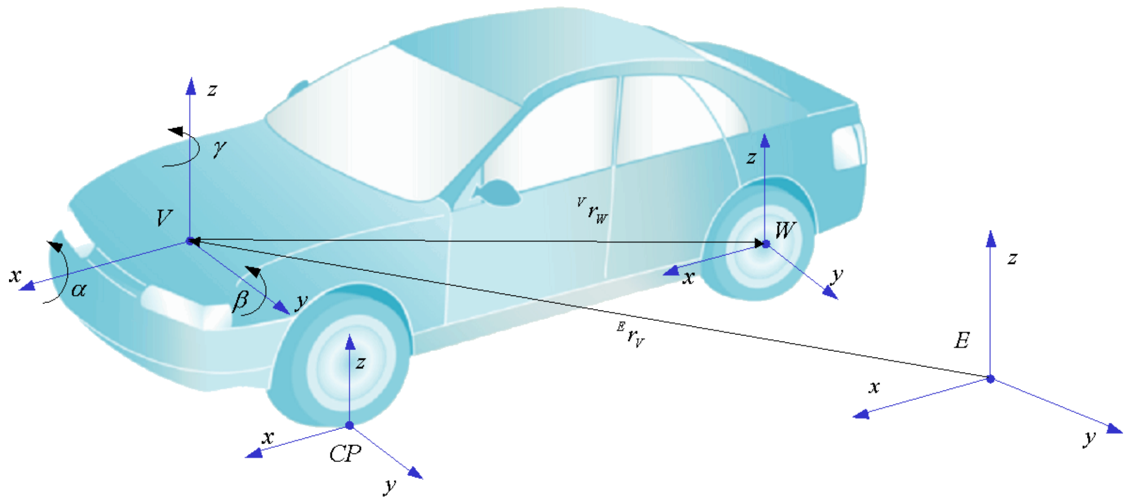

Fig. 2.21 Schematic of the main components in vehicle dynamics simulation [6].

vehicle velocities of the origin of coordinate system V in x, y, and z directions described in vehicle reference coordinate system V

$$\begin{bmatrix} \dot{q}_1 \\ \dot{q}_2 \\ \dot{q}_3 \end{bmatrix} = \begin{bmatrix} v_x \\ v_y \\ v_z \end{bmatrix}_V^V \tag{2.30}$$

The angular vehicle velocities about the x, y, and z-axes of vehicle reference coordinate system V

$$\begin{bmatrix} \dot{q}_4 \\ \dot{q}_5 \\ \dot{q}_6 \end{bmatrix} = \begin{bmatrix} \omega_x \\ \omega_y \\ \omega_z \end{bmatrix}_V^V \tag{2.31}$$

The vertical speed of the wheel represented in vehicle reference coordinate system V

$$\begin{bmatrix} \dot{q}_7 \\ \dot{q}_8 \\ \dot{q}_9 \\ \dot{q}_{10} \end{bmatrix} = \begin{bmatrix} \dot{z}_{W1} \\ \dot{z}_{W2} \\ \dot{z}_{W3} \\ \dot{z}_{W4} \end{bmatrix}_V^V \tag{2.32}$$

The position of the vehicle-fixed axis system V with respect to the earth-fixed axis system E is described by the components x, y, z of the position vector E_{Pos_V}, calculated by integrating the vehicle velocity in the vehicle reference coordinate system, V_{v_V}, transformed in the earth coordinate system, as:

$$E_{Pos_V} = E_{Pos_{V,0}} + \int \left(E_{T_V} V_{v_V} \right) dt \tag{2.33}$$

Its orientation is defined by the rotation matrix E_{T_V}, given by the product

$$E_{T_V} = T_\varphi T_\beta T_\alpha \tag{2.34}$$

that can be expressed as

$$E_{T_V} = \begin{bmatrix} cos(\varphi) & -sin(\varphi) & 0 \\ sin(\varphi) & cos(\varphi) & 0 \\ 0 & 0 & 1 \end{bmatrix} \begin{bmatrix} cos(\beta) & 0 & sin(\beta) \\ 0 & 1 & 0 \\ -sin(\beta) & 0 & cos(\beta) \end{bmatrix} \begin{bmatrix} 1 & 0 & 0 \\ 0 & cos(\alpha) & -sin(\alpha) \\ 0 & sin(\alpha) & cos(\alpha) \end{bmatrix} \tag{2.35}$$

where, *varphi* denotes the yaw angle and β and α characterize the pitch and roll motion. Each wheel is supposed to be fully balanced. Then, its center is located on the rotation axis. As a consequence, the position of each wheel is defined by the vector $E_{Pos_{Wi}}$ in the earth coordinate system as follows:

$$E_{Pos_{Wi}} = E_{Pos_V} + E_{T_V} V_{Pos_{Wi}} \tag{2.36}$$

with $i \in \{1, \ldots, 4\}$, and where E_{Pos_V} is the vehicle position in the earth coordinate system. If the rotation matrices $V_{T_{Wi}}$, with $i \in \{1, \ldots, 4\}$, describe the orientation of each wheel-fixed axis system relative to the vehicle-fixed axis system, then the rotation matrices

$$E_{T_{Wi}} = E_{T_V} + E_{T_V} V_{T_{Wi}} \tag{2.37}$$

define their orientation with respect to the earth-fixed axis system. The suspension model describes the position and orientation of each wheel. In particular, the vertical motion z_{w_i} of each wheel $i \in \{1, \ldots, 4\}$ relative to the chassis is used to characterize wheel motion. A rack-and-pinion steering system is used at the front axle, so the rack movement q_{St} at the front axle fully describe the steering motion. Then, the position and orientation of each wheel center relative to the vehicle-fixed axis system is defined at the front $(i \in \{1,2\})$ by

$$V_{Pos_{Wi}} = V_{Pos_{Wi}}\left(z_{w_i}, q_{St}\right) \tag{2.38}$$

$$V_{T_{Wi}} = V_{T_{Wi}}\left(z_{w_i}, q_{St}\right) \tag{2.39}$$

Instead, the position and orientation of each wheel center relative to the vehicle-fixed axis system is defined at the rear $(i \in \{3,4\})$ as a function of z_{w_i} and wheel vertical displacement at the opposite side $z_{w_{i,Opposite}}$:

$$V_{Pos_{Wi}} = V_{Pos_{Wi}}\left(z_{w_i}, z_{w_{i,Opposite}}\right) \tag{2.40}$$

$$V_{T_{Wi}} = V_{T_{Wi}}\left(z_{w_i}, z_{w_{i,Opposite}}\right) \tag{2.41}$$

Expressing the absolute velocity and the absolute angular velocity of the vehicle-fixed axis system in this axis system results in

$$V_{v_V} = \left(E_{T_V}\right)^T E_{v_V} \tag{2.42}$$

$$V_{\omega_V} = \begin{bmatrix} \dot{\alpha} \\ 0 \\ 0 \end{bmatrix} + \left(T_\alpha\right)^T \left\{ \begin{bmatrix} 0 \\ \dot{\beta} \\ 0 \end{bmatrix} + \left(T_\beta\right)^T \begin{bmatrix} 0 \\ 0 \\ \dot{\varphi} \end{bmatrix} \right\} = \begin{bmatrix} 1 & 0 & -sin(\beta) \\ 0 & cos(\alpha) & sin(\alpha)cos(\beta) \\ 0 & -sin(\alpha) & cos(\alpha)cos(\beta) \end{bmatrix} \begin{bmatrix} \dot{\alpha} \\ \dot{\beta} \\ \dot{\varphi} \end{bmatrix} \tag{2.43}$$

where, E_{V_V} is the velocity of the vehicle-fixed axis system V with respect to the earth-fixed axis system E, and V_{ω_V} is the angular vehicle velocities about the axes of vehicle reference coordinate system V. Now, the absolute velocity and the angular velocity of the vehicle center of gravity (CoG), $V_{V_{CoG}}$ and $V_{\omega_{CoG}}$, are defined as follows:

$$V_{v_{CoG}} = V_{v_V} + V_{\omega_V} \times V_{Pos_{CoG}} \tag{2.44}$$

$$V_{\omega_{CoG}} = V_{\omega_V} \tag{2.45}$$

where, $V_{Pos_{CoG}}$ is the position of (CoG) in the vehicle reference coordinate system V. And for the wheel center, at first, the time derivative of eq. 2.36 results in the absolute velocities of the wheels centre in the earth-fixed axis system E

$$E_{v_{Wi}} = E_{v_V} + E_{\omega_V} \times E_{T_V} V_{Pos_{Wi}} + E_{T_V} V_{\dot{Pos}_{Wi}} \tag{2.46}$$

with $i \in \{1, \dots, 4\}$, where, E_{ω_V} absolute angular velocity of the vehicle-fixed axis system in the earth-fixed axis system E, and $V_{\dot{Pos}_{Wi}}$ is the velocity of each wheel center relative to the vehicle-fixed axis system. Next, the transformation into the vehicle-fixed axis system yields to the :

$$V_{v_{Wi}} = V_{v_V} + V_{\omega_V} \times V_{Pos_{Wi}} + V_{\dot{Pos}_{Wi}} \tag{2.47}$$

Similarly, the absolute angular velocities of the wheels centre in the vehicle-fixed axis system, $V_{\omega_{Wi}}$, are written as

$$V_{\omega_{Wi}} = V_{\omega_V} + V_{\omega_V} \times V_{Pos_{Wi}} + V_{\omega_{Wi,rel}} \tag{2.48}$$

where, $V_{\omega_{Wi,rel}}$ is the angular velocity of each wheel center relative to the vehicle-fixed axis system. The equation of motion can be generated via Jordain's principle of virtual power [104], and is provided by the following first-order differential equation:

$$M\ddot{q} = Q_L \tag{2.49}$$

where, $\ddot{q}$ is the $[10 \times 1]$ degrees of freedom vector. Q_L is the $[10 \times 1]$ generalized forces and torques in the direction of the relevant degrees of freedom. Indeed, the forces and torques applied to each body can be transformed via the partial velocities and the partial angular velocities to the corresponding generalized forces and torques. Defined E_{V_i} the velocity vector with which a body i is moving relative to the earth-fixed axis system E in this reference system, and E_{ω_i} vector of the angular velocities relative to the earth-fixed axis system E in this reference system, the contribution of the 5 bodies to the vector of generalized forces and torques is given by:

$$Q_L = \sum_{i=1}^{5} \left[\frac{\partial E_{V_i}^T}{\partial \dot{q}} \left(F_i^a - m_i E_{a_i}^R \right) + \frac{\partial E_{\omega_i}^T}{\partial \dot{q}} \left(Trq_i^a - \Theta_i E_{\alpha_i}^R - E_{\omega_i} \times \Theta_i E_{\omega_i} \right) \right] \tag{2.50}$$

combines the inertia and gyroscopic forces and torques with F_i^a and Trq_i^a, which represent the external forces and torques (tire, aerodynamics, mass forces, and torques and suspension forces and torques) applied to body i. In the equation, m_i is the mass of the body i, Θ_i

denotes the inertia tensor of body i, $E^R_{a_i}$ and $E^R_{\alpha_i}$ the remaining terms in the linear and angular accelerations. M is the $[10 \times 10]$ generalized mass matrix, which is calculated at every simulation step as a function of the wheel position and kinematic suspension relations, as follows:

$$M = \sum_{i=1}^{5} \left[\frac{\partial E^T_{V_i}}{\partial \dot{q}} m_i \frac{\partial E_{V_i}}{\partial \dot{q}} + \frac{\partial E^T_{\omega_i}}{\partial \dot{q}} \Theta_i \frac{\partial E_{\omega_i}}{\partial \dot{q}} \right] \tag{2.51}$$

Aerodynamics Model Development

The effects of aerodynamics are represented by aerodynamics forces and torques acting on the vehicle sprung mass. The aerodynamics forces and torques are applied in the aerodynamics coordinate system, located in the ground plane (x-y plane) at the middle of the wheelbase and track width. The forces and torques are calculated as follows:

$$\begin{aligned}
F_{Aero,x} &= -\tfrac{1}{2}\rho_{Air}\Delta v^2 C_x(\tau_{Wind})A_x \\
F_{Aero,y} &= -\tfrac{1}{2}\rho_{Air}\Delta v^2 C_y(\tau_{Wind})A_x \\
F_{Aero,z} &= \tfrac{1}{2}\rho_{Air}\Delta v^2 C_z(\tau_{Wind})A_x \\
Trq_{Aero,x} &= \tfrac{1}{2}\rho_{Air}\Delta v^2 C_{Mx}(\tau_{Wind})A_x l_{wheelbase} \\
Trq_{Aero,y} &= -\tfrac{1}{2}\rho_{Air}\Delta v^2 C_{My}(\tau_{Wind})A_x l_{wheelbase} \\
Trq_{Aero,z} &= -\tfrac{1}{2}\rho_{Air}\Delta v^2 C_{Mz}(\tau_{Wind})A_x l_{wheelbase}
\end{aligned} \tag{2.52}$$

where, Δv is the difference between the velocity of vehicle and wind $\Delta v = (v_{Vehicle} - v_{Wind})$, ρ_{Air} is the density of air, A_x is the longitudinal shadow area of the vehicle, $l_{wheelbase}$ is the vehicle wheelbase, C_x, C_y, C_z, C_{Mx}, C_{My}, C_{Mz} are the the aerodynamics coefficients, and τ_{Wind} is the angle of incidence of wind. As can be seen from above equations, the aerodynamics coefficients are dependent on the angle of incidence. This dependency is calculated in the model through look-up tables.

Suspension Model Development

Suspension orientation is described with three rotation angles which are defined with respect to wheel coordinate system: α_{Wheel} (rotation about x-axis), β_{Wheel} (rotation about y-axis) and γ_{Wheel} (rotation about z-axis). They are defined with certain relation to camber, caster and toe angles, which is a conventional way to define wheel orientations on a vehicle:

- camber angle is an angle between the vertical axis of wheel and vertical axis of vehicle when viewed from front or rear. Positive camber is when the distance from upper part of the wheel to the vehicle is greater than the lower part. For the left side of vehicle, positive camber angle nearly equals to the negative α_{Wheel} angle about x axis;

- caster is an angle to which the steering pivot axis is tilted forward or rearward from vertical, as viewed from left or right side of vehicle. Positive caster angle is when the upper pivot line is leaned backward father than bottom pivot. The positive caster angle nearly equals to the negative β_{Wheel} about y axis when viewed from each side of vehicle;

- toe angle identifies the exact direction the tires are pointed comparing to the longitudinal axis of the vehicle when viewed from top. Positive toe, or toe in, which means the front of the wheel pointing in towards the centerline of the vehicle, is nearly equal to a negative γ_{Wheel} for left side of the vehicle. The definition of toe out is the other way round.

Because a right-handed coordinate system is used, the left wheel positive toe angle is a negative rotation about the z-axis, the positive camber angle is a negative rotation about the x-axis, and the positive caster angle is a negative rotation about the y-axis. Therefore, the positive camber, caster and toe angle are in accordance with the negative α_{Wheel}, β_{Wheel} and γ_{Wheel}. The suspension model reproduce the kinematics of vehicle suspension system. For front suspension system, it calculates the relation of wheel position with respect to the displacement of steering rack and vertical wheel displacement of wheel, the relation of wheel angular velocity with respect to the velocity of steering rack vertical wheel speeds of wheel and the displacements of the spring, damper and stabilizer, according to the steering rack displacement and vertical displacement of wheel. The suspension kinematics is divided into three parts, Wheel Position, Wheel Orientation, Spring, Damper and Stabilizer Displacements. Each of these three uses 2-D look-up tables to obtain related kinematics information with two inputs: displacement of steering rack q_{St} and vertical displacement of left and right front wheel z_{w_i}. Wheel position q_i is calculated as the sum of the initial position $q_{i,0}$ and relative change of the position $\Delta q_{i,0}(z_{w_i}, q_{St})$ computed from a 2-D look-up tables with the given two inputs:

$$q_i = q_{i,0} + \Delta q_{i,0}(z_{w_i}, q_{St}) \tag{2.53}$$

Similarly, the wheel orientation in terms of α, β and γ is obtained from 2-D look-up tables with the same inputs, as follows:

$$[\alpha_{Wheel}, \beta_{Wheel}, \gamma_{Wheel}]_i^T = \theta_{Wheel,i}(z_{w_i}, q_{St}) \tag{2.54}$$

The vertical displacement of the spring joint points z_{sp}, damper joint points of front left and front right wheel z_d, and vertical displacement of the stabilizer left joint point relative to the right joint point z_{stab} also rely on steering rack displacement and wheel vertical movement, as expressed in following equations:

$$\begin{aligned}
z_{sp_i} &= z_{sp_i}\left(z_{w_i}, q_{St}\right)\\
z_{d_i} &= z_{d_i}\left(z_{w_i}, q_{St}\right)\\
z_{stab_i} &= z_{stab_i}\left(z_{w_i}, q_{St}\right)
\end{aligned} \tag{2.55}$$

To calculate the wheel velocity relative to vehicle body and establish the equation of motion described in Chapter 2.2.3, some partial derivatives must be evaluated, including changes in wheel position and orientation with respect to vertical wheel movement and steering rack displacement, represented as $\frac{\partial q_i}{\partial z_{w_i}}$, $\frac{\partial q_i}{\partial q_{St}}$, $\frac{\partial \theta_i}{\partial z_{w_i}}$, $\frac{\partial \theta_i}{\partial q_{St}}$. To evaluate the forces acting between the wheel and vehicle body (suspension equivalent force in the direction of wheel center motion), partial derivatives of vertical displacement of spring, damper and stabilizer with respect to vertical wheel movement and steering rack displacement are calculated, represented as $\frac{\partial z_{sp_i}}{\partial z_{w_i}}$, $\frac{\partial z_{d_i}}{\partial z_{w_i}}$, $\frac{\partial z_{stab_i}}{\partial z_{w_i}}$. Suspension compliance kinematics describes additional elastic wheel displacements caused by the forces and torques acting on the wheel. The additional displacements are considered in x and y directions and α_{Wheel} and γ_{Wheel} angles. In particular, Δx_{Wheel}, Δy_{Wheel}, $\Delta\alpha_{sus}$ and $\Delta\gamma_{sus}$ are calculated from 2D look-up tables as functions of the longitudinal force, lateral force, longitudinal torque and self-aligning torque , represented by $\Delta q_{Compl,Fx}$, $\Delta q_{Compl,Fy}$, $\Delta q_{Compl,Trqx}$ and $\Delta q_{Compl,Trqz}$ respectively. The total additional displacements and angles due to compliance are are computed as the sum of the additional movements of the tire caused by four different forces or torques:

$$\Delta q_{Compl,Fx} + \Delta q_{Compl,Fx} + \Delta q_{Compl,Fx} + \Delta q_{Compl,Fx} = \begin{bmatrix} \Delta x_{Wheel}[left; right] \\ \Delta y_{Wheel}[left; right] \\ \Delta\alpha_{Wheel}[left; right] \\ \Delta\gamma_{Wheel}[left; right] \end{bmatrix} \tag{2.56}$$

Forces acting between the wheel and vehicle body, are generated by spring, damper, and stabilizer. These forces are functions of spring, damper and stabilizer displacements which are represented by 2-D look-up tables. The equations and corresponding look-up tables with respect to spring, damper and stabilizer forces are described as follows:

$$\begin{aligned}
F_{sp_i} &= F_{sp_i}\left(z_{sp_i}\right)\\
F_{d_i} &= F_{d_i}\left(z_{d_i}\right)\\
F_{stab_i} &= F_{stab_i}\left(z_{stab_i}\right)
\end{aligned} \tag{2.57}$$

The description of suspension model made for the front axle is similar for the rear axle. However, for rear suspension system, it calculates the wheel position, wheel angular velocity and the displacements of the spring, damper and stabilizer with respect to the vertical wheel displacement of wheel and the vertical wheel displacement of the opposite side wheel, rather than steering rack.

Tire Model Development

The tire model utilizes the Pacejka's Magic Formula (MF) [7], it is a semi-empirical tire-road interaction model which describes longitudinal and lateral tire force characteristics and the self-aligning torque as functions of longitudinal and/or lateral slip, wheel loads and camber. The basic form of the Magic Formula is:

$$Y(x) = Dsin\left[C\,arctan\left\{Bx - E\left(Bx - arctan\,Bx\right)\right\}\right] + S_v \tag{2.58}$$

with $x = X + S_h$, where $Y(x)$ is the possible output F_x,F_y or M_z, X is the input (slip ratio or slip angle), B is the stiffness factor, C is the shape factor, D is the peak value, E is the curvature factor, S_v is the vertical shift, and S_h is the horizontal shift. The result of the model are shown in Figure 2.22. The six coefficients listed above are called macro-parameters of Pacejka and govern the trend of the curve:

- D defines, except for the vertex shift, the maximum value drawn from the function;
- BCD product corresponds to the slope of the curve in the origin;
- C controls the shape of the curve and governs the abscissa of the maximum and the curvature in its surroundings.

The shifts allow to translate the curve and to contemplate the contribution of camber, hysteresis, asymmetry and taper of the tire. It is important to note that for $C \leq 1$ the maximum value of the curve coincides with the asymptote and that for $E > 1$ the curve degenerates. The expression just described allows to represent the characteristics of pure interaction. If these conditions are broken, we will talk about a combined interaction. At the same load, camber and slip (ratio or angle) the combined interaction is more modest than pure since part of the available adherence is engaged by the complementary interaction. This observation led to the development and implementation of the "cosine version" of the Pacejka formula. The first expression elaborated was:

$$G = Dcos\left[C\,arctan\left(Bx\right)\right] + S_h \tag{2.59}$$

With B, C, D and S_h distinct from the previously defined macro parameters. As shown in Figure 2.23, parameter:

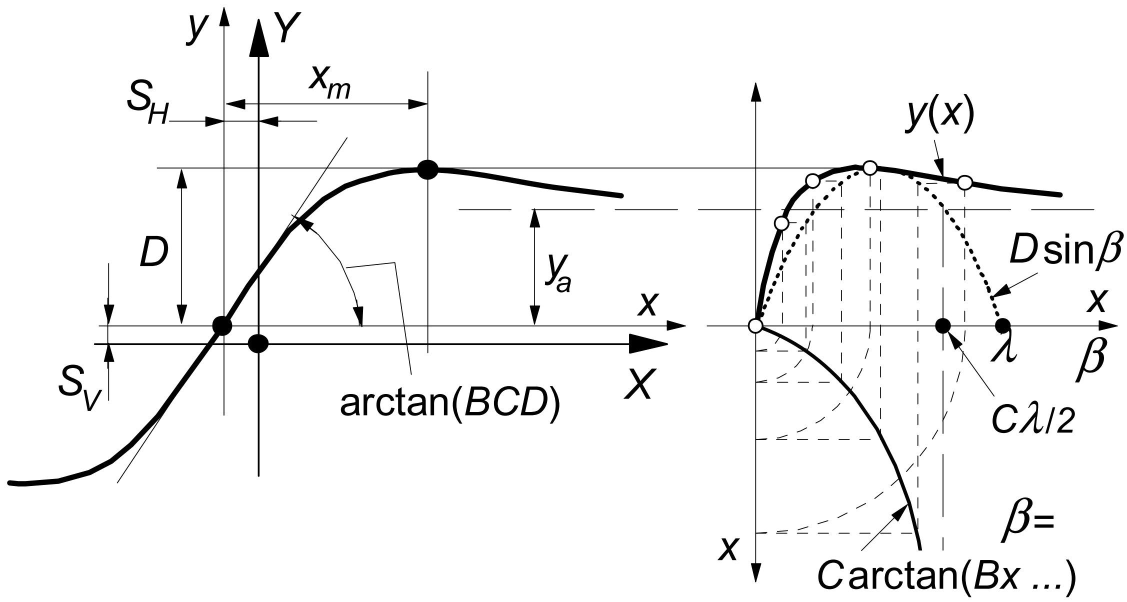

Fig. 2.22 Curve produced by the original sine version of the Magic Formula [7].

- D represents the maximum value (slightly less than 1 in the presence of offset);
- C determines the position of the horizontal asymptote placed at the base of the curve;
- B governs the shape and intercepts with the axis of the abscissas.

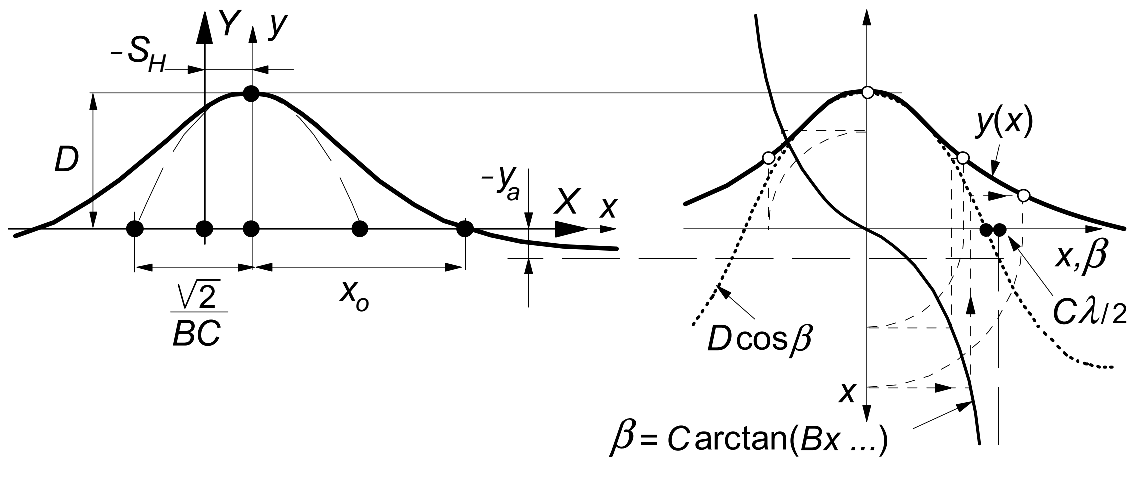

Fig. 2.23 Curve produced by the cosine version of the Magic Formula [7].

In this expression, parameter G, multiplied by pure interaction, returns the combined interaction. This is evidently a weight function, a reduction factor that has a physical sense only if it is within the range $[0, 1]$. The interaction characteristic varies according to the vertical load, the camber angle, the inflation pressure, the spin. It also depends on the construction characteristics, the thermo-mechanical and tribological properties of the tire, as well as on the road surface conditions. Further complications are given by the non-linear behaviour of the system. To introduce dependence on all these factors into the economy of the equation, the macro parameters have been expressed as a combination of micro-parameters:

- parameters for defining the force curves at pure slip condition;
- parameters for defining the torque curves at pure slip condition;
- parameters for defining the force curves at combined slip condition;
- parameters for defining the torque curves at combined slip condition.

Sometimes the interaction characteristics dictated by the MF are significantly far from the experimental points detected by the telemetry. This is due to the impossibility of faithfully reproducing in the laboratory the conditions of humidity, temperature, inflation pressure, adhesion, wear, taper which the tire is subjected once mounted on a real vehicle. To solve this problem, scaling factors have been introduced that allow modulating macro-parameters and modifying the shape of the curve. They are indicated with the letter λ. In this work, the tire model utilizes the formulation 6.1 of MF, described in [9], that allows to contemplate extreme camber conditions and the contribution of tire inflation pressure.

Wheel Speed Model Development

The wheel speed model considers only the rotational degree of freedom of the wheel movement. Therefore, the generalized degrees of freedom of wheels in vehicle reference coordinate system V, are

$$\begin{bmatrix} \dot{q}_{11} \\ \dot{q}_{12} \\ \dot{q}_{13} \\ \dot{q}_{14} \end{bmatrix} = \begin{bmatrix} \omega_1 \\ \omega_2 \\ \omega_3 \\ \omega_4 \end{bmatrix} \tag{2.60}$$

where, ω_1, ω_2, ω_3 and ω_4 are the angular velocities of front left, front right, rear left and rear right wheel, respectively. A 1st order equation describes the wheel dynamics, derived from a torque balance around the wheel axis of rotation:

$$J_{wheel_i}\dot{\omega}_i = Trq_{Wheel_i} + Trq_{Tire_i} - Trq_{Brake_i} \tag{2.61}$$

with $i \in \{1, \ldots, 4\}$, where J_{wheel} is the inertia about the wheel rotational axis, Trq_{Wheel} is the driving torque, transferred through the drivetrain, Trq_{Tire} is the tire torque, and Trq_{Brake} is the braking torque.

Steering Model Development

The steering model computes the movement of the steering rod starting from the steering wheel angle defined by the driver. The steering rod movement is passed on to the suspension kinematics so that the wheel position and orientation can be calculated. The steering model is composed of a steering column, steering transmission, and steering rod, as shown in Figure 2.24. The generalized degree of freedom is the displacement of the steering rod:

$$\begin{bmatrix} \dot{q}_{15} \end{bmatrix} = \begin{bmatrix} \dot{q}_{St} \end{bmatrix} \tag{2.62}$$

Neglecting the coupling between the steering degree of freedom and the other vehicle

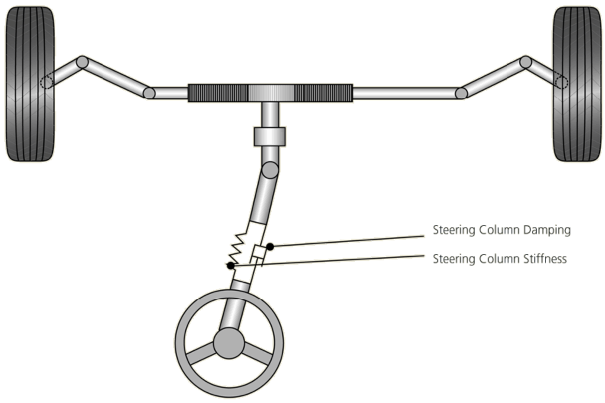

Fig. 2.24 Schematic of steering model [6].

degrees of freedom, the equation of motion for the steering rod movement can be written as follows:

$$M_{St}\ddot{q}_{St} = Q_{L_{St,1}} + Q_{L_{St,2}} + Q_{L_{St,Gear}} + Q_{L_{St,Fric}} \tag{2.63}$$

where, M_{St} is the generalized mass in the direction of q_{St} which depends on the wheel inertias and masses, $Q_{L_{St,1}}$ and $Q_{L_{St,2}}$ are the generalized forces due to front left and right tires forces and torques, respectively, and depend on the suspension kinematics, $Q_{L_{St,Gear}}$ is the generalized force at the steering gear from the steering column, $Q_{L_{St,Fric}}$ is the generalized force due to friction in the steering rod. The friction in the steering gear resists the movement of the steering rod. The friction force is composed of two components. Static force $F_{St_{Fric,Stat}}$ balances the other steering forces. The transition behaviour is computed by a dynamic term, which depends on the speed of the steering rod:

$$Q_{L_{St,Fric}} = F_{St_{Fric,Stat}} - \mu_{St_{Fric}} \dot{q}_{St} \tag{2.64}$$

where, $\mu_{St_{Fric}}$ is the transient friction coefficient.

Brake Model Development

The brake model consists of a simple model that computes an additional torque that reduces the net torque acting on the tire as a function of the brake input signal. A brake torque is calculated at each wheel according to the brake pressure p_{Brake} as:

$$Trq_{Brake_i} = 2\mu_{Brake_i} r_{Brake_i} \left(p_{Brake_i} A_{Brake_i}\right) \tag{2.65}$$

with $i \in \{1,\ldots,4\}$, where μ_{Brake} is the brake friction coefficient, r_{Brake} is the radius of the brake disc, and A_{Brake} is the brake friction area. The brake pressure is calculated from a look-up table as a function of the driver pedal position. The calculated torque is the maximum brake torque, which corresponds to a certain brake pressure. The effective braking torque is modeled as a friction torque with sticking capability. The friction torque consists of two components, the static and the dynamic torque. The static torque, $Trq_{Brake_{Stat}}$, is used to balance the shaft and tire torques acting on the wheel, $Trq_{Brake_{Stat}} = Trq_{Shaft} + Trq_{Tire}$. The dynamic torque is added to allow the transition from the wheel rotation to standstill. The static torque and the sum of static and dynamic torques are limited by the maximum braking torque, which is calculated in the brake model. The effective braking torque Trq_{Brake,eff_i} is calculated as follows:

$$Trq_{Brake,eff_i} = Trq_{Brake_{Stat,i}} + c_{Dyn_{Brake,i}} \omega_i \leq Trq_{Brake_i} \tag{2.66}$$

where, $c_{Dyn_{Brake,i}}$ is a coefficient that describes the change of braking torque with wheel speed.

2.3 Road Vehicle Model Validation

This Chapter presents a process for validating the developed road vehicle model, called ASM. As described in previous Sections, the developed ASM model includes the dynamics that are relevant for studying vehicle handling and braking, but it is still simple enough to run in real-time, while reduces the effort for parameterization. Its validation was conducted against high-order Multibody Simulation (MBS) embedded in ADAMS/Car by MSC. Respect to the developed ASM few bodies vehicle dynamics model, which has only 15 degrees of freedom, the high-order model is much more complicated, with about 10^2 degrees of freedom, and, therefore, a significant experimental activity is required to assess its parameters. In particular, it requires detailed information about suspension design. Furthermore, it is time-consuming and, therefore, not adequate for the real-time simulation of HIL environment. The high-order MBS have a general applicability and can provide excellent results, while, on the other hand, the ASM model may be inaccurate for studies that consider wide-ranging and/or severe inputs, since it is based on many assumptions. Therefore, it is necessary to verify that ASM model reliable simulates the vehicle handling and braking. The validation process has consisted of three main phases: experimental field data collection, vehicle parameter measurement, and comparison of simulation predictions with the high-order model data using the same driver control inputs. The phases concerning the experimental field data collection, and vehicle parameter measurement have been carried out by the industrial partner of the Ph.D. program. In particular, a target vehicle have been selected: a Segment-D SUV passenger car, equipped with a Diesel engine 2.2 L I4 Multijet II 210 CV AT8 Q4, whose main parameters are reported in Tables 2.1, 2.3 and 2.4. In the research work, only the third phase has been carried out, comparing simulation results of the ASM model respect to the high-order multibody model. Specifically, the validation has two main objectives:

- to evaluate uncertainty of the ASM model with respect to the high-order multibody model in reproducing handling and braking behaviour of the vehicle;
- to verify the reliability of the model in reproducing the energy flows within the power-train and the vehicle, in order to obtain an accurate evaluation of fuel consumption, based on the control inputs and the road load.

2.3.1 Vehicle Dynamics Validation

Validation process consists of comparing the vehicle dynamics response to control inputs (steering rod displacement, brake and drive torques) simulated with the ASM model with respect to the results of the high-order MBS obtained considering the same inputs. There are standardized maneuvers that can be performed that cover a broad range of vehicle operations. In order to validate the model, test manoeuvres relevant to vehicle handling and braking were selected. The tests used include the following:

- straight-line braking manoeuvres;
- slow ramp steer manoeuvre;
- step steer manoeuvres;

- braking-in-turn manoeuvre.

Some of these maneuvers are conducted under several different conditions. For purposes of validation, aerodynamic effects were neglected in both high-order model and ASM simulation environments, according to validation methodology proposed in [105]. The results for the vehiicle dynamics rensponse analysis are summarized in Figures 2.25-2.49, where the relevant quantities of lateral and longitudinal dynamics have been carefully post-processed to clearly represent the uncertainty of the ASM simulation in terms of:

- direct comparison between AMS and high-order MBS results, to verify that ASM uncertainty remain within 95% of confidence range;
- relative deviation between AMS and high-order MBS results, calculated as:

$$Relative\ deviation = \left| \frac{\Gamma_{ASM} - \Gamma_{high-order}}{\Gamma_{high-order}} \right| 100\% \tag{2.67}$$

  and the mean value over the simulation samples, where, Γ_{ASM} and $\Gamma_{high-order}$ are results of ASM simulation and high-order MBS, respectively, for a generic quantity.

Vehicle Longitudinal Dynamics: Straight-Line Braking Manoeuvres

To verify the capability of the few bodies ASM simulation to reproduce the vehicle longitudinal dynamics, straight line braking maneuvers are used. Driving the vehicle straight ahead at a speed of 100 km/h, after 2 s a step input in brake pedal is applied to achieve a desired level of deceleration. Two straight-line braking maneuvers have been executed, for two different levels of deceleration of 4.9 m/s^2 and 7.4 m/s^2, called straight-line braking 1 and 2, whose inputs in terms of torques at wheels are shown in Figures 2.25a and 2.25b, respectively. The results for the longitudinal deceleration are used to assess ASM performance for reproducing the vehicle longitudinal dynamics. Figures 2.26a and 2.28a show the comparison between ASM and high-order MBS results for straight-line braking 1 and 2, respectively, while Figures 2.26b and 2.28b report the time history of their relative deviation after 2 s of simulation, calculated as:

$$Relative\ deviation = \left| \frac{a_{x,ASM} - a_{x,high-order}}{a_{x,high-order}} \right| 100\% \tag{2.68}$$

as well as the mean value over the simulation samples, where, $a_{x,ASM}$ and $a_{x,high-order}$ are the longitudinal accelerations of ASM simulation and high-order MBS, respectively. It can be noted that, both ASM and high-order MBS have approximately the same steady state deceleration level, assessed after 6 s. In particular, considering the straight-line braking

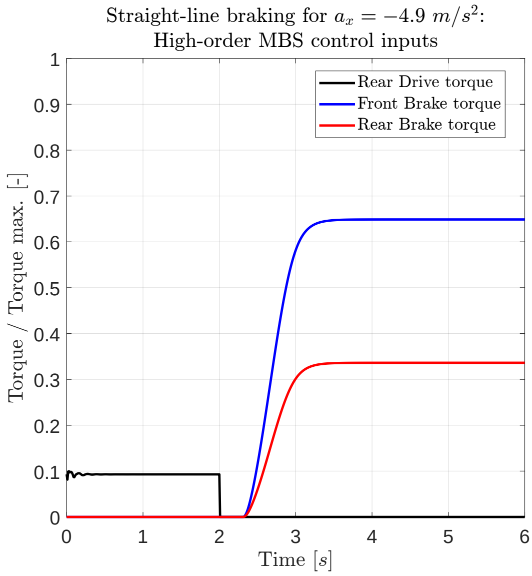

(a) Wheel torques input for straight-line braking 1 $\left(a_x = -4.9\, m/s^2\right)$.

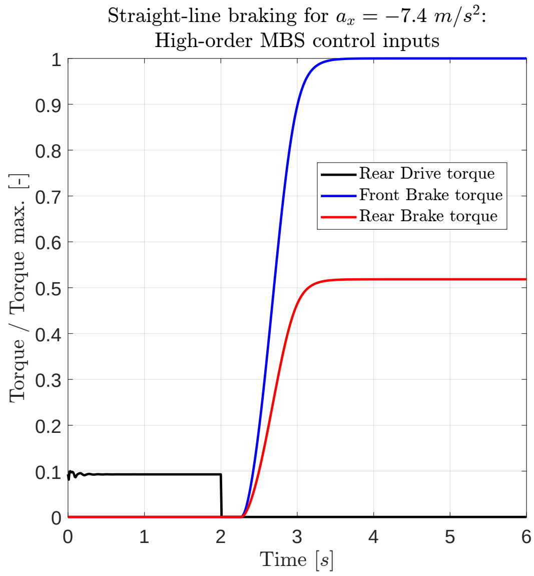

(b) Wheel torques input for straight-line braking 2 $\left(a_x = -7.4\, m/s^2\right)$.

Fig. 2.25 high-order MBS control inputs for straight line braking maneuvers.

1, ASM have a relative deviation of 0.1% with respect of $-4.9\ m/s^2$ computed by high-order simulation. Similarly, for straight-line braking 2, a deviation of 0.2% from $-7.4\ m/s^2$ have been assessed with ASM. The longitudinal dynamics of the vehicle is, therefore, well predicted by ASM simulation, as highlighted by Figures 2.27 and 2.29, which show the comparison for vehicle speeds computed in straight-line braking 1 and 2, respectively. Generally, there are not significant differences, how confirmed by the Root Mean Square Errors (RMSE) reported in Table 2.5. This is an important fact that should be checked since

Table 2.5 RMSE for straight-line braking manoeuvres.

Manoeuvre	**Quantity**	**RMSE**
Straight-line braking 1	a_x	0.06 m/s^2
Straight-line braking 1	$v_{x,Vehicle}$	0.02 km/h
Straight-line braking 2	a_x	0.06 m/s^2
Straight-line braking 2	$v_{x,Vehicle}$	0.07 km/h

braking is indispensable for vehicle safety.

Vehicle Lateral Dynamics: Slow Ramp Steer Manoeuvre

The slow ramp steering test is used to evaluate the simulation's ability to predict the steady-state lateral acceleration of the vehicle from the linear operation region of the tires to end in the saturation region of the same. As the name implies, vehicle speed is held constant while

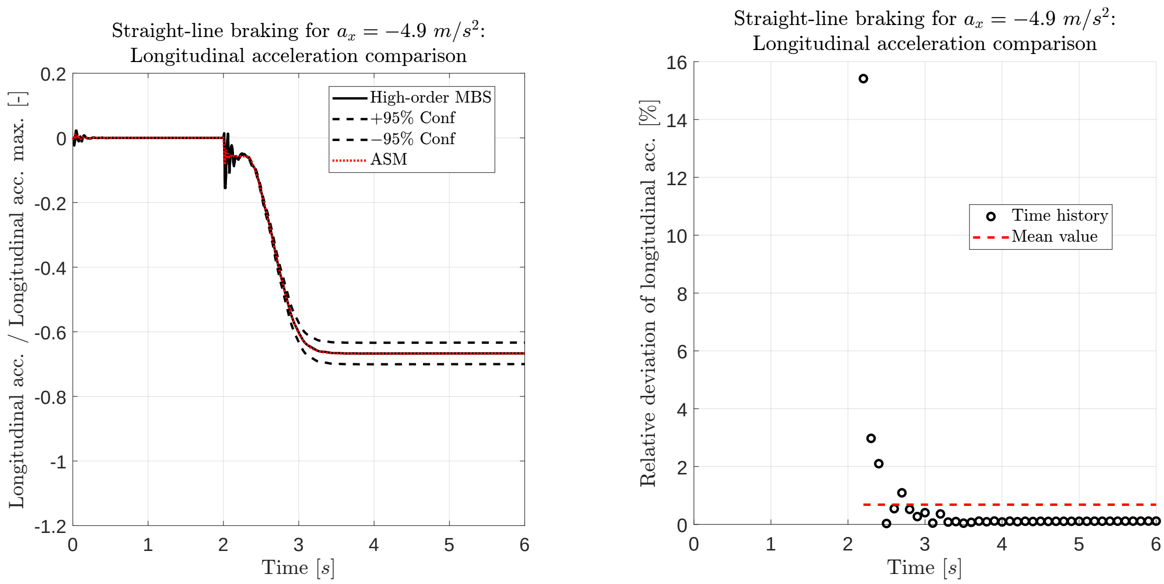

(a) Comparison of longitudinal acceleration. (b) Longitudinal acceleration deviation.

Fig. 2.26 Comparison of ASM and high-order MBS longitudinal acceleration for straight-line braking 1 $\left(a_x = -4.9\ m/s^2\right)$.

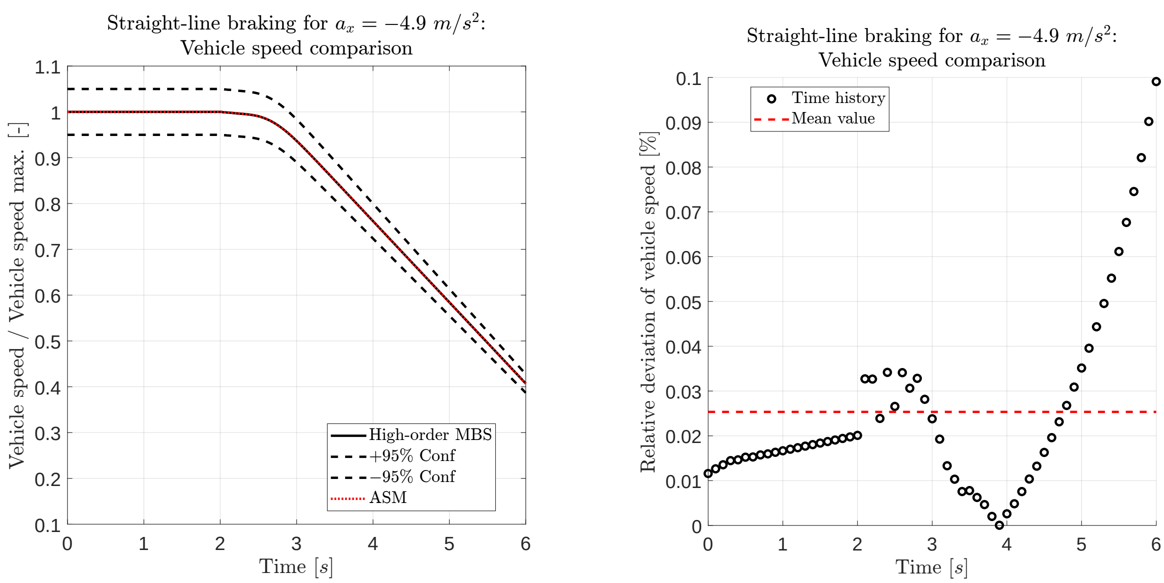

(a) Comparison of longitudinal speed. (b) Longitudinal speed deviation.

Fig. 2.27 Comparison of ASM and high-order MBS longitudinal speed for straight-line braking 1 $\left(a_x = -4.9\ m/s^2\right)$.

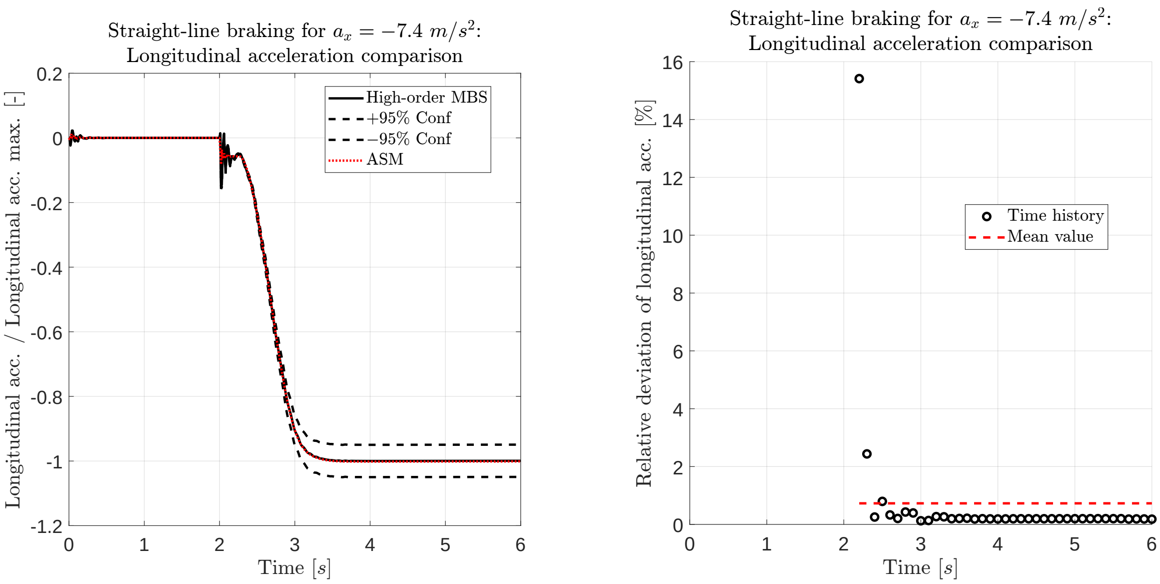

(a) Comparison of longitudinal acceleration. (b) Longitudinal acceleration deviation.

Fig. 2.28 Comparison of ASM and high-order MBS longitudinal acceleration for straight-line braking 2 $\left(a_x = -7.4\,m/s^2\right)$.

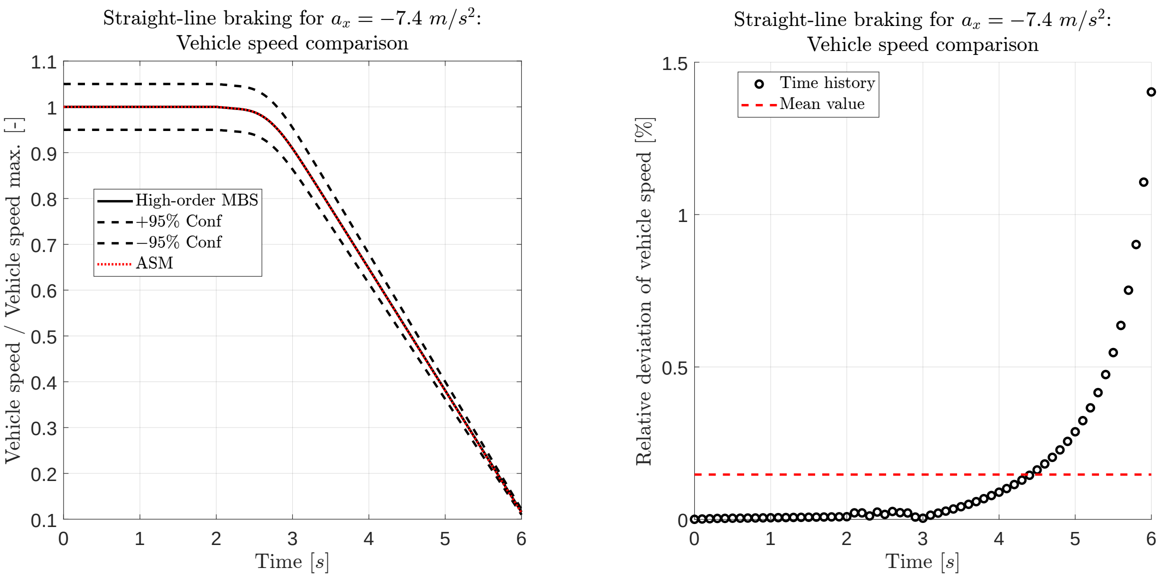

(a) Comparison of longitudinal speed. (b) Longitudinal speed deviation.

Fig. 2.29 Comparison of ASM and high-order MBS longitudinal speed for straight-line braking 2 $\left(a_x = -7.4\,m/s^2\right)$.

the steering wheel angle is slowly increased, as shown in Figure 2.30. Figure 2.31 shows comparison of lateral acceleration as a function of steering angle for vehicle speed of 100 km/h. For moderate acceleration levels, the results confirm the frequency response, which shows good correlation between the two simulations. For high accelerations, instead, it can be noted that the a_y achieved by the high-order MBS is slightly greater than that achieved by the ASM model. The main cause of these behaviors are certainly the tire and suspension parameterizations. Figures 2.32 and 2.32 show the lateral force normalized to the vertical load as a function of slip angle normalized to the maximum value, for front and rear tires, respectively. The tire slip angles, other than speed, depends by the steering angle and lateral acceleration. In particular, the trends reported in the Figures depend mainly by wheels set-up, such as camber. Indeed, during the steering phase, the presence of a negative camber causes the inner tires to deform less and thus move away from the slipping condition, while the outer ones deform more. In this case, camber is different because is modeled through simple map. This causes the slip angles to diverge. However, these forces depend not only on the slip angle but also on the vertical load. Due to the centrifugal force, the vertical load does not remain constant during the maneuver but there is a load transfer from the wheel inside the curve to the external one. The effects of slip angle variations and vertical load influence the trend of tire-road interaction forces: the inner tires generate smaller forces because they see a lower load F_z, while the outer ones generate greater forces due to the F_z increasing. In addition to the load transfer, the left and right slip angles are different. However, having a larger slip angle on the outside wheels is not a problem as there is also a higher vertical load. The differences between these parameters in ASM and high-order MBS determine this forces trend, expressed in terms of RMSE in Table 2.6. In general, the model predictions are comparable to the high-order model data up to the limit of adhesion, with a relative deviation with respect to the maximum lateral acceleration of 4.5 % (computed with eq. 2.67).

Table 2.6 RMSE for slow ramp steer manoeuvre.

Quantity	RMSE
Lateral acceleration a_y	0.3 m/s^2
Front left tire F_y	313 N
Front right tire F_y	111 N
Rear left tire F_y	413 N
Rear right tire F_y	90 N

Vehicle Lateral Dynamics: Step Steer Manoeuvres

The step steer test is used to evaluate vehicle transient and steady-state behaviours up to the limit of adhesion. Specifically, vehicle speed is held constant at 100 km/h and then a step

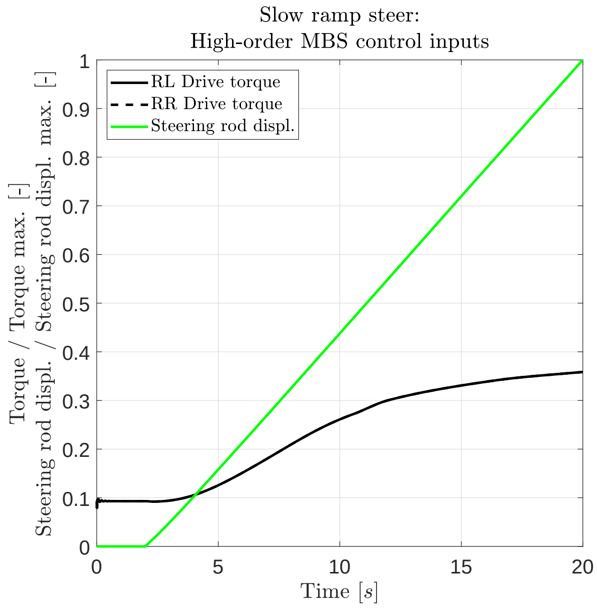

Fig. 2.30 high-order MBS control inputs for slow ramp steering manoeuvre.

input is given at the steering wheel in order to achieve a desired level of lateral acceleration. Two step steer manoeuvres have been executed, for 4.9 m/s^2 and 6.9 m/s^2 of maximum lateral acceleration, called step steer 1 and 2, whose control inputs are shown in Figure 2.34. Results of the first step steer test are reported in Figures 2.35, 2.36, 2.37 and 2.38. While, Figures 2.39, 2.40, 2.41 and 2.42 show the lateral and roll responses for the step steer 2 $\left(a_y = -6.9\ m/s^2\right)$. It can be noted that ASM simulation predicts the vehicle lateral response with a reasonable deviation respect to the high-order model, especially for the low steer angle. Indeed, for high steer angle the mean value of the relative deviation of lateral acceleration rise from 1% to 3.8% Concerning the roll response, again, the average value of relative deviation is about 5%, highlighting how the simulations do a reasonable job of predicting the vehicle dynamics, comparable with high-order MBS. Table 2.7 report the RMSE for the two step steer manoeuvres, to quantify performance of lateral and roll responses.

Table 2.7 RMSE for step steer manoeuvres.

Manoeuvre	Quantity	RMSE
Step steer 1	Lateral acceleration a_y	0.07 m/s^2
Step steer 1	Sideslip angle	0.03 deg
Step steer 1	Yaw rate	0.13 deg/s
Step steer 1	Roll angle	0.08 deg
Step steer 2	Lateral acceleration a_y	0.2 m/s^2
Step steer 2	Sideslip angle	0.04 deg
Step steer 2	Yaw rate	0.37 deg/s
Step steer 2	Roll angle	0.15 deg

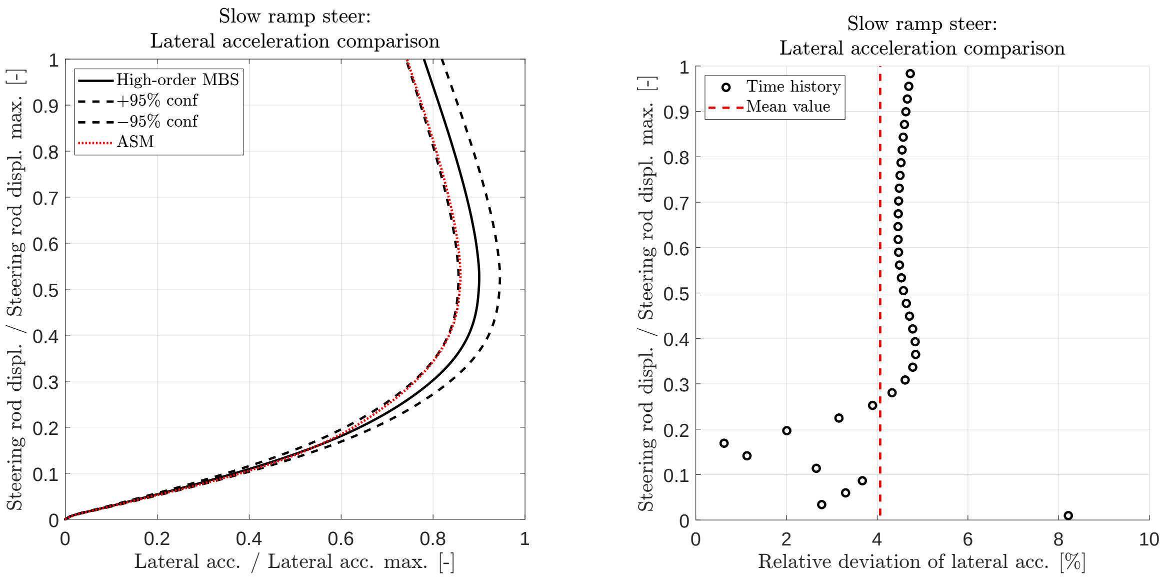

(a) Comparison of lateral acceleration. (b) Lateral acceleration deviation.

Fig. 2.31 Comparison of lateral acceleration as a function of steering angle for 100 km/h.

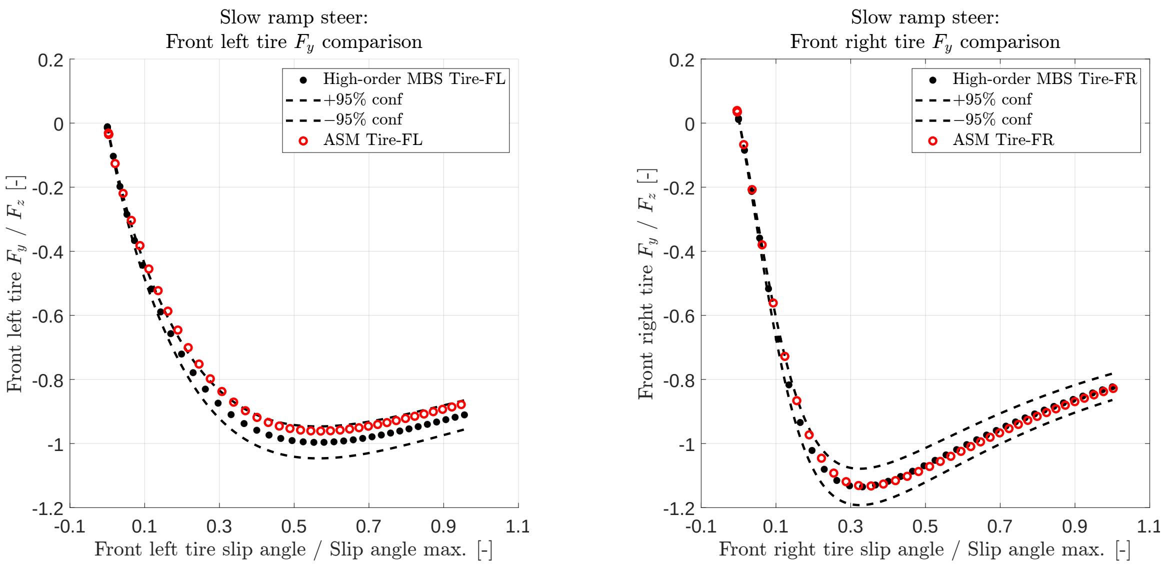

(a) Front left tire. (b) Front right tire.

Fig. 2.32 Normalized front tires lateral force as a function of slip angle.

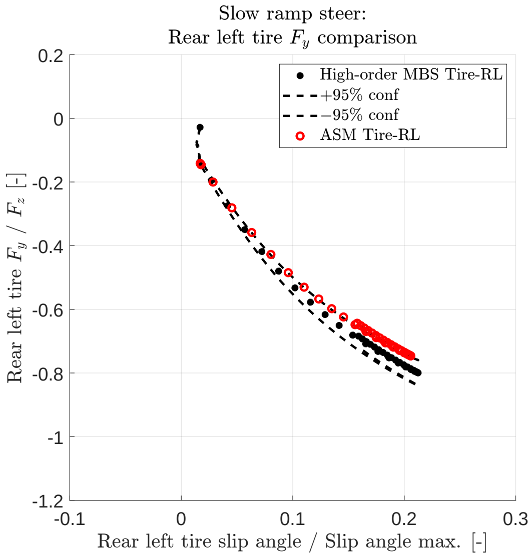

(a) Rear left tire.

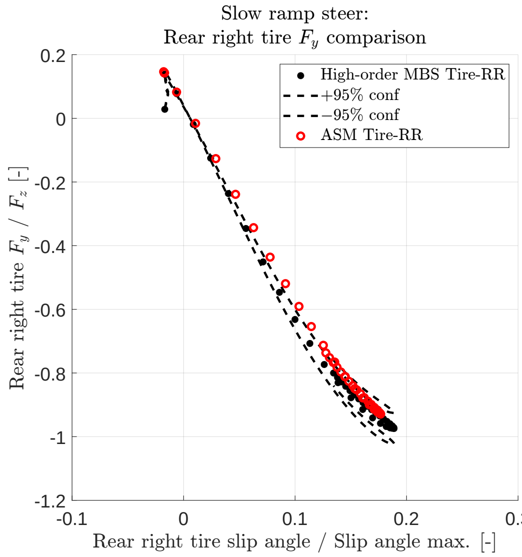

(b) Rear right tire.

Fig. 2.33 Normalized front tires lateral force as a function of slip angle.

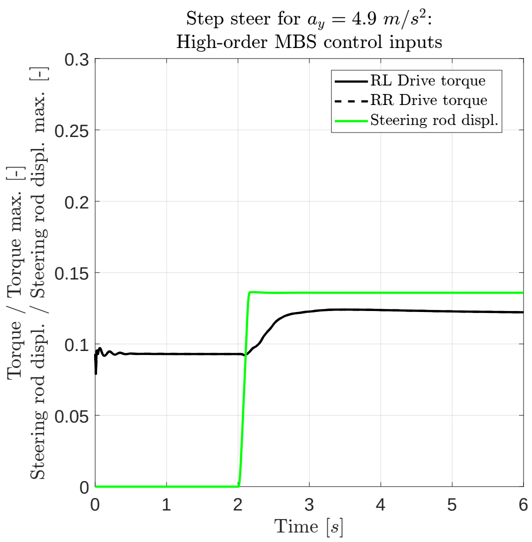

(a) Inputs for step steer 1 $\left(a_y = -4.9\ m/s^2\right)$.

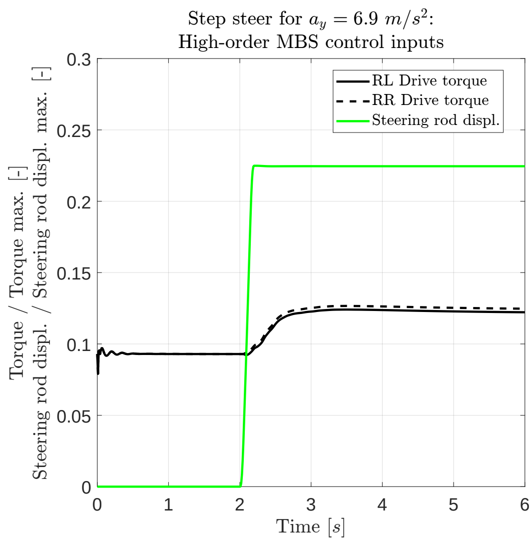

(b) Inputs for step steer 2 $\left(a_y = -6.9\ m/s^2\right)$.

Fig. 2.34 high-order MBS control inputs for step steer maneuvers.

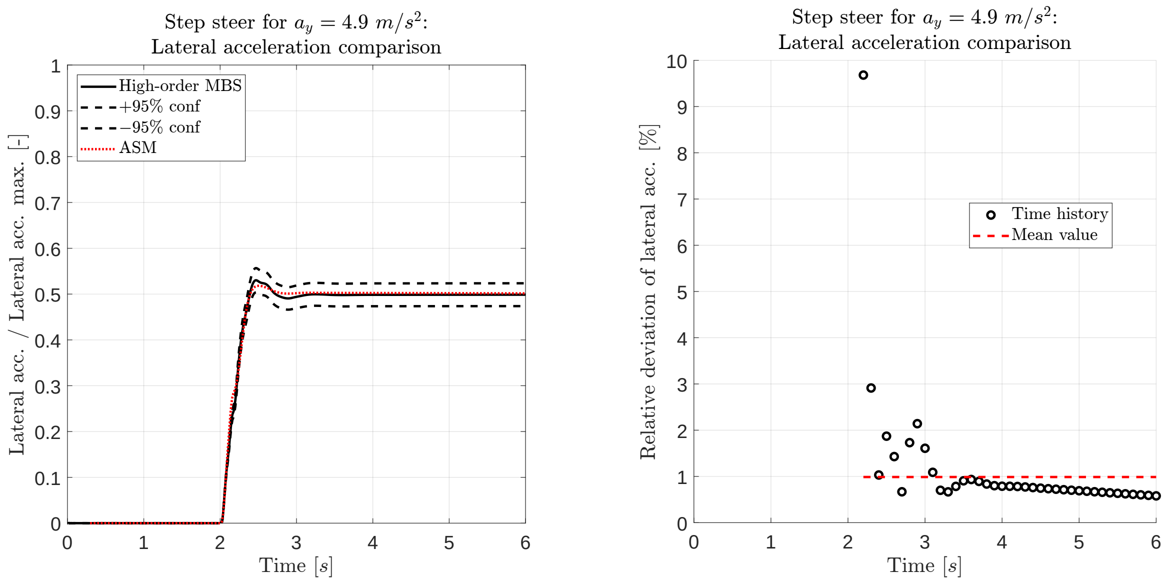

(a) Comparison of lateral acceleration. (b) Lateral acceleration deviation.

Fig. 2.35 Comparison of ASM and high-order MBS lateral acceleration for step steer manoeuvre at step steer 1 $\left(a_y = -4.9\ m/s^2\right)$.

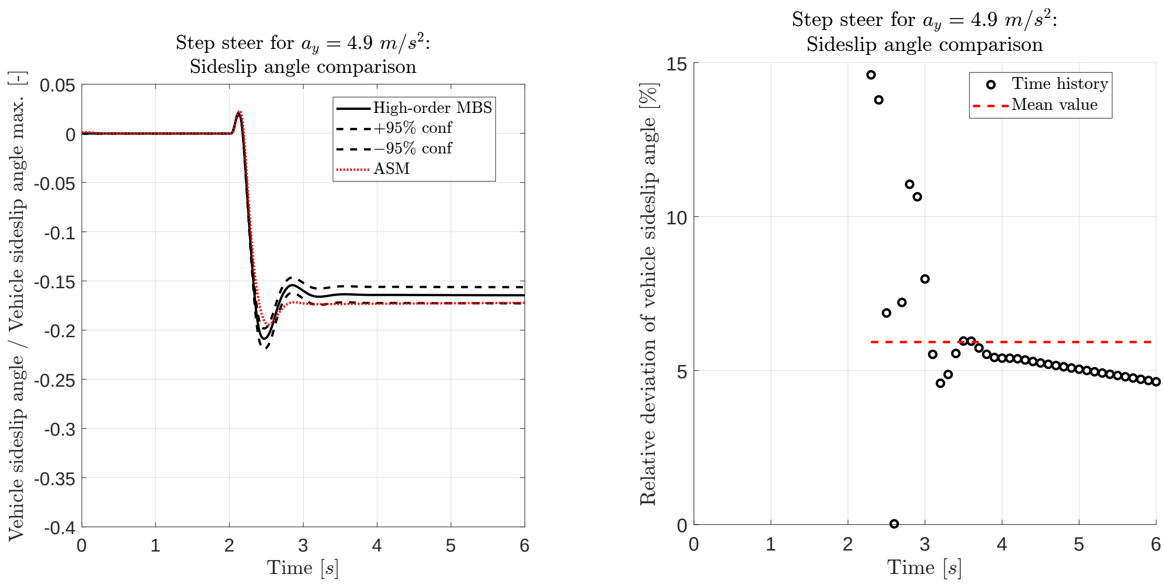

(a) Comparison of Sideslip angle. (b) Sideslip angle deviation.

Fig. 2.36 Comparison of ASM and high-order MBS sideslip angle for step steer manoeuvre at step steer 1 $\left(a_y = -4.9\ m/s^2\right)$.

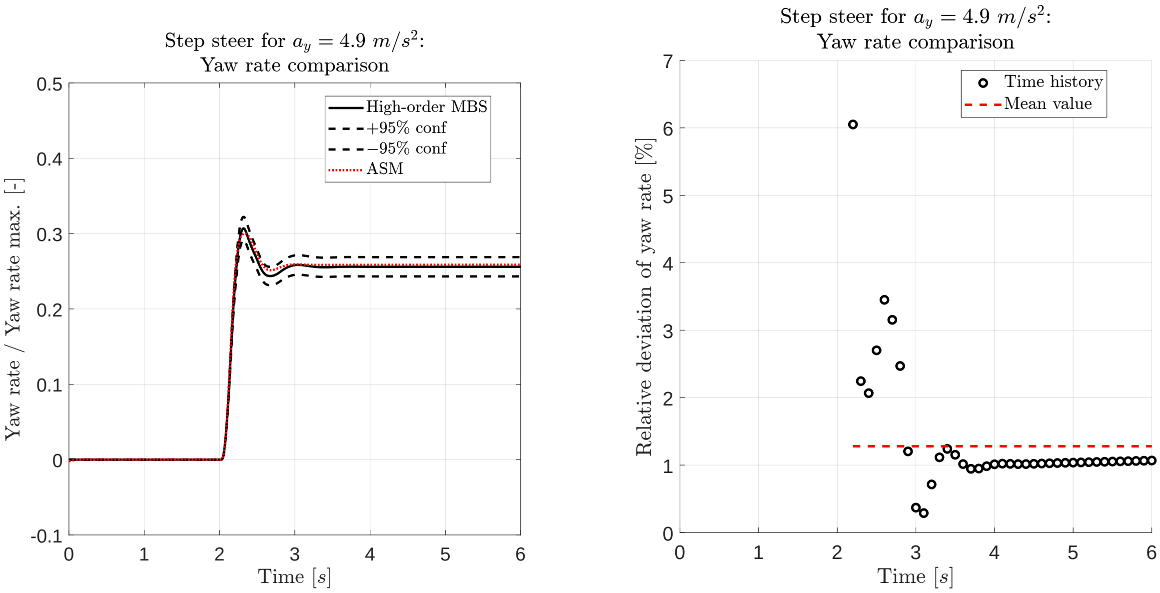

(a) Comparison of yaw rate. (b) Yaw rate deviation.

Fig. 2.37 Comparison of ASM and high-order MBS yaw rate for step steer manoeuvre at step steer 1 $\left(a_y = -4.9\, m/s^2\right)$.

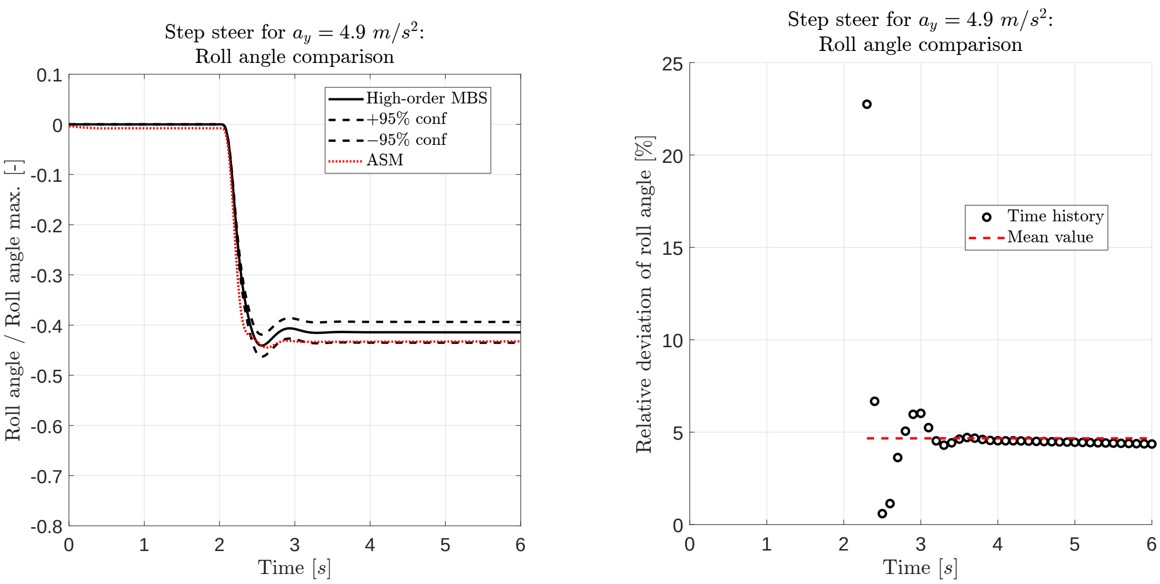

(a) Comparison of roll angle. (b) Roll angle deviation.

Fig. 2.38 Comparison of ASM and high-order MBS roll angle for step steer manoeuvre at step steer 1 $\left(a_y = -4.9\, m/s^2\right)$.

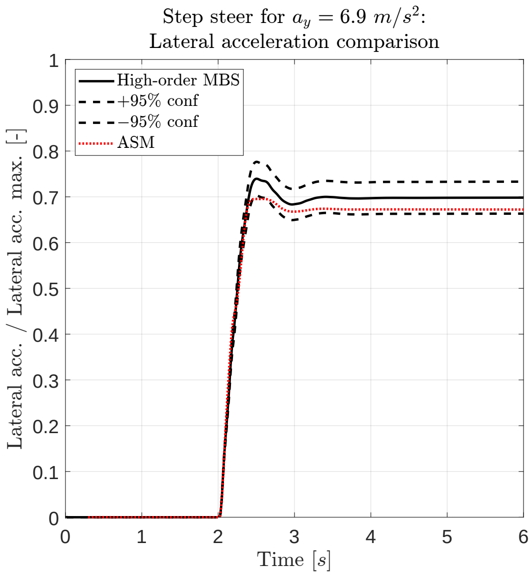

(a) Comparison of lateral acceleration.

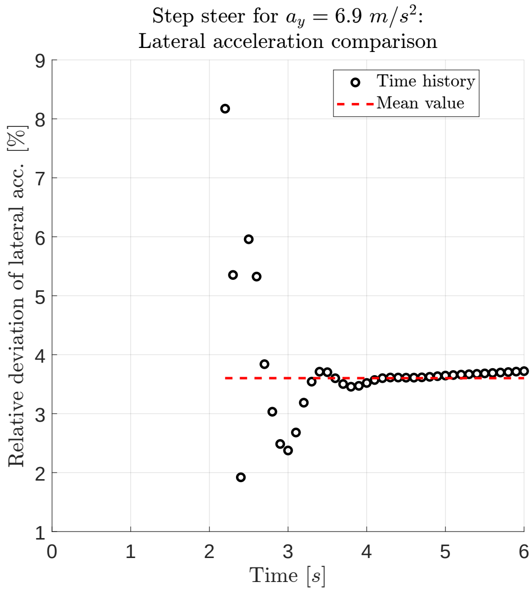

(b) Lateral acceleration deviation.

Fig. 2.39 Comparison of ASM and high-order MBS lateral acceleration for step steer manoeuvre at step steer 2 $\left(a_y = -6.9\, m/s^2\right)$.

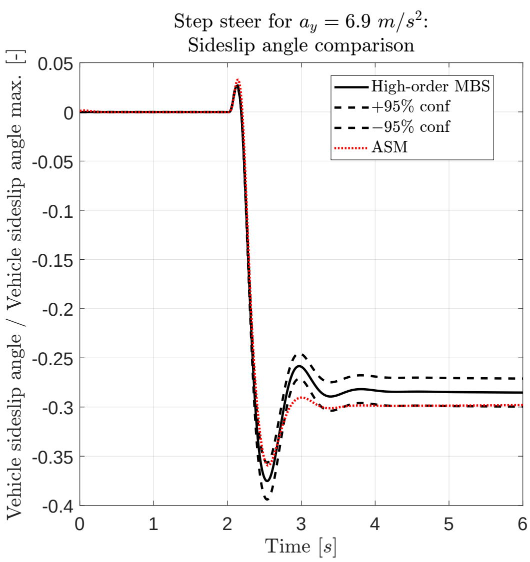

(a) Comparison of Sideslip angle.

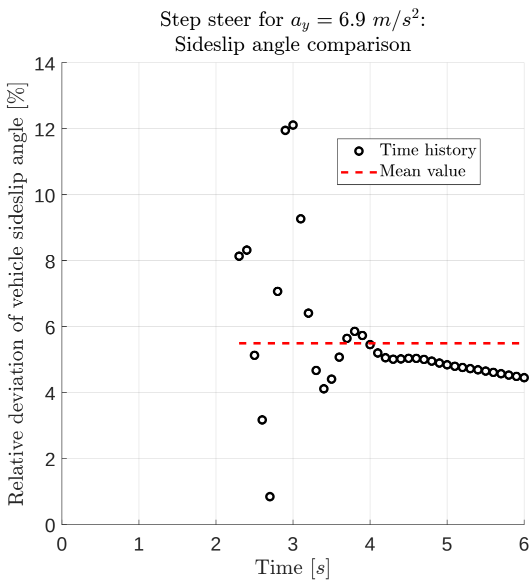

(b) Sideslip angle deviation.

Fig. 2.40 Comparison of ASM and high-order MBS sideslip angle for step steer manoeuvre at step steer 2 $\left(a_y = -6.9\, m/s^2\right)$.

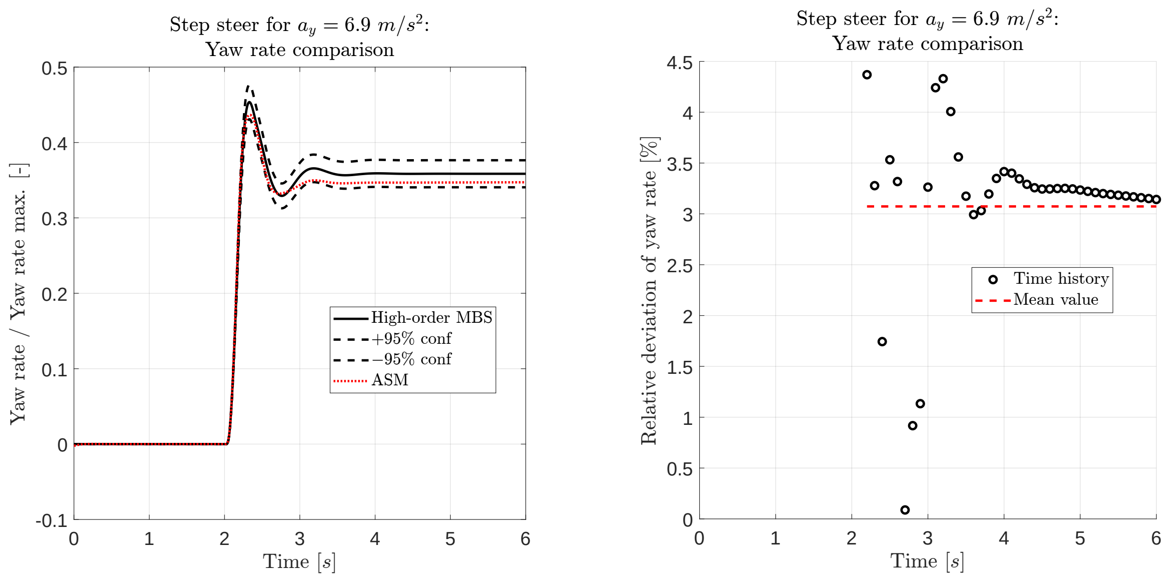

(a) Comparison of yaw rate.

(b) Yaw rate deviation.

Fig. 2.41 Comparison of ASM and high-order MBS yaw rate for step steer manoeuvre at step steer 2 $\left(a_y = -6.9\ m/s^2\right)$.

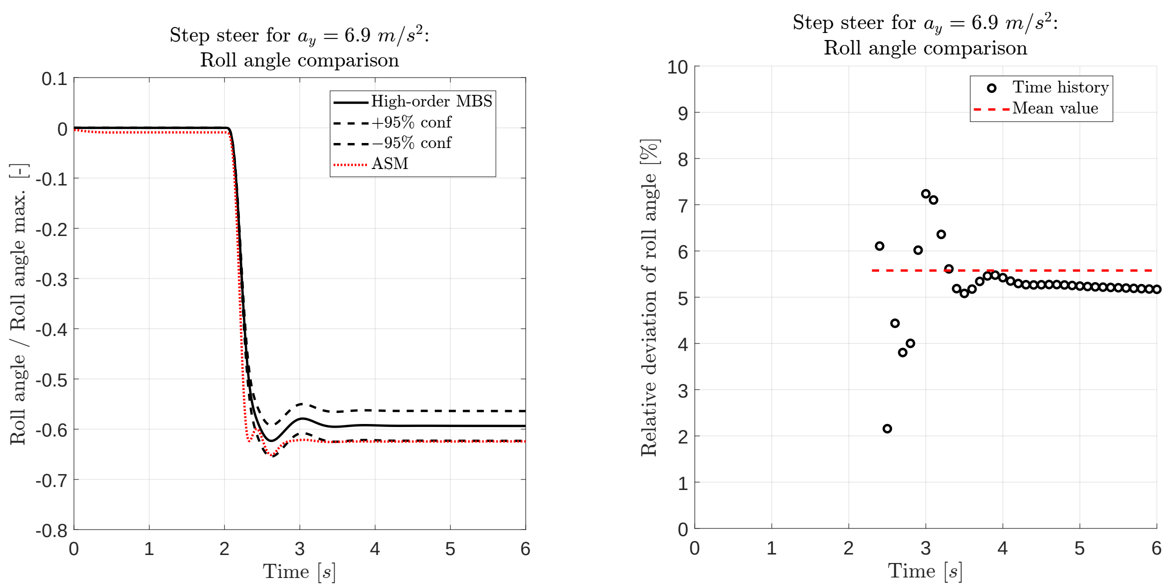

(a) Comparison of roll angle.

(b) Roll angle deviation.

Fig. 2.42 Comparison of ASM and high-order MBS roll angle for step steer manoeuvre at step steer 2 $\left(a_y = -6.9\ m/s^2\right)$.

Vehicle Lateral Dynamics: Braking-in-Turn Manoeuvre

The braking-in-turn test is an attempt to recreate in a test environment a real world crash-avoidance maneuver. Vehicle speed is held constant at 80 km/h and then a step input is given at the steering wheel to achieve a lateral acceleration of 4.9 m/s^2. So, a braking for a deceleration of 4.9 m/s^2 is executed to determine its effect on course holding and directional behaviour of the vehicle. Manoeuvre inputs are shown in Figure 2.43. Figures 2.44, 2.45, 2.46 and 2.47 show the lateral response. Instead, Figures 2.48 and 2.49 report the result in terms of longitudinal response of the vehicle. As can be seen from these Figures, the prediction of sideslip angle with ASM simulation during transient of step inputs, which occur at 2 s and 6 s, do not follow exactly the high-order model data, mainly due to the uncertainty in the evaluation of the camber angles through the map based approach. However, it is very close to high-order MBS results, with a relative deviation lower than 5% during the steady-state. Generally, the ASM model do a very good job of predicting vehicle responses, since the simulation follow the high-order model data very closely. Table 2.8 reports the RMSE of the relevant quantities for braking-in-turn manoeuvre.

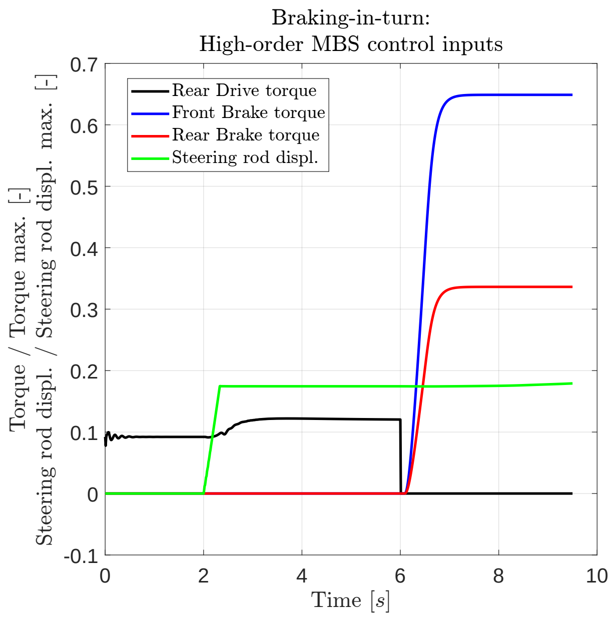

Fig. 2.43 high-order MBS braking-in-turn steer manoeuvre input.

2.3.2 Validation of Energy Flow Simulation

Energy losses in powertrain components are modeled using efficiency maps that contain poertrain's elements efficiency data as a function of the stationary operating conditions This

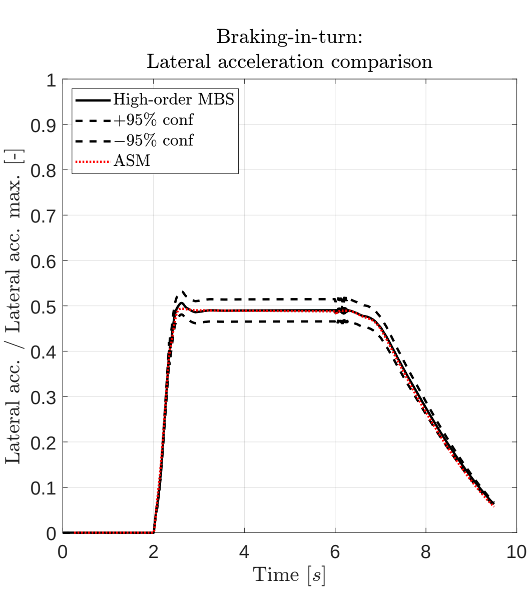

(a) Comparison of lateral acceleration.

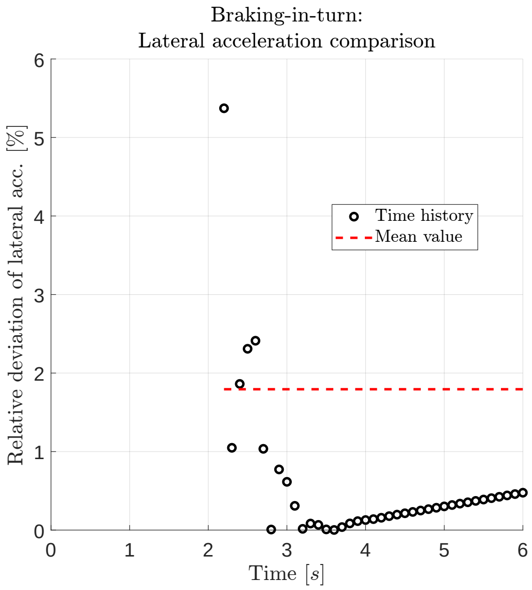

(b) Lateral acceleration error.

Fig. 2.44 Comparison of ASM and high-order MBS lateral acceleration for braking-in-turn manoeuvre.

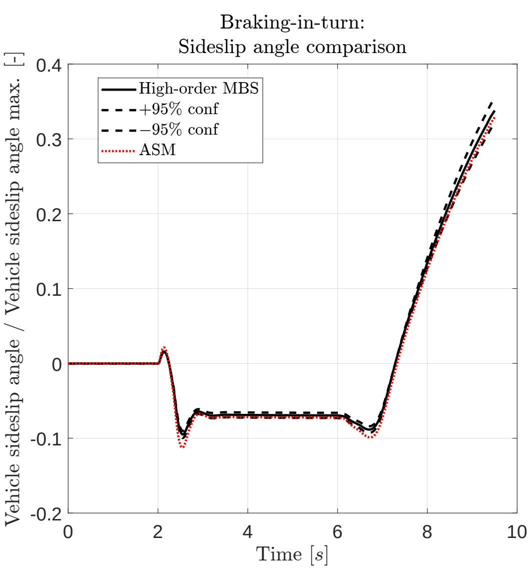

(a) Comparison of Sideslip angle.

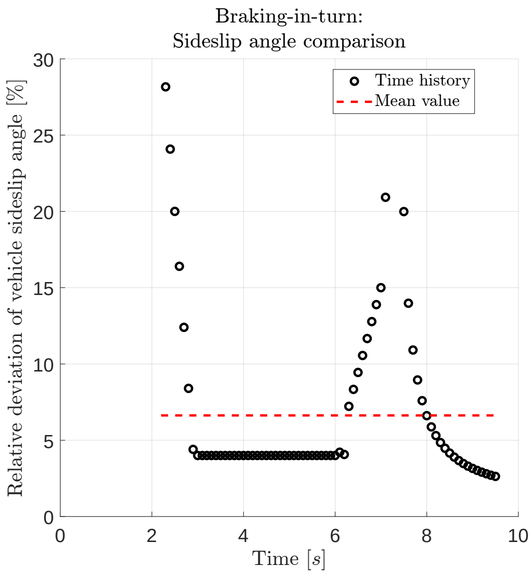

(b) Sideslip angle error.

Fig. 2.45 Comparison of ASM and high-order MBS Sideslip angle for braking-in-turn manoeuvre.

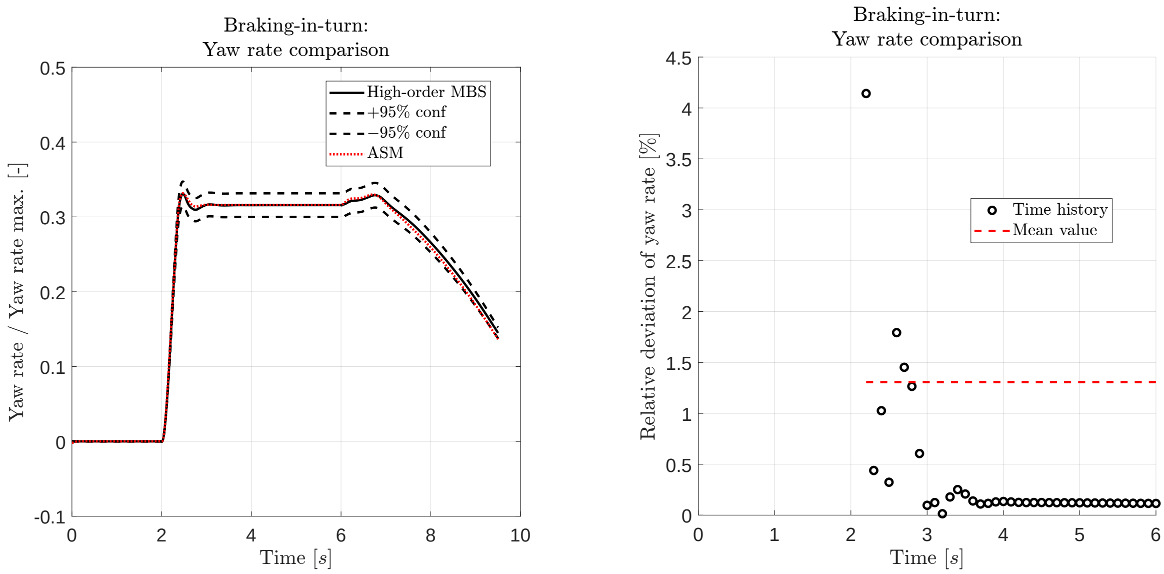

(a) Comparison of yaw rate. (b) Yaw rate error.

Fig. 2.46 Comparison of ASM and high-order MBS yaw rate for braking-in-turn manoeuvre.

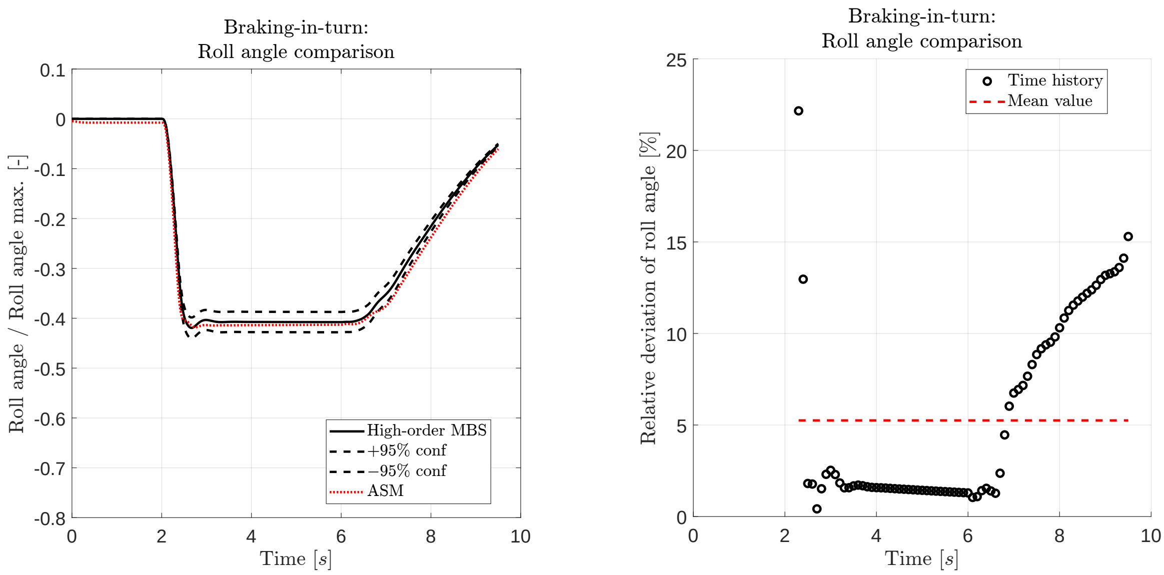

(a) Comparison of roll angle. (b) Roll angle deviation.

Fig. 2.47 Comparison of ASM and high-order MBS roll angle for braking-in-turn manoeuvre.

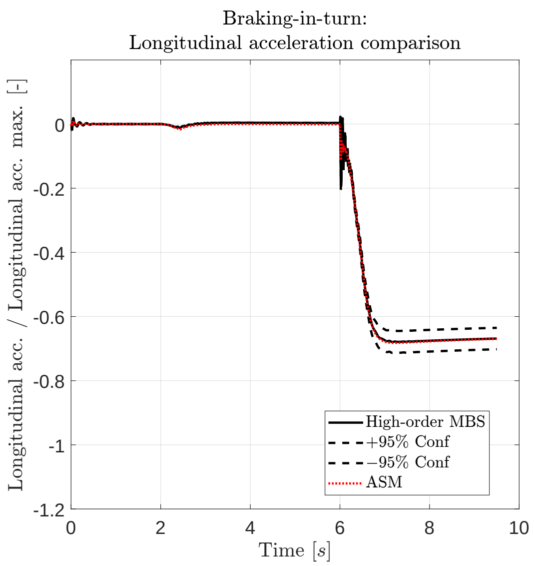

(a) Comparison of longitudinal acceleration.

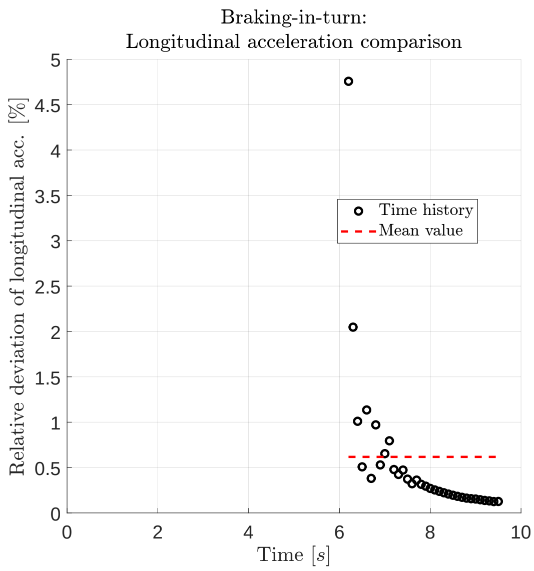

(b) Longitudinal acceleration deviation.

Fig. 2.48 Comparison of ASM and high-order MBS longitudinal acceleration for braking-in-turn manoeuvre.

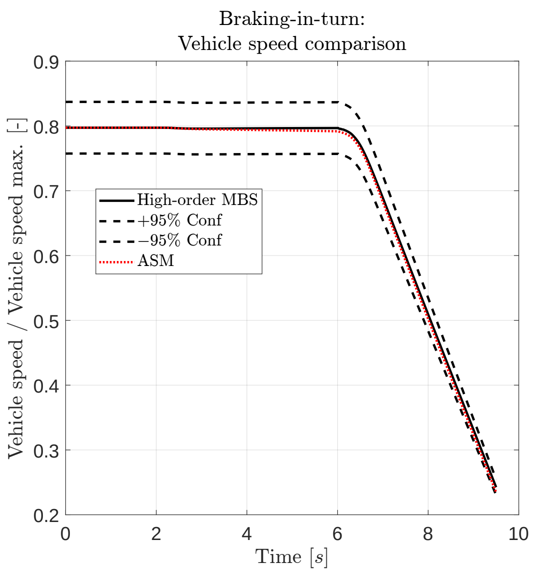

(a) Comparison of longitudinal speed.

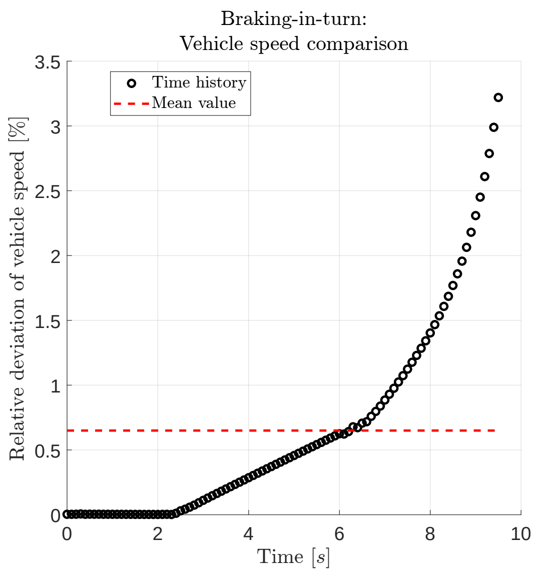

(b) Longitudinal speed deviation.

Fig. 2.49 Comparison of ASM and high-order MBS longitudinal speed for braking-in-turn manoeuvre.

Table 2.8 RMSE for braking-in-turn manoeuvre.

Quantity	**RMSE**
Lateral acceleration a_y	0.05 m/s^2
Sideslip angle	0.08 deg
Yaw rate	0.15 deg/s
Roll angle	0.09 deg
Roll rate	0.23 deg/s
Longitudinal acceleration a_x	0.06 m/s^2
$v_{x,Vehicle}$	0.45 km/h

modelling approach may not be accurate during transients. Furthermore, the methodology used to reconstruct the engine efficiency map, though some assumptions and approximations, reduces the experimental data of the engine under examination to the maximum efficiency only. Therefore, should be validated to verify that the accuracy of the simulation can reliable estimates fuel consumption. Two tests were considered, WLTP and NEDC, both driving cycle designed to assess the emission levels of car engines and fuel economy in passenger cars. Figure 2.50 and Figure 2.51 show simulation results. In the first, an average consumption of 7.4 $dm^3/100km$ was obtained, while in the second it was equal to 6.6 $dm^3/100km$. It is possible to note a deviation respect to reference ranges published by vehicle manufacturer [106], corresponding to 5.9-7 $dm^3/100km$ and to 5-6.1 $dm^3/100km$ for WLTP and NEDC respectively. However, the deviation is less than 10%, therefore considered acceptable.

2.4 Conclusions

The simulation platform presented can be used for testing vehicle dynamics state estimation schemes. It involves full vehicle, road, maneuver and driver models. The few bodies vehicle dynamics model, despite the low degrees-of-freedom that have been included, well predicts the handling and braking behaviours of the simulated vehicle in response to control inputs. Indeed, in most cases it matches with the high-order model, which supports the simplifications of the 15DOF vehicle model. The most significant differences between the two models were found in the brake-in-turn test, where a combination of steering and braking is considered, and slow ramp steer test. The first allows to investigate the ASM model response to severe inputs, while the second to examine it under wide-ranging steer input. These differences are mainly due to map based approach used to model the steer and suspension systems, whose approximations undermine the quality of the simulation. Finally, the model has an acceptable agreement with the high-order MBS, for both handling and braking responses. So, it can be used for the development and testing of estimation schemes discloses in next Chapters. Note that the interest in high-fidelity real-time environment platforms is getting higher and higher

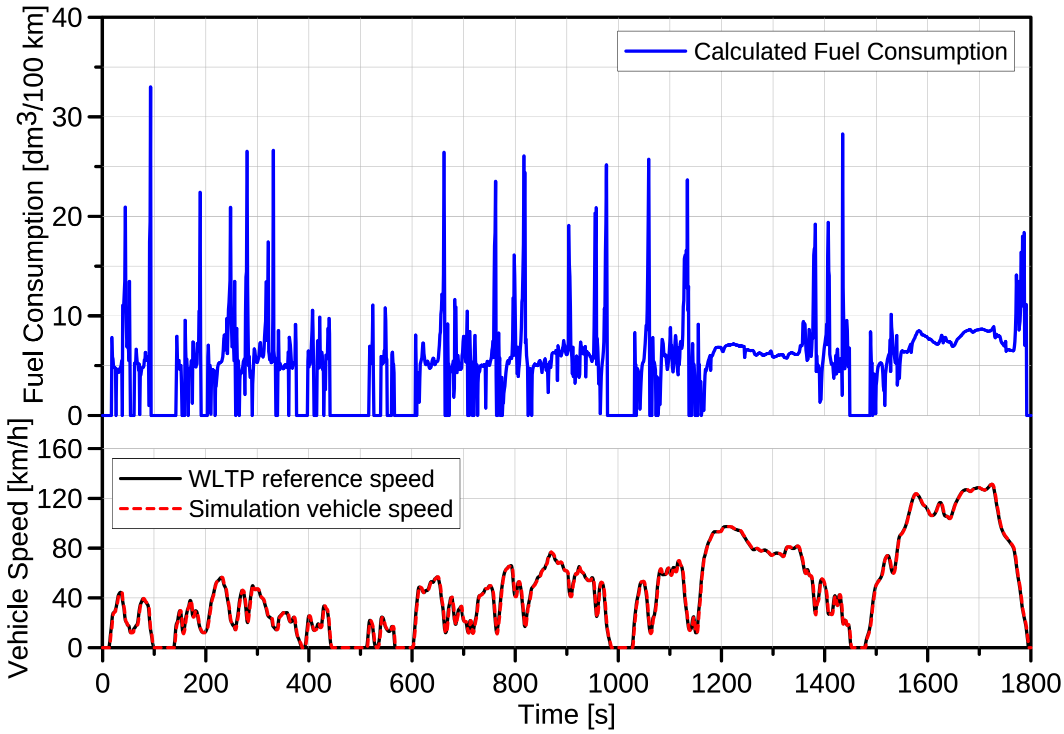

Fig. 2.50 Fuel consumption and vehicle speed for WLTP driving cycle.

in automotive. Of course, ”modeling” plays a central role in the development of embedded control systems. where some simplifications are crucial to perform the control design phase (e.g., neglecting disturbances or nonlinear dynamics hard to handle, ignoring delays and latencies in communication buses, etc.). Such simplifications clearly introduce mismatches between the model and the real plant and it follows that is critical to validate any system via high-fidelity simulation platforms reproducing realistic driving conditions, allowing not only to reduce the number of test drives but also to reproduce any scenario, especially including emerging dangerous situations which are impossible to be safely assessed in the real world [107]. To this aim, the realistic and high-fidelity simulation platform here described is exploited to emulate the ego-vehicle and the nearby environment, so as to deeply evaluate the efficiency of the proposed estimating strategies in different driving conditions.

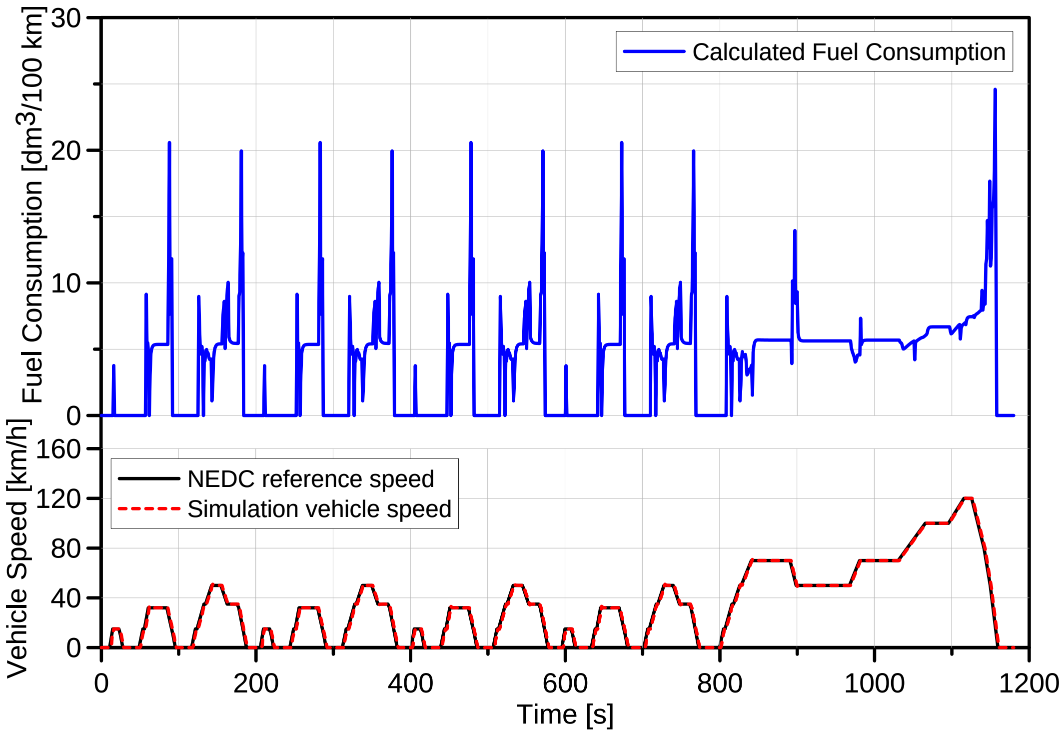

Fig. 2.51 Fuel consumption and vehicle speed for NEDC driving cycle.

Chapter 4

Tire Inflation Pressure Estimation

4.1 Introduction

Proper inflated tires reduce fuel consumption, improve braking performance, improve handling, and extend tires life, while deflated tires create overheating and can lead to accidents. The main causes of tire deflation are leakage, temperature changes, and road potholes [122]. To keep tires inflated a monitoring system is required. An interesting solution are the indirect tire pressure monitoring systems, which outperform the direct measurement systems for cost, life and maintenance. However, estimation obtained through the wheel speed signal frequency analysis may be undermined by high road surface unevenness levels, that make the spectrum of speed signal unclear. Recently, estimation schemes, based on a quarter car model, have been proven to be a successfully approach to estimate the tire inflation pressure [42]. This approach, can be used to estimate tire inflation pressure on any road, but need the knowledge of road surface roughness, which acts as an unknown input for the quarter car model. To address this issue an innovative estimation algorithm is proposed. Specifically, the proposed estimation methodology is based on a interactive multiple model approach which give a reliable estimation of the inflation pressure also when the vertical dynamics of the vehicle change abruptly due to a change of road surface roughness. This algorithm is composed of a bank of four UKFs, each of them tailored to predict vertical dynamics behaviour when the vehicle is on a specific road characterized by a well-defined degree of roughness. Each filter gives a proper estimation of the vehicle state and covariance. All these estimations are combined through a weighted average obtained from a probabilistic model. Therefore, the IMM obtains the tire pressure estimation without an a-priori knowledge of the road surface. Compared to the dPTMS, the proposed system has the advantage of having the accelerometers on the vehicle. This is the reason why they do not need to be replaced

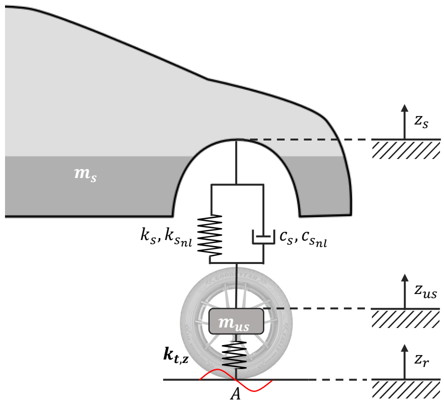

Fig. 4.1 Quarter car model.

together with the tires, they can be easily powered, and they do not require a wireless data transmission to communicate the measurements.

4.2 Quarter Car Model

The inflation pressure of the tire was estimated based on a 2DOF Quarter Car (QC) non-linear model for passive suspensions, widely used to study, in ride comfort analyses, the vertical motion of vehicles caused by roads' surface unevenness [123]. It assumes the coupling of pitch, roll and heave motions of the vehicle are negligible, since it has poor significance for typical passenger-cars [124]. The model, in Figure 4.1, consists of basic elements of the suspension system such as sprung mass m_s (representing sprung mass of a vehicle quarter) connected via a spring and a damper (representing the suspension system) to the unsprung mass m_{us} (representing the wheel assembly). The fundamental assumption of the model is to neglect the effects of suspension systems' complex linkages [125]. Suspension systems generally exhibit non-linear behaviour [126], which can be taken into account considering a cubic stiffness $k_{s_{nl}}$ in parallel with a linear stiffness k_s [127], and a quadratic damping non-linearity modelled with linear c_s and non-linear damping coefficients $c_{s_{nl}}$ [123]. The vertical behaviour of the unsprung mass is modelled with a "single point contact model" approach [128], composed of a spring with a linear stiffness k_t (representing tire), while damping contribution is neglected [129]. It considers that the entire part of the tire in contact with the road is reduced to a single point contact A, which receives from the road a displacement according to its surface profile $z_r(t)$. This approach for modelling vehicle dynamics reduces the complexity of the system, while being highly effective [130]. For a 2DOF QC non-linear model representing 1/4th of a vehicle passive suspension system, according to d'Alembert's principle, the governing equations of motion are:

$$\begin{aligned} m_s\ddot{z}_s &= -k_s\left(z_s - z_{us}\right) - k_{s_{nl}}\left(z_s - z_{us}\right)^3 - c_s\left(\dot{z}_s - \dot{z}_{us}\right) - c_{s_{nl}}\left(\dot{z}_s - \dot{z}_{us}\right)^2 \\ m_{us}\ddot{z}_{us} &= -k_s\left(z_{us} - z_s\right) - k_{s_{nl}}\left(z_{us} - z_s\right)^3 - c_s\left(\dot{z}_{us} - \dot{z}_s\right) - c_{s_{nl}}\left(\dot{z}_{us} - \dot{z}_s\right)^2 - k_{t,z}\left(z_{us} - z_r\right) \end{aligned} \tag{4.1}$$

with the sprung mass of a vehicle quarter m_s, calculated as [129]:

$$m_s = \frac{1}{2} m_{s,vehicle} \frac{a_2}{a_1 + a_2} \tag{4.2}$$

where, z_s is the vertical displacement of the sprung mass, z_{us} the is the vertical displacement (hop) of the unsprung mass, a_1 and a_2 are the semi-wheelbases. The total sprung mass of the vehicle $m_{s,vehicle}$ is calculated as the sum of vehicle chassis mass $m_{chassis}$ (vehicle body) and loading mass m_{load}, $m_{s,vehicle} = m_{chassis} + m_{load}$. The proposed methodology indirectly estimates the tire pressure using its explicit relationship with the tire vertical stiffness. According to preliminary investigations, drawing an indirect estimation of tire inflation pressure by direct estimation of tire stiffness, during vehicle driving, seems to be a promising solution [42]. The relationship between the rolling dynamic vertical stiffness and the inflation pressure can be reasonably assumed as linear [131], neglecting viscoelastic properties of the tire, since the 2DOF QC non-linear model operates under transient inputs [132]. This assumption can be successfully used to indirectly monitor the tire inflation pressure [65]. A linear relationship between vertical stiffness and inflation pressure of the tire is used [9]:

$$k_{t,z} = k_{t,z_0}\left(1 + p_{Fz_1} dpi\right) \tag{4.3}$$

with,

$$dp_i = \frac{p_{eff} - p_0}{p_0} \tag{4.4}$$

where, p_0 is the nominal pressure of the inflated tire, p_{eff} is the effective inflation pressure of the tire, k_{t_0} is the vertical stiffness at the nominal inflation pressure p_0, and p_{Fz_1} is the coefficient representing the pressure effect on vertical stiffness. The 2DOF QC non-linear model reliable simulates vertical dynamics of vehicles if its input, road surface profile, is known. We have adopted a methodology to reproduce tire excitation by road-roughness numerically. Considering a single specific degree of road roughness, according to one of A–H classes of ISO (International Organization for Standardization) 8608 classification [114], the Power Spectral Density (PSD) of the road-velocity profile $\dot{z}_r$ can be assumed to be essentially flat [133]. The tire excitation by road-roughness z_r is generated in time domain, non-linear vehicle models requirement, filtering a white-noise with a first-order linear shape filter [112], described in Chapter 3.3.3.

4.3 Interacting Multiple Model Filter

The road surface profile acts as a disturbance input to the suspension system, which is a critical issue in simulating car vertical dynamics, since it is not known a-priori. The prediction model adopted partially mitigates this problem, generating tire excitation by road roughness numerically. However, reliable simulation of the effective car vertical dynamics can be only carried out if the modelled tire-road interaction truly reflects the actual conditions. The

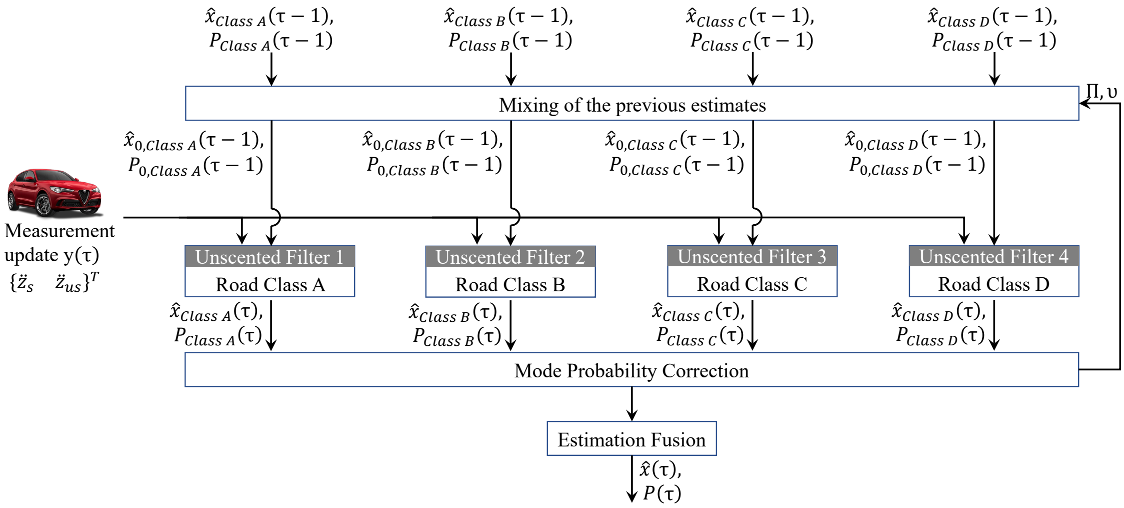

Fig. 4.2 Scheme of the interacting multiple model unscented filter.

implemented methodology numerically generates tire excitation conforming to a specific ISO 8608 road roughness class, according to the parameter a of the Equation (3.26). The road class that the vehicle is driving in is not known $a-priori$, and can abruptly change during driving. We address this issue through the Interacting Multiple Model (IMM) approach composed of a bank of nonlinear Unscented Kalman Filters (UKF).

4.3.1 Interacting Multiple Model Algorithm

In this work an IMM based on the Unscented Kalman Filters are adopted as estimators for the tire inflation pressure so as to deal with changing of road surface roughness. The IMM system is governed by two relationships:

$$
\begin{aligned}
x_{\tau+1} &= f_s(x_\tau, u_\tau) + \nu_\tau \\
y_\tau &= h_s(x_\tau) + \rho_\tau
\end{aligned}
\tag{4.5}
$$

where $f_s(\cdot)$ is the process function, $h_s(\cdot)$ is the measurement function, $s \in \{0, 1, \ldots, S\}$ is the state mode. The IMM system is composed of a bank of multiple KFs, identified by value of s, each of them tailored to represent ride dynamics behaviour of the vehicle for one of road classes that the vehicle could driving in. Here, nonlinear f_s and h_s are considered; thus nonlinear filters, such as UKFs, must be used. The interacting multiple model unscented filter is given by an algorithm composed of steps reported below.

1. Mixing probabilities $\upsilon_{i|j}(\cdot|\cdot)$ evaluation,

$$\upsilon_{i|j}(\tau-1|\tau-1)=\frac{1}{\bar{c}_j}\Pi_{ij}\upsilon_i(\tau-1)$$

   being $\bar{c}_j=\sum_{i=1}^{S}\upsilon_{Markov,ij}\upsilon_i(\tau-1)$, where, $\upsilon_i(\tau-1)$ is the mode probability at time $(\tau-1)$, Π is the transition probability matrix, and $\upsilon_{Markov,ij}$ is the Markov transition probability from mode i to mode j, while Π_{ij} denotes the state transfer probability from model i to model j. The mixed initial state condition $\hat{x}_{0j}(\tau-1|\tau-1)$ and covariance $P_{0j}(\tau-1|\tau-1)$ for mode-matched filter j at time $\tau-1$ are

$$\begin{aligned}\hat{x}_{0j}(\tau-1|\tau-1)&=\sum_{i=1}^{S}\hat{x}_i(\tau-1|\tau-1)\upsilon_{i|j}(\tau-1|\tau-1),\\ P_{0j}(\tau-1|\tau-1)&=\sum_{i=1}^{S}\upsilon_{i|j}(\tau-1|\tau-1)(P_i(\tau-1|\tau-1)\\ &\quad+[\hat{x}_i(\tau-1|\tau-1)-\hat{x}_{0j}(\tau-1|\tau-1)]\cdot\\ &\quad\cdot[\hat{x}_i(\tau-1|\tau-1)-\hat{x}_{0j}(\tau-1|\tau-1)]^\top)\end{aligned}$$

   where, $\hat{x}_i(\tau-1|\tau-1)$ denotes the state estimate for mode-matched filter i at time $\tau-1$ and $P_i(\tau-1|\tau-1)$ its covariance matrix.

2. Estimation via nonlinear Kalman filter is used to obtain the posterior state estimation $\hat{x}_j(\tau|\tau)$, the state covariance matrix $P_j(\tau|\tau)$, the measurement output $\hat{y}_j(\tau|\tau-1)$ and the corresponding covariance matrix $P_{yy}^{j,\tau|\tau-1}$ for the $j-$th model.

3. Model probability update. Under the Gaussian assumption, the likelihood function Λ_j can be evaluated as a function of the residual N_j with respect to measurement $y(\tau)$

$$\begin{aligned}\Lambda_j(\tau)&=\frac{\exp\{-\frac{1}{2}(N_j(\tau)^\top(P_{yy}^{j,\tau|\tau-1})^{-1}N_j(\tau))\}}{\sqrt{2\pi P_{yy}^{j,\tau|\tau-1}}},\\ N_j(\tau)&=y(\tau)-\hat{y}_j(\tau|\tau-1)\end{aligned}$$

Then, the model probability is calculated as

$$\upsilon_j(\tau) = \frac{1}{\sum_{j=1}^{S} \Lambda_j(\tau)\bar{c}_j} \Lambda_j(\tau)\bar{c}_j$$

4. Output interacting is obtained combining the previous results from each filter, obtaining the state estimation $\hat{x}(\tau|\tau)$ at time τ and its covariance $P(\tau|\tau)$ according to

$$\begin{aligned}
\hat{x}(\tau|\tau) &= \sum_{i=1}^{S} \hat{x}_j(\tau|\tau)\mu_j(\tau), \\
P(\tau|\tau) &= \sum_{i=1}^{S} \mu_j(\tau)(P_j(\tau|\tau) + [\hat{x}_j(\tau|\tau) - \hat{x}(\tau|\tau)] \cdot [\hat{x}_j(\tau|\tau) - \hat{x}(\tau|\tau)]^\top)
\end{aligned}$$

4.3.2 Unscented Kalman Filter Algorithm

The Unscented Kalman Filter is a suboptimal solution for the stochastic filtering problem of a discrete-time, dynamical system described either in the additive form

$$\begin{aligned}
x_{\tau+1} &= f(x_\tau, u_\tau) + \nu_\tau \\
y_\tau &= h(x_\tau) + \rho_\tau
\end{aligned} \tag{4.6}$$

where $f(\cdot)$ is the process function, $h(\cdot)$ is the measurement function, $x \in R^{n_x}$ is the state vector, τ is the time instant, and $y \in R^{n_y}$ is the measurement vector. The process ν_τ and measurement ρ_τ noises are both assumed as zero-mean uncorrelated processes with covariances Q_τ and R_τ, respectively. The UKF keep the structure of the linear Kalman filter of one prediction (or a priori estimation) and one correction (or update) step. Consider eq. 4.6 and suppose that, at time step τ, $\hat{x}_{\tau-1|\tau-1}$ and $\hat{P}_{xx}^{\tau-1|\tau-1}$ are given. Choose a real $\kappa > -n_x$ and define, for $1 \le i \le n_x$, the weights and points

$$\begin{aligned}
&w_0 := \tfrac{\kappa}{n_x+\kappa}, w_i = w_{i+n_x} := \tfrac{1}{2(n_x+\kappa)}, \chi_0^{\tau-1|\tau-1} := \hat{x}_{\tau-1|\tau-1} \\
&\chi_i^{\tau-1|\tau-1} := \hat{x}_{\tau-1|\tau-1} + \left(\sqrt{(n_x+\kappa)\hat{P}_{xx}^{\tau-1|\tau-1}}\right)_{*i} \\
&\chi_{i+n_x}^{\tau-1|\tau-1} := \hat{x}_{\tau-1|\tau-1} - \left(\sqrt{(n_x+\kappa)\hat{P}_{xx}^{\tau-1|\tau-1}}\right)_{*i}
\end{aligned} \tag{4.7}$$

For $0 \le i \le 2n_x$, define the transformed sigma points

$$\chi_i^{\tau|\tau-1} := f\left(\chi_i^{\tau-1|\tau-1}, \tau\right), \ \gamma_i^{\tau|\tau-1} := h\left(\chi_i^{\tau|\tau-1}, \tau\right) \tag{4.8}$$

and their associated statistics ($(A)(\diamond)^T$ stands for $(A)(A)^T$)

$$\begin{array}{l} \hat{x}_{\tau|\tau-1} := \sum_{i=0}^{2n_x} w_i \chi_i^{\tau|\tau-1},\ \hat{y}_{\tau|\tau-1} := \sum_{i=0}^{2n_x} w_i \gamma_i^{\tau|\tau-1} \\ \hat{P}_{xx}^{\tau|\tau-1} := \sum_{i=0}^{2n_x} w_i \left(\chi_i^{\tau|\tau-1} - \hat{x}_{\tau|\tau-1}\right)(\diamond)^T + Q_\tau \\ \hat{P}_{xy}^{\tau|\tau-1} := \sum_{i=0}^{2n_x} w_i \left(\chi_i^{\tau|\tau-1} - \hat{x}_{\tau|\tau-1}\right)\left(\gamma_i^{\tau|\tau-1} - \hat{y}_{\tau|\tau-1}\right)^T \end{array} \tag{4.9}$$

along with the innovation's covariance

$$\hat{P}_{yy}^{\tau|\tau-1} := \sum_{i=0}^{2n_x} w_i \left(\gamma_i^{\tau|\tau-1} - \hat{y}_{\tau|\tau-1}\right)(\diamond)^T + R_\tau \tag{4.10}$$

Finally, instantiate the KF's correction equations

$$\begin{array}{l} G_\tau := \hat{P}_{xy}^{\tau|\tau-1}\left(\hat{P}_{yy}^{\tau|\tau-1}\right)^{-1}, \hat{x}_{\tau|\tau} := \hat{x}_{\tau|\tau-1} + G_\tau(y_\tau - \hat{y}_{\tau|\tau-1}) \\ \hat{P}_{xx}^{\tau|\tau} := \hat{P}_{xx}^{\tau|\tau-1} - G_\tau \hat{P}_{yy}^{\tau|\tau-1} G_\tau^T \end{array} \tag{4.11}$$

4.4 Tire Inflation Pressure Estimation via IMM

The proposed IMMUKF for estimation of the tire inflation pressure is schematized in Figure 4.2. It consists of a bank of UKF, each of them with a prediction model able to represent ride dynamics behaviour of the vehicle when driving on a road belonging to a specific ISO class. Usually, road profiles hardly belong to classes worse than D (repair interventions should be performed to restore optimal conditions), so, only the classes A (very good), B (good), C (average) and D (poor) are considered; therefore, the proposed multiple model, to be able to estimate the inflation pressure when vehicle driving on roads whose roughness level can significantly change, a bank of four UKF is considered. The state vector considered is $x = [z_s, z_{us}, \dot{z}_s, \dot{z}_{us}, k_{t,z}]^T \in \mathbb{R}^{5\times1}$. Since measurements available to the IMMUKF are the sprung and unsprung vertical acceleration, $\ddot{z}_s$ and $\ddot{z}_{us}$, the measurement vector is $y = [\ddot{z}_s, \ddot{z}_{us}]^T \in \mathbb{R}^{2\times1}$. To indirectly estimate the tire inflation pressure, the tire vertical stiffness $k_{t,z}$ is modelled as a random walk process [134] that artificially varies the parameters at every sampling instant. Discretizing 2DOF QC nonlinear model equations through the forward Euler method, the particular nonlinear function $f_s(.)$ of the state equations is given by:

$$\begin{cases} z_{s_{\tau+1}} = z_{s_\tau} + [\dot{z}_{s_\tau}]\,\Delta t \\ z_{us_{\tau+1}} = z_{us_\tau} + [\dot{z}_{us_\tau}]\,\Delta t \\ \dot{z}_{s_{\tau+1}} = \dot{z}_{s_\tau} + \left[\frac{-k_s(z_{s\tau}-z_{us\tau})-k_{s_{nl}}(z_{s\tau}-z_{us\tau})^3-c_s(\dot{z}_{s\tau}-\dot{z}_{us\tau})-c_{s_{nl}}(\dot{z}_{s\tau}-\dot{z}_{us\tau})^2}{m_s}\right]\Delta t \\ \dot{z}_{us_{\tau+1}} = \dot{z}_{us_\tau} + \left[\frac{-k_s(z_{us\tau}-z_{s\tau})-k_{s_{nl}}(z_{us\tau}-z_{s\tau})^3-c_s(\dot{z}_{us\tau}-\dot{z}_{s\tau})-c_{s_{nl}}(\dot{z}_{us\tau}-\dot{z}_{s\tau})^2-k_{t\tau}(z_{us\tau}-z_r)}{m_{us}}\right]\Delta t \\ k_{t_{\tau+1}} = k_{t_\tau} + w_{t_\tau} \end{cases} \tag{4.12}$$

where, w_{t_τ} is assumed to be zero mean Gaussian white noise process with variance σ_t. The measurement function $h_s(.)$ is as follows:

$$\begin{cases} \ddot{z}_{s_\tau} = \frac{-k_s(z_{s\tau}-z_{us\tau})-k_{s_{nl}}(z_{s\tau}-z_{us\tau})^3-c_s(\dot{z}_{s\tau}-\dot{z}_{us\tau})-c_{s_{nl}}(\dot{z}_{s\tau}-\dot{z}_{us\tau})^2}{m_s} \\ \ddot{z}_{us_\tau} = \frac{-k_s(z_{us\tau}-z_{s\tau})-k_{s_{nl}}(z_{us\tau}-z_{s\tau})^3-c_s(\dot{z}_{us\tau}-\dot{z}_{s\tau})-c_{s_{nl}}(\dot{z}_{us\tau}-\dot{z}_{s\tau})^2-k_{t\tau}(z_{us\tau}-z_r)}{m_{us}} \end{cases} \tag{4.13}$$

The transition probability matrix Π, to assign the same probability to each mode, is defined as:

$$\Pi = \begin{pmatrix} 0.97 & 0.01 & 0.01 & 0.01 \\ 0.01 & 0.97 & 0.01 & 0.01 \\ 0.01 & 0.01 & 0.97 & 0.01 \\ 0.01 & 0.01 & 0.01 & 0.97 \end{pmatrix} \tag{4.14}$$

The process noise covariance matrix Q is defined as:

$$Q_\tau = \begin{pmatrix} q_1\Delta t^3 & 0 & 0 & 0 & 0 \\ 0 & q_2\Delta t^3 & 0 & 0 & 0 \\ 0 & 0 & q_3\Delta t^3 & 0 & 0 \\ 0 & 0 & 0 & q_4\Delta t^3 & 0 \\ 0 & 0 & 0 & 0 & q_5\Delta t^3 \end{pmatrix} \tag{4.15}$$

where q_0–q_5 are five tuning parameters of the IMMUKF, and Δt is the sampling time of the filter. While the covariance matrix of measurement noise R_τ is defined as:

$$R_\tau = \begin{pmatrix} \sigma_{az_s} & 0 \\ 0 & \sigma_{az_{us}} \end{pmatrix} \tag{4.16}$$

being σ_{az_s} and $\sigma_{az_{us}}$ the respective standard deviations.

4.5 Algorithm Validation

In this section, the effectiveness of the approach is assessed through a numerical campaign, based on simulation platform described in Chapter 2. First Monte Carlo simulation was carried out to compare tire inflation pressure estimation accuracy by the proposed methodology with respect to a single unscented filter. Then, the capability of the IMMUKF to deal with abruptly change of road surface profile class and tire inflation pressure was verified.

4.5.1 2DOF QC Parameters Identification

As mentioned above, the IMMUKF consists of a bank of four UKF, each with different parameterisations for the prediction model. Specifically, the approach provides one model properly parametrised to represent the ride dynamics behaviour of the vehicle for each of A - D road classes that the vehicle could driving in. Herein, for each of these four classes, we have tailored a prediction model to the ASM high-fidelity vehicle simulation by levering the results obtained from several numerical simulations [135]. By doing so, we have obtained prediction models that reliable reproduce the ride dynamics behaviour of the vehicle under several roads, belonging to A - D classes, such that they can be exploited for the estimation methodology. Four system identification problems have been solved, one for each of the A - D road classes, any of them formulated as an optimization task where the objective was to find a set of parameters that minimizes the prediction error between outputs of the ASM simulation, and the 2DOF QC model [136]. Two outputs have been considered, the vertical accelerations of sprung $\ddot{z}_s$ and unsprung $\ddot{z}_{us}$ masses, here computed considering the tire inflation pressure (parameter to be estimated) and the road surface profile (that acts as unknown input during estimation) as known inputs. More specifically, the outputs have been computed in nine simulation scenarios, by combining three vehicle speeds (40, 60 and 80 km/h) and three tire inflation pressures (130, 180 and 230 kPa), in a straight-line manoeuvre, considering the road model of ASM environment subsystem set to provide properties of road according to one of the classes. The exploited identification procedure has been performed four times, changing the road from class A to D, which, leveraging a Genetic Algorithm (GA), found four sets of parameters for the 2DOF QC model, respectively. Each prediction model is characterized by 12 parameters, four of which, listed in the Table 4.1, were unknown and needed to be identified; therefore we have considered these four parameters as decision variables of the optimization task. The Root Mean Square Error (RMSE) between the ASM simulation and the 2DOF QC model outputs, $\ddot{z}_s$ and $\ddot{z}_{us}$, in the nine simulation scenarios, have been defined

Table 4.1 2DOF QC model unknown parameters.

Parameter	Description
c_s	Linear damping coefficient
$c_{s_{nl}}$	Non-linear square damping coefficient
k_s	Linear spring stiffness coefficient
$k_{s_{nl}}$	Non-linear cube spring stiffness coefficient

as objective functions to be minimized, as:

$$\sqrt{\frac{1}{N}\sum_{k=1}^{N}\left(\ddot{z}_s(\tau)-\hat{\ddot{z}}_s(\tau)\right)^2} \tag{4.17}$$

$$\sqrt{\frac{1}{N}\sum_{k=1}^{N}\left(\ddot{z}_{us}(\tau)-\hat{\ddot{z}}_{us}(\tau)\right)^2} \tag{4.18}$$

where, N is the number of samples.

The population size was set according to the technical literature [137], while, the one-point crossover method and the bit-string mutation were used for the crossover and the mutation, respectively [138]. The number of generation was set to 1000, enough for identifying solutions belonging to the 18-dimensional hypersurface of the Pareto frontier. Among the dominant solutions, the one situated at the minimum distance from the origin of the 18-dimensional hyperspace was considered. Solutions of the four system identification problems are reported in Table 4.2, where each of its columns contains parameter values for the 2DOF QC model exploitable to simulate ride dynamics behaviour of the vehicle under test on roads belonging to one of the four A - D classes. The results of the identification problems,

Table 4.2 Optimal solutions of the four system identification problems.

Parameter	Road class A	Road class B	Road class C	Road class D
c_s $[Ns/m]$	6576	4585	14819	14708
$c_{s_{nl}}$ $[Ns/m^2]$	4319	6016	5839	4555
k_s $[N/m]$	113086	173415	94544	118114
$k_{s_{nl}}$ $[N/m^3]$	130098	151886	62836	121723

therefore, have a poor physical meaning, since they not are the real stiffness and damping coefficients of the vehicle suspension system, but are values identified by the optimization methodology to reproduce the input/output behaviour of the vehicle system. To verify the effectiveness of the identification procedure, a test has been executed: simulation scenario consists of a straight-line manoeuvre with a constant speed of 60 km/h, on a class B road. Results in terms of unsprung mass vertical acceleration are reported in Figures 4.3a and 4.3b for tire inflation pressures of 230 kPa and 130 kPa, respectively. In particular, these Figures

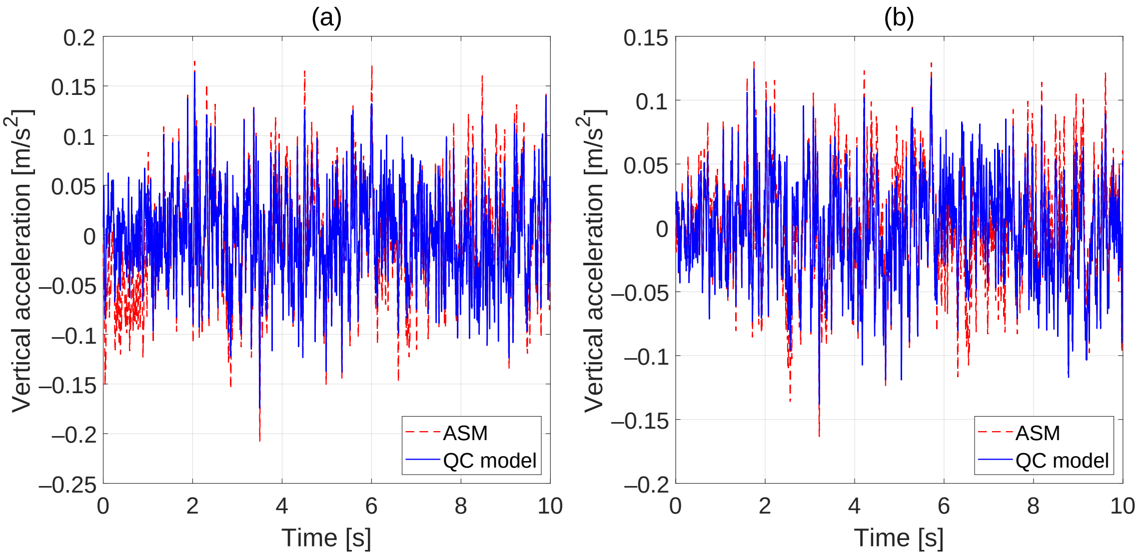

Fig. 4.3 Unsprung mass acceleration; (**a**) tire inflation pressure 230 kPa; and (**b**) tire inflation pressure 130 kPa. Vehicle speed 60 km/h, road class B.

show a comparison between the vertical acceleration of unsprung mass computed with ASM (dashed red line) and the one calculated with the QC model (blue line). Discrepancies can be noted due to several assumptions on which the simplified QC model is based on. Indeed, as mentioned above, the QC model assumes negligible the pitch, roll and heave motions of the vehicle [124]. Moreover, it neglects the effects of suspension kinematics and compliance [125], which undermine the QC's predictive capability [130]. However, the identification procedure have mitigated the un-modelled dynamics of the QC successfully, as demonstrated by RMSE on $\ddot{z}_{us}$, equal to 0.03 m/s^2 and 0.025 m/s^2 for tire inflation pressures of 230 kPa and 130 kPa, respectively.

4.5.2 Monte Carlo Analysis

To assess the tire inflation pressure estimation accuracy by the proposed methodology, a Monte Carlo numerical campaign has been carried out. The Monte Carlo method is generally used to evaluate the uncertainty of estimations [139], since it leads to more advantages then conventional methods, which require the evaluation of the separate effect of each input quantity on the result through a parametric analysis [140]. When, in a complex system, multiple input variables are correlated, uncertainty analysis become a not trivial task and sometimes even unreliable. Monte Carlo simulation [141, 142] is a probabilistic method to solve deterministic problems thanks to the use of electronic calculators, which can simulate a lot of experimental trials that have random outcomes. When applied to uncertainty evaluation, random numbers are generated to randomly sample parameters' uncertainty space. Such an analysis is closer with the probabilistic nature of the actual processes. Both the IMMUKF and the single UKF solutions have been tested executing a set of 100 simulations. The initial conditions $\hat{x}_{0|0}$ were varied as a normal distribution with mean value equal to true value of the initial vehicle state x_0, i.e., $\hat{x}_{0|0} \in \mathcal{N}(x_0, \sqrt{P_{0|0}})$. The initial covariance error matrix $P_{0|0}$ is selected in accordance with the variances of the initial conditions, as:

$$P_{0|0} = diag[\sigma^2_{z,s}, \quad \sigma^2_{z,us}, \quad \sigma^2_{v_{z,s}}, \quad \sigma^2_{v_{z,us}}, \quad \sigma^2_{k,t}]. \tag{4.19}$$

The driving simulation scenario is characterized by Straight-line: starting from initial vehicle state $x_0 = [0,0,0,0,k_{t,z0}]^T$, the vehicle drives straight ahead at constant speed $v_{x,Vehicle}$ on a road whit a profile belonging to a specific ISO class (constant value of the parameter a_{Road} of the Eq. 3.26), keeping constant the value of tire inflation pressure p_{eff} for all 20 s of simulation. The scenario' parameters (i.e. p_{eff}, $v_{x,Vehicle}$ and a_{Road}) have been made to vary following the Monte Carlo approach as random variables with uniform distribution within the ranges reported in the Table 4.3. The measurements employed in the IMMUKF are acquired

Table 4.3 Scenario parameters range.

Parameter	**Range**
p_{eff}	(130-230) $[kPa]$
$v_{x,Vehicle}$	40-80 $[km/h]$
a_{Road}	0-3 [-]

with the high-fidelity vehicle simulation model and corrupted by zero-mean, Gaussian noises:

$$\begin{cases} \ddot{z}_s = \ddot{z}_{s_{true}} + \nu_{az_s}, & \nu_{az_s} \in \mathcal{N}(0, \sigma_{az_s}) \\ \ddot{z}_{us} = \ddot{z}_{us_{true}} + \nu_{az_{us}}, & \nu_{az_{us}} \in \mathcal{N}(0, \sigma_{az_{us}}) \end{cases} \tag{4.20}$$

where, σ_{az_s} and $\sigma_{az_{us}}$ are the values of the noise covariances. In this numerical campaign, they were both set equal to 0.5 m/s^2, as reported in the sensors datasheets. The single UKF used to compare the results is based on the same model parametrised for the road class A. The results of the Monte Carlo simulation require a post-processing to clearly represent the uncertainty of the estimation algorithm. Three indexes have been considered:

- mean estimation error $\bar{e}_\tau$ obtained on N Monte Carlo samples (red line). For each τ-th time step, the following performance index is evaluated:

$$\bar{e}_\tau = \frac{1}{N} \sum_{\chi=1}^{N} (x_{\tau,\chi} - \hat{x}_{\tau,\chi}); \tag{4.21}$$

- standard deviation of the estimation errors obtained on N Monte Carlo samples (dashed blue line), evaluated for each τ-th time step as:

$$\sigma_\tau = \sqrt{\frac{1}{N-1}\sum_{\chi=1}^{N} |(x_{\tau,\chi} - \hat{x}_{\tau,\chi}) - \bar{e}_\tau|^2}; \tag{4.22}$$

- estimation error of a single Monte Carlo sample (green line).

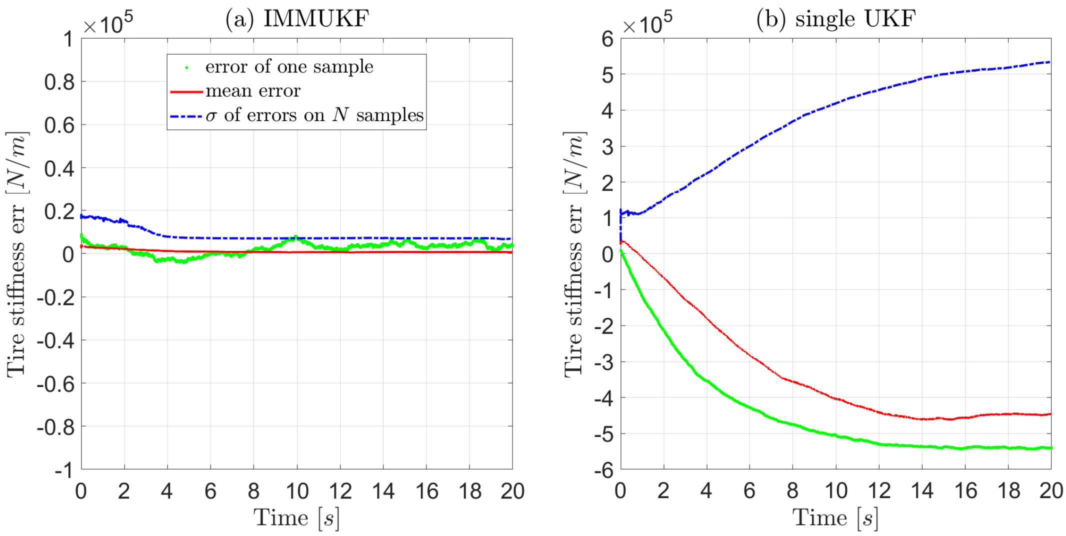

Fig. 4.4 (**a**) IMMUKF and (**b**) classic UKF estimation error on $k_{t,z}$.

The results show how the IMMUKF outperforms the single filter solution. Indeed, the mean error is around zero; the standard deviation converges to the true value, lower than the single UKF solution; and the sample estimation error remains within bounds defined by the standard deviation of the errors for all the simulation time. Instead, the single UKF exhibits a divergence in the estimation of tire stiffness. More specifically, the green line in the Figg. is the estimation error of a single Monte Carlo sample, selected among the N samples to highlight the maximum estimation error. Specifically, it refers to a simulation scenario that consider an ISO class D for the road profile. The estimation error of the single UKF converges to $-5.3\ N/m$, which exhibits, therefore, poor estimation properties with respect to high uneven road surface, leading to a relative error of 270%. These results confirm the possibility to use a Multiple Model algorithm to deal with more realistic and non-trivial scenarios.

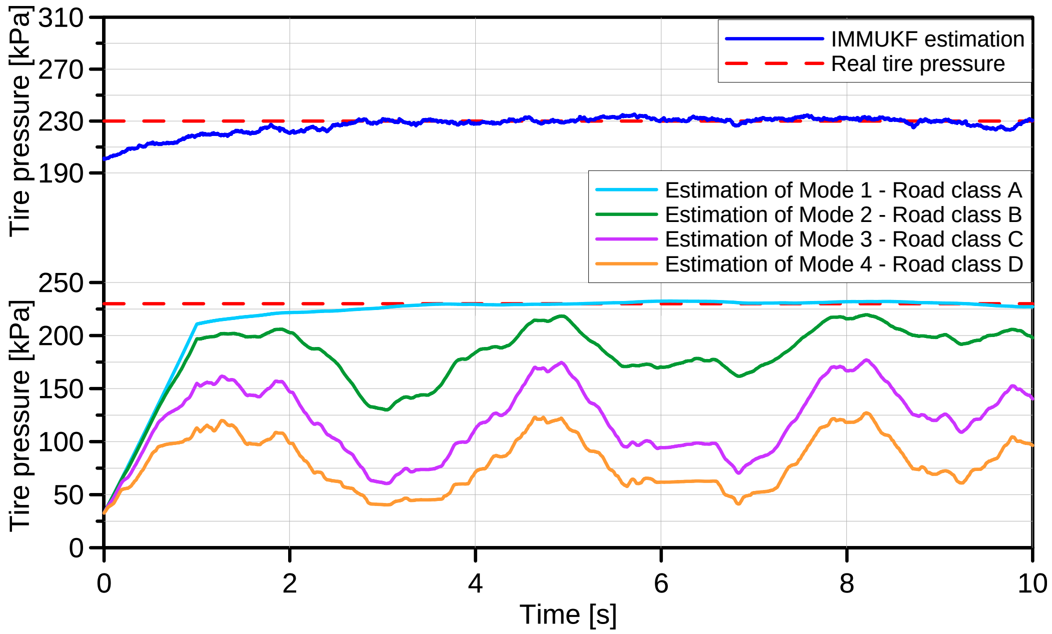

Fig. 4.5 Estimation of tire pressure on an ISO class A road.

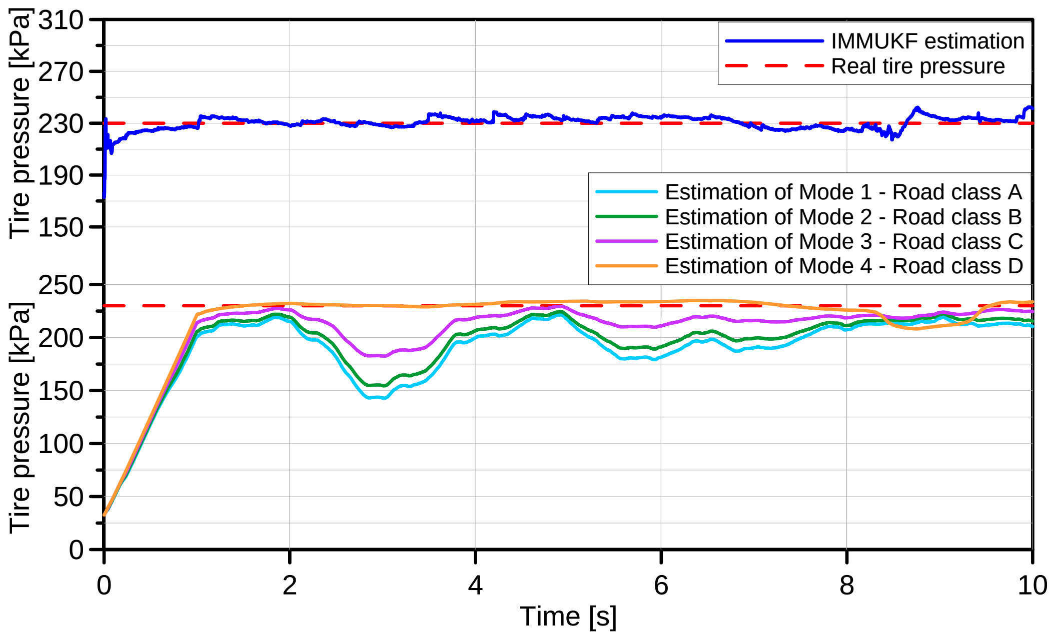

Fig. 4.6 Estimation of tire pressure on an ISO class D road.

4.5.3 Tire Inflation Pressure Estimation

To assess the capability of IMMUKF to deal with abrupt changes of road surface profile class and tire inflation pressure, several numerical simulations have been executed. Figure 4.5

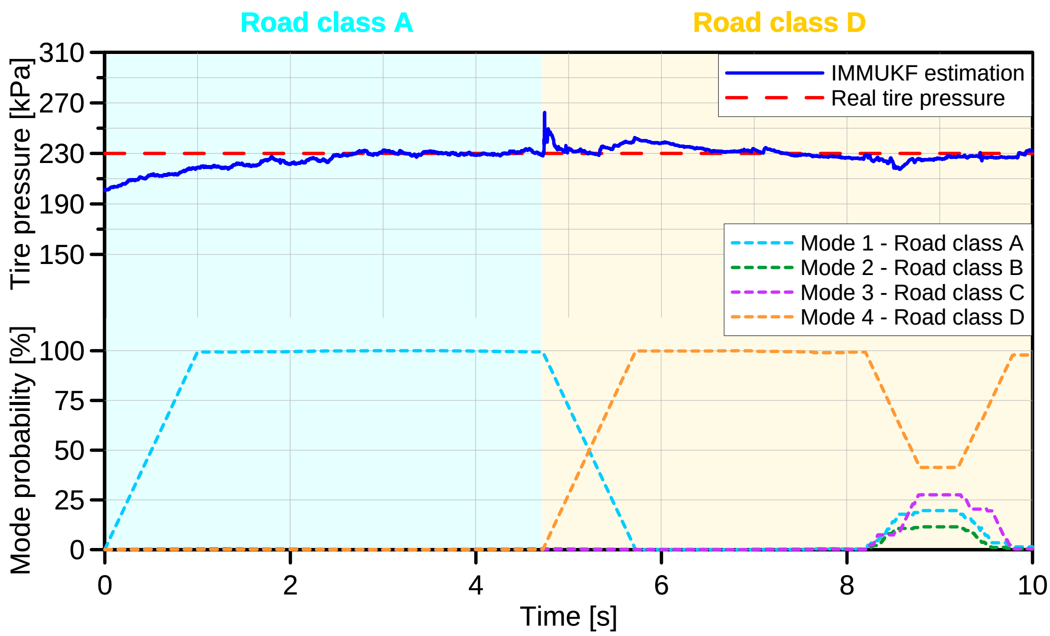

Fig. 4.7 Estimation of tire pressure with abrupt change of class for road surface profile.

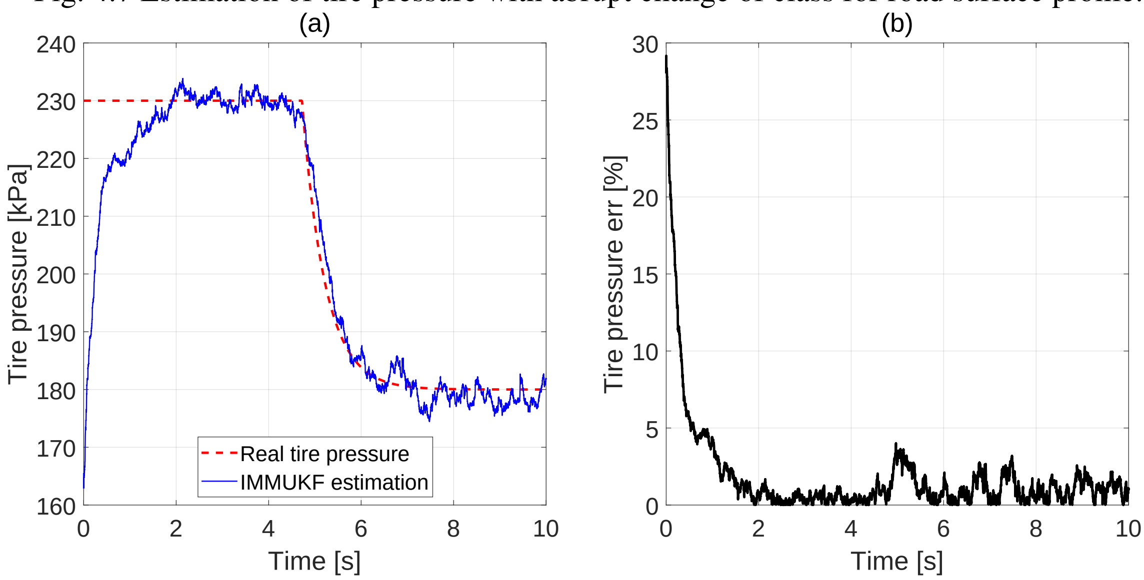

Fig. 4.8 (**a**) Estimation of tire pressure with abrupt change of tire inflation pressure and (**b**) estimation error.

shows the results of a simulation scenario where a road profile according to ISO class A was considered. In the top, it can be noted that after 2 of 10 s of simulation, the IMMUKF converges to an acceptable estimation of tire inflation pressure. In the bottom of Figure 4.5 are reported the moving average of each single mode estimation: as shown, mode 1, exploitable for estimation on roads of class A, fast converges to a real value of tire inflation pressure,

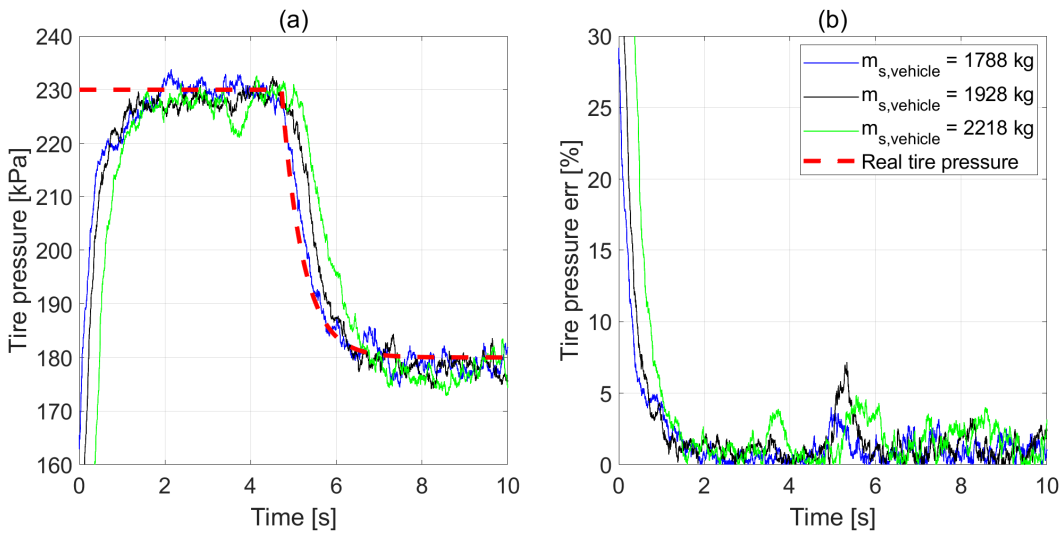

Fig. 4.9 (**a**) Estimation of tire pressure with respect to different total sprung mass of the vehicle $m_{s,vehicle}$ and (**b**) estimation errors.

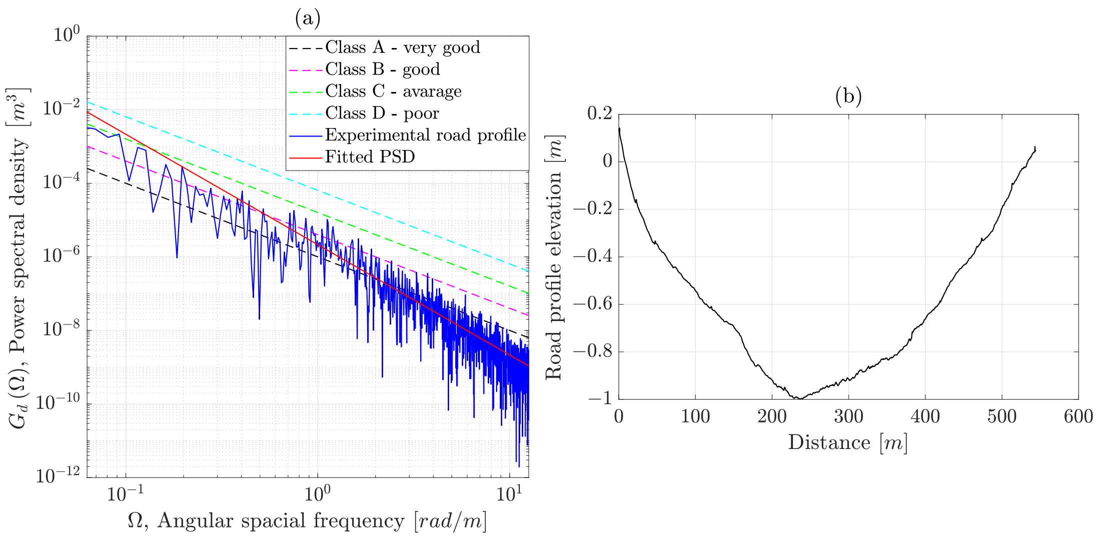

Fig. 4.10 (**a**) Power spectral density of (**b**) experimental road profile.

while the other modes diverge to much lower values. Similarly, Figure 4.6 shows the results of a simulation executed on a road with a ISO class D profile, confirming the capability of the IMMUKF to estimate tire inflation pressure on different road, without a-priori information on surface profile.

To verify the capability of the IMMUKF to deal with abrupt changes of road surface profile class, a scenario with two different road surface profiles has been considered. For 5 s of simulation, the vehicle drives on a class A road, and then, with a sudden change of road profile, drives on a class D road. The results, shown in Figure 4.7, highlight how the MM

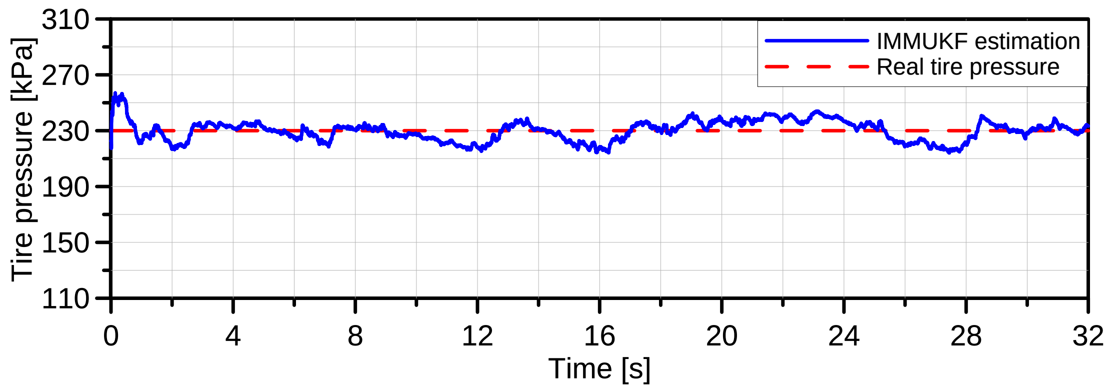

Fig. 4.11 Estimation of tire pressure with experimental road.

approach is able to deal with changes of road pavement conditions, as usually happens in real-world driving. Comparing the measurements to every single prediction, claims are made as to which filter most likely represents the true vehicle dynamics. According to it, the algorithm steps provide for evaluation of the likelihood function of each filter, and their probability is so updated, in order to place more trust in that filter. In particular, for the first 5 s of simulation (class A road), mode 1 has been the most representative, while in the last 5 s (class D road), more trust has been placed in mode 4, as highlighted by the moving averages of modes probability showed in the bottom of Figure 4.7. Instead, to verify the capability of the IMMUKF to estimate tire deflection, a simulation on a class B road was executed, with a sudden reduction of tire inflation pressure from 230 kPa to 180 kPa in about 1.5 s (Figure 4.8). The estimation converges to a real tire inflation pressure value in about 2 s, and then accurately follows the transient behaviour without significant delay in response to the pressure drop, with a low estimation error. A sensitivity analysis has been carried out to investigate the reliability of the proposed algorithm with respect to the variability of the sprung mass of the vehicle, because the vehicle sprung mass depends on loading, which is one of the significant model uncertainties leading to mismatched process noise. Considered constant, the sprung mass of the quarter car model, the nominal sprung mass of the vehicle in the high-fidelity simulation (empty vehicle, 1788 kg) was perturbed by +8% (1928 kg) and +24% (2218 kg), respectively, as shown in Figure 4.9. The estimated and actual inflation pressure show good agreement in the three scenarios. The results highlight the reliability of the estimation algorithm against the uncertainty on vehicle unsprung mass because the mean estimation error is lower than 5%. This behaviour confirms the well-known robustness of the Kalman filter against mismatched process noise covariance due to parameter uncertainty [143]. To be note that, as vehicle mass perturbation increases as the convergence to the true pressure value is slower. This behaviour can be seen in the first 2 s of simulation, since the algorithm corrected the initial estimation error, and after 5 s, when tire deflation has been simulated. Increasing the vehicle mass perturbation (and, therefore, parameter uncertainty), the mismatched process noise covariance increases, causing tire inflation pressure harder to reconstruct. Finally, capability of the proposed algorithm to accurately estimate the tire inflation pressure without information on road surface roughness, on any type of road pavement whose surface roughness belongs to $A-D$ ISO 8608 classification, was proven. To this purpose, an experimental measure of road roughness measured with a mobile LIDAR system, and reported in [144], has been used. In Figure 4.10 is plotted the road displacement Power Spectral Density (PSD) versus angular spatial frequency in a bi-logarithmic plan. In particular, a simulation scenario was considered, that consists of the Segment-D SUV vehicle driving in a road, whose roughness profile is reproduced according to the road roughness measure. Simulation results, in Figure 4.11, show how the algorithm successfully estimates the tire inflation pressure, confirming, in a real-word scenario, the capability of the multiple model approach to work on any type of road pavement, dealing with unknown road surface roughness.

4.6 Conclusions

In this Chapter, an innovative algorithm for the estimation of tire inflation pressure was presented. The estimation is based on an Interacting Multiple Model Unscented Filter scheme that considers a bank of four UKF, each of them exploitable for estimation of ride dynamics behaviour of a car on different road surface profiles, belonging to A - D ISO classes. The validation of the algorithm was carried out with an extensive numerical campaign, using a simulation platform representative of a real SUV vehicle, developed with dSPACE software ASM. Numerical simulations have confirmed the validity of the approach and have disclosed how the estimation of tire inflation pressure could be successfully carried to detect tire deflation, also when the road profile changes.

Chapter 6

Conclusions

Advanced driver-assistance systems, and in particular active safety control systems, are widely used in modern cars to improve vehicle safety and performance. In these systems, the knowledge of vehicle dynamics state and parameters plays a crucial role. Some vehicle states, such as sideslip angle and tire inflation pressure, need to be estimated because of the lack of onboard sensors that can measure them, for technical and economical reasons. Indeed, algorithms used for estimation purposes, to be cost-effectively implemented on-board a vehicle, should work just with CAN-BUS data and low-cost onboard sensors only. The thesis have described research activities carried out to develop and test algorithms for the estimation of these variables. First, the possibility to test iTPMS base on wheel speed signal in HIL environment has been investigated. To this purpose, a simulation platform able to reproduce the two pressure-dependent characteristics of tires inherent in the wheel angular speed, and analysed by the iTPMS to detect pressure losses, has been developed. Although the wheel rolling radius dependency by inflation pressure have been easily modelled using the Magic Formula with micro-parameters dependent by the pressure (MF version 6.1), the simulation of the wheel angular speed whose frequency content considers the effects of tire dynamics response to road excitation is not a trivial task. A new methodology for the development of the wheel speed model has been proposed. In particular, the wheel speed frequency content due to road excitation has been reproduced through a simplified reduced order model. Its parameterization has been carried out with the use of experimental measurement of wheel angular speeds: parameters evaluation has been formulated as an optimization task, where the objective is the minimization of errors between the reduced order model outputs and experimental data. To verify its effectiveness, the methodology has been used to test functionality of a real iTPMS in HIL environment. The results confirm the possibility to check in a virtual environment the two phases of iTPMS algorithm: learning phase, and detection phase. Second half part of the Thesis discloses of the development of new estimation algorithms for tire inflation pressure and vehicle sideslip angle. An IMM model-based algorithm has been proposed to estimate the tire pressure indirectly, dealing with high uneven road surface conditions. Specifically, the IMM is composed of a bank of four UKF, based on a 2DOF quarter car model, each of them able to estimate the tire pressure for a well defined degree of road surface roughness. Then, the IMM, through a weighted average obtained from a probabilistic model, gives an acceptable estimation of the tire pressure, also on highly uneven road surface, without an a-priori knowledge of road roughness. Similarly, for the vehicle sideslip angle a novel estimation strategy has been developed, which not requires tire-road friction coefficient knowledge, based on the IMM filters. By integrating available onboard sensor data, the IMM estimates relevant vehicle information in different driving conditions, emulated through a 2DOF single-track vehicle model and a Dugoff tire model. Specifically, exploiting the nonlinear estimation Kalman theory, two IMM algorithms based on the EKF and UKF are developed. While usually the transition probabilities among models for classical IMMs are fixed and set on prior information and/or dedicated analysis (as in the tire inflation pressure), for the sideslip angle estimation these conservative hypotheses are relaxed introducing a time-varying Markov transition matrix based on a novel model switching algorithm. The effectiveness of these new estimation methods, for both tire inflation pressure and sideslip angle, has been confirmed through extensive realistic driving scenarios, using a high-fidelity vehicle dynamics simulation platform, whose modelling ad validation is described in the Thesis.

6.1 Future Work

This Thesis shows that accurate estimation of sideslip angle under critical driving conditions is possible using low-cost sensors available on ordinary vehicle. A possible direction for this work is to use sideslip angle estimation to enhance the performance of the vehicle motion control systems and to improve the stabilization performances and path tracking capabilities for ADAS systems, specifically in the vehicle lateral control stability in critical driving conditions. In addition, improvement in its estimation can be investigated by considering for state and covariance propagation more detailed vehicle models than the bicycle model. Indeed, the bicycle model does not include the complete dynamics of the vehicle and tires, especially roll steer and chamber changes, which may improve the estimation accuracy across a wide range of manoeuvres. For all estimation algorithm proposed in this Thesis further future works will concern the evaluation of multiple model approach computational effort, which will be useful to verify if the proposed estimation schemes can be successfully implemented for providing vehicle dynamics state information in real-time. This will enable experimental validation of the algorithms through vehicle test on proving grounds.

References

[1] William F Milliken, Douglas L Milliken, and L Daniel Metz. *Race car vehicle dynamics*, volume 400. SAE international Warrendale, 1995.

[2] Charles C MacAdam. Application of an optimal preview control for simulation of closed-loop automobile driving. *IEEE Transactions on systems, man, and cybernetics*, 11(6):393–399, 1981.

[3] United States Environmental Protection Agency. Vehicle and fuel emissions testing: Benchmarking advanced low emission light-duty vehicle technology, 2023. https://www.epa.gov/vehicle-and-fuel-emissions-testing/benchmarking-advanced-low-emission-light-duty-vehicle-technology, last accessed 03 January 2023.

[4] Auto Tecnica. Alfa romeo stelvio, techincal analysis, 2023. https://www.autotecnica.org/alfa-romeo-stelvio-analisi-tecnica/, last accessed 15 March 2023.

[5] Takeshi Yamaguchi, Kazuhiro Tanaka, and Katsuya Suzuki. Dynamics of torque converter with lock-up clutch. 2012.

[6] dSPACE. Automotive simulation models (asm), 2023. https://www.dspace.com, last accessed 15 March 2023.

[7] Hans Pacejka. *Tire and vehicle dynamics*. Elsevier, 2005.

[8] Rolf Isermann. *Automotive control: modeling and control of vehicles*. Springer, 2022.

[9] IJM Besselink, AJC Schmeitz, and HB Pacejka. An improved magic formula/swift tyre model that can handle inflation pressure changes. *Vehicle System Dynamics*, 48(S1):337–352, 2010.

[10] PWA Zegelaar and HB Pacejka. The in-plane dynamics of tyres on uneven roads. *Vehicle System Dynamics*, 25(S1):714–730, 1996.

[11] World Health Organization. Global status report on road safety 2018. 2018.

[12] Bianca Caiazzo, Dario Giuseppe Lui, Alberto Petrillo, and Stefania Santini. Distributed double-layer control for coordination of multiplatoons approaching road restriction in the presence of iov communication delays. *IEEE Internet of Things Journal*, 9(6):4090–4109, 2021.

[13] Alberto Petrillo, Alessandro Salvi, Stefania Santini, and Antonio Saverio Valente. Adaptive multi-agents synchronization for collaborative driving of autonomous vehicles with multiple communication delays. *Transportation research part C: emerging technologies*, 86:372–392, 2018.

[14] Luca Maria Castiglione, Paolo Falcone, Alberto Petrillo, Simon Pietro Romano, and Stefania Santini. Cooperative intersection crossing over 5g. *IEEE/ACM Transactions on Networking*, 29(1):303–317, 2020.

[15] Marco Di Vaio, Paolo Falcone, Robert Hult, Alberto Petrillo, Alessandro Salvi, and Stefania Santini. Design and experimental validation of a distributed interaction protocol for connected autonomous vehicles at a road intersection. *IEEE Transactions on Vehicular Technology*, 68(10):9451–9465, 2019.

[16] Leandro Masello, German Castignani, Barry Sheehan, Finbarr Murphy, and Kevin McDonnell. On the road safety benefits of advanced driver assistance systems in different driving contexts. *Transportation research interdisciplinary perspectives*, 15:100670, 2022.

[17] Anton van Zanten and Robert Bosch. Evolution of electronic control systems for improving the vehicle dynamic behavior. 2002.

[18] Anton T Van Zanten. Bosch esp systems: 5 years of experience. *SAE transactions*, pages 428–436, 2000.

[19] Yimin Chen, Chao Lu, and Wenbo Chu. A cooperative driving strategy based on velocity prediction for connected vehicles with robust path-following control. *IEEE Internet of Things Journal*, 7(5):3822–3832, 2020.

[20] Shouyang Wei, Yuan Zou, Xudong Zhang, Tao Zhang, and Xiaoliang Li. An integrated longitudinal and lateral vehicle following control system with radar and vehicle-to-vehicle communication. *IEEE Transactions on Vehicular Technology*, 68(2):1116–1127, 2019.

[21] Ehsan Hashemi, Milad Jalali, Amir Khajepour, Alireza Kasaiezadeh, and Shih-ken Chen. Vehicle stability control: Model predictive approach and combined-slip effect. *IEEE/ASME Transactions on Mechatronics*, 25(6):2789–2800, 2020.

[22] Wei Liu, Lu Xiong, Xin Xia, Yishi Lu, Letian Gao, and Shunhui Song. Vision-aided intelligent vehicle sideslip angle estimation based on a dynamic model. *IET Intelligent Transport Systems*, 14(10):1183–1189, 2020.

[23] Ric Robinette, Darrell Deering, and Richard J Fay. Drag and steering effects of under inflated and deflated tires. *SAE transactions*, pages 1610–1625, 1997.

[24] King Tin Leung, James F Whidborne, David Purdy, and Alain Dunoyer. A review of ground vehicle dynamic state estimations utilising gps/ins. *Vehicle System Dynamics*, 49(1-2):29–58, 2011.

[25] Yoshio Suzuki and Masato Takeda. An overview on vehicle lateral dynamics and yaw stability control systems. *J. Adv. Vehicle Eng.*, 2(4):182–190, 2016.

[26] Liang Li, Yishi Lu, Rongrong Wang, and Jie Chen. A three-dimensional dynamics control framework of vehicle lateral stability and rollover prevention via active braking with mpc. *IEEE Transactions on Industrial Electronics*, 64(4):3389–3401, 2016.

[27] Simon Sternlund, Johan Strandroth, Matteo Rizzi, Anders Lie, and Claes Tingvall. The effectiveness of lane departure warning systems—a reduction in real-world passenger car injury crashes. *Traffic injury prevention*, 18(2):225–229, 2017.

[28] Wei Liu, Lu Xiong, Xin Xia, and Zhuoping Yu. Vehicle sideslip angle estimation: A review. *SAE Technical Paper 2018-01-0569*, 2018.

[29] Joanny Stephant, Ali Charara, and Dominique Meizel. Virtual sensor: Application to vehicle sideslip angle and transversal forces. *IEEE Transactions on industrial electronics*, 51(2):278–289, 2004.

[30] Haiyan Zhao and Hong Chen. Estimation of vehicle yaw rate and side slip angle using moving horizon strategy. In *2006 6th World Congress on Intelligent Control and Automation*, volume 1, pages 1828–1832. IEEE, 2006.

[31] Guillaume Baffet, Ali Charara, and Daniel Lechner. Estimation of vehicle sideslip, tire force and wheel cornering stiffness. *Control Engineering Practice*, 17(11):1255–1264, 2009.

[32] Moustapha Doumiati, Alessandro Correa Victorino, Ali Charara, and Daniel Lechner. Onboard real-time estimation of vehicle lateral tire–road forces and sideslip angle. *IEEE/ASME Transactions on Mechatronics*, 16(4):601–614, 2010.

[33] Xu Li, Xiang Song, and Chingyao Chan. Reliable vehicle sideslip angle fusion estimation using low-cost sensors. *Measurement*, 51:241–258, 2014.

[34] Marco Gadola, D Chindamo, M Romano, and Fabrizio Padula. Development and validation of a kalman filter-based model for vehicle slip angle estimation. *Vehicle System Dynamics*, 52(1):68–84, 2014.

[35] S Antonov, A Fehn, and A Kugi. Unscented kalman filter for vehicle state estimation. *Vehicle System Dynamics*, 49(9):1497–1520, 2011.

[36] HH Kim and J Ryu. Sideslip angle estimation considering short-duration longitudinal velocity variation. *International Journal of Automotive Technology*, 12(4):545–553, 2011.

[37] Rusty Anderson and David M Bevly. Using gps with a model-based estimator to estimate critical vehicle states. *Vehicle System Dynamics*, 48(12):1413–1438, 2010.

[38] Niclas Persson, Fredrik Gustafsson, and Markus Drevö. Indirect tire pressure monitoring using sensor fusion. *SAE Transactions*, pages 1657–1662, 2002.

[39] Philip MO Owende, Anton M Hartman, Shane M Ward, Michael D Gilchrist, and Michael J O'Mahony. Minimizing distress on flexible pavements using variable tire pressure. *Journal of Transportation Engineering*, 127(3):254–262, 2001.

[40] Thomas Weispfenning. Fault detection and diagnosis of components of the vehicle vertical dynamics. *Meccanica*, 32(5):459–472, 1997.

[41] Selim Solmaz. A Novel Method for Indirect Estimation of Tire Pressure. *Journal of Dynamic Systems, Measurement, and Control*, 138(5), 03 2016.

[42] Giulio Reina, Angelo Gentile, and Arcangelo Messina. Tyre pressure monitoring using a dynamical model-based estimator. *Vehicle system dynamics*, 53(4):568–586, 2015.

[43] Juyong Kang. Robust estimation method of tire torsional resonance frequency to detect decrease in tire inflation pressure. *Vehicle System Dynamics*, pages 1–17, 2021.

[44] AMA Soliman and MMS Kaldas. Semi-active suspension systems from research to mass-market–a review. *Journal of Low Frequency Noise, Vibration and Active Control*, 40(2):1005–1023, 2021.

[45] Xiaolin Ding, Zhenpo Wang, Lei Zhang, and Cong Wang. Longitudinal vehicle speed estimation for four-wheel-independently-actuated electric vehicles based on multi-sensor fusion. *IEEE Transactions on Vehicular Technology*, 69(11):12797–12806, 2020.

[46] Cong Wang, Zhenpo Wang, Lei Zhang, Dongpu Cao, and David G Dorrell. A vehicle rollover evaluation system based on enabling state and parameter estimation. *IEEE Transactions on Industrial Informatics*, 17(6):4003–4013, 2020.

[47] Yung-Hsiang Judy Hsu, Shad M Laws, and J Christian Gerdes. Estimation of tire slip angle and friction limits using steering torque. *IEEE Transactions on Control Systems Technology*, 18(4):896–907, 2009.

[48] Rolf Isermann. *Automotive control: modeling and control of vehicles*. Springer, 2022.

[49] Wenrui Han, Yi Guo, Günther Prokop, and Thomas Roscher. Simulative research on the tire torsional vibration and its vehicle relevant influencing factors. In *19. Internationales Stuttgarter Symposium*, pages 1397–1411. Springer, 2019.

[50] M Gipser and G Hoffmann. Ftire–flexible structure tire model, modelization and parameter specification. *Muenchen: Cosin scientific software*, 2018.

[51] A Gallrein and M Bäcker. Cdtire: a tire model for comfort and durability applications. *Vehicle System Dynamics*, 45(S1):69–77, 2007.

[52] Peter Willem Anton Zegelaar. The dynamic response of tyres to brake torque variations and road unevennesses. 1998.

[53] Stefano Bruni, Federico Cheli, and Ferruccio Resta. On the identification in time domain of the parameters of a tyre model for the study of in-plane dynamics. *Vehicle System Dynamics*, 27(S1):136–150, 1997.

[54] IJM Besselink and AJC Schmeitz. The mf-swift tyre model: Extending the magic formula with rigid ring dynamics and an enveloping model. *JSAE review*, 26(2):245–252, 2005.

[55] Wenrui Han, Günther Prokop, and Thomas Roscher. Model-based development of itpms (indirect tire pressure monitoring system). In *10th International Munich Chassis Symposium 2019*, pages 775–794. Springer, 2020.

[56] Ashraf Elfasakhany. Tire pressure checking framework: A review study. *Reliability Engineering and Resilience*, 1(1):12–28, 2019.

[57] Fredrik Gustafsson, Stefan Ahlqvist, Marcus Drevö, Urban Forssell, and Niclas Persson. Adaptive filter model for motor vehicle sensor signals, January 2 2007. US Patent 7,158,866.

[58] Mikao Nakajima. Device for determining initial correction factor for correcting rotational velocity of tire, September 28 1999. US Patent 5,959,202.

[59] Jian Zhao, Jing Su, Bing Zhu, and Jingwei Shan. An indirect tpms algorithm based on tire resonance frequency estimated by ar model. *SAE International Journal of Passenger Cars-Mechanical Systems*, 9(1):99–107, 2016.

[60] Alfonso Silva, Jesús R Sánchez, Gerardo E Granados, Juan C Tudon-Martinez, and Jorge de J Lozoya-Santos. Comparative analysis in indirect tire pressure monitoring systems in vehicles. *IFAC-PapersOnLine*, 52(5):54–59, 2019.

[61] Takaji Umeno, Katsuhiro Asano, Hideki Ohashi, Masahiro Yonetani, Toshiharu Naitou, and Takeyasu Taguchi. Observer based estimation of parameter variations and its application to tyre pressure diagnosis. *Control Engineering Practice*, 9(6):639–645, 2001.

[62] Qi Zhang, Bo Liu, and Guofu Liu. Design of tire pressure monitoring system based on resonance frequency method. In *2009 IEEE/ASME International Conference on Advanced Intelligent Mechatronics*, pages 781–785. IEEE, 2009.

[63] Jiapeng Han, Yongli Sun, and Xiaofeng Tang. Research on tire pressure monitoring system based on the tire longitudinal stiffness. In *2008 IEEE International Conference on Automation and Logistics*, pages 1648–1652. IEEE, 2008.

[64] Sun-Woo Kang, Jung-Sik Kim, and Gi-Woo Kim. Road roughness estimation based on discrete kalman filter with unknown input. *Vehicle System Dynamics*, 57(10):1530–1544, 2019.

[65] Dong-Hoon Lee, Dal-Seong Yoon, and Gi-Woo Kim. New indirect tire pressure monitoring system enabled by adaptive extended kalman filtering of vehicle suspension systems. *Electronics*, 10(11):1359, 2021.

[66] NIRA Dynamics. Tire pressure indicator, the world-leading tire pressure monitoring system, 2023. https://niradynamics.se/tire-pressure-indicator/, last accessed 13 January 2023.

[67] Daniel Chindamo, Basilio Lenzo, and Marco Gadola. On the vehicle sideslip angle estimation: a literature review of methods, models, and innovations. *applied sciences*, 8(3):355, 2018.

[68] Rajesh Rajamani, Gridsada Phanomchoeng, Damrongrit Piyabongkarn, and Jae Y Lew. Algorithms for real-time estimation of individual wheel tire-road friction coefficients. *IEEE/ASME Transactions on Mechatronics*, 17(6):1183–1195, 2011.

[69] Giseo Park. Vehicle sideslip angle estimation based on interacting multiple model kalman filter using low-cost sensor fusion. *IEEE Transactions on Vehicular Technology*, 2022.

[70] Wuwei Chen, Dongkui Tan, and Linfeng Zhao. Vehicle sideslip angle and road friction estimation using online gradient descent algorithm. *IEEE Transactions on Vehicular Technology*, 67(12):11475–11485, 2018.

[71] Jing Li and Jiaxu Zhang. Vehicle sideslip angle estimation based on hybrid kalman filter. *Mathematical Problems in Engineering*, 2016, 2016.

[72] Angelo Bonfitto, Stefano Feraco, Andrea Tonoli, and Nicola Amati. Combined regression and classification artificial neural networks for sideslip angle estimation and road condition identification. *Vehicle system dynamics*, 58(11):1766–1787, 2020.

[73] Angelo Candeli, Gianmaria De Tommasi, Dario Giuseppe Lui, Adriano Mele, Stefania Santini, and Gaetano Tartaglione. A deep deterministic policy gradient learning approach to missile autopilot design. *IEEE Access*, 10:19685–19696, 2022.

[74] David M Bevly, Jihan Ryu, and J Christian Gerdes. Integrating ins sensors with gps measurements for continuous estimation of vehicle sideslip, roll, and tire cornering stiffness. *IEEE Transactions on Intelligent Transportation Systems*, 7(4):483–493, 2006.

[75] Jihan Ryu and J Christian Gerdes. Integrating inertial sensors with global positioning system (gps) for vehicle dynamics control. *J. Dyn. Sys., Meas., Control*, 126(2):243–254, 2004.

[76] Jonathan How, Nicholas Pohlman, and Chan-Woo Park. Gps estimation algorithms for precise velocity, slip and race-track position measurements. *SAE Transactions*, pages 2414–2421, 2002.

[77] Jong-Hwa Yoon and Huei Peng. Robust vehicle sideslip angle estimation through a disturbance rejection filter that integrates a magnetometer with gps. *IEEE Transactions on Intelligent Transportation Systems*, 15(1):191–204, 2013.

[78] J Kim. Identification of lateral tyre force dynamics using an extended kalman filter from experimental road test data. *Control Engineering Practice*, 17(3):357–367, 2009.

[79] Jamil Dakhlallah, Sébastien Glaser, Said Mammar, and Yazid Sebsadji. Tire-road forces estimation using extended kalman filter and sideslip angle evaluation. In *2008 American control conference*, pages 4597–4602. IEEE, 2008.

[80] Hongyan Guo, Dongpu Cao, Hong Chen, Chen Lv, Huaji Wang, and Siqi Yang. Vehicle dynamic state estimation: State of the art schemes and perspectives. *IEEE/CAA Journal of Automatica Sinica*, 5(2):418–431, 2018.

[81] Laura R Ray. Nonlinear tire force estimation and road friction identification: Simulation and experiments. *Automatica*, 33(10):1819–1833, 1997.

[82] Karl Berntorp and Stefano Di Cairano. Tire-stiffness and vehicle-state estimation based on noise-adaptive particle filtering. *IEEE Transactions on Control Systems Technology*, 27(3):1100–1114, 2018.

[83] Feliciano Di Biase, Basilio Lenzo, and Francesco Timpone. Vehicle sideslip angle estimation for a heavy-duty vehicle via extended kalman filter using a rational tyre model. *IEEE Access*, 8:142120–142130, 2020.

[84] Matt C Best, TJ Gordon, and PJ Dixon. An extended adaptive kalman filter for real-time state estimation of vehicle handling dynamics. *Vehicle System Dynamics*, 34(1):57–75, 2000.

[85] Henricus Albertus Petrus Blom. An efficient filter for abruptly changing systems. In *The 23rd IEEE Conference on Decision and Control*, pages 656–658. IEEE, 1984.

[86] Xianjian Jin and Guodong Yin. Estimation of lateral tire–road forces and sideslip angle for electric vehicles using interacting multiple model filter approach. *Journal of the Franklin Institute*, 352(2):686–707, 2015.

[87] Xianyao Ping, Shuo Cheng, Wei Yue, Yongchang Du, Xiangyu Wang, and Liang Li. Adaptive estimations of tyre–road friction coefficient and body's sideslip angle based on strong tracking and interactive multiple model theories. *Proceedings of the Institution of Mechanical Engineers, Part D: Journal of Automobile Engineering*, 234(14):3224–3238, 2020.

[88] Ying Xu, Wenjie Zhang, Wentao Tang, Chengxiang Liu, Rong Yang, Li He, and Yun Wang. Estimation of vehicle state based on imm-aukf. *Symmetry*, 14(2):222, 2022.

[89] Wan Wenkang, Feng Jingan, Song Bao, and Li Xinxin. Vehicle state estimation using interacting multiple model based on square root cubature kalman filter. *Applied Sciences*, 11(22):10772, 2021.

[90] SuoJun Hou, Wenbo Xu, and Gang Liu. Design of an interacting multiple model-cubature kalman filter approach for vehicle sideslip angle and tire forces estimation. *Mathematical Problems in Engineering*, 2019, 2019.

[91] H Tsunashima, M Murakami, and J Miyataa. Vehicle and road state estimation using interacting multiple model approach. *Vehicle System Dynamics*, 44(sup1):750–758, 2006.

[92] Henrique MT Menegaz and Simone Battistini. Switching multiple model filter for boost-phase missile tracking. *IEEE Transactions on Aerospace and Electronic Systems*, 54(5):2547–2553, 2018.

[93] Simone Battistini and Henrique MT Menegaz. Interacting multiple model unscented filter for tracking a ballistic missile during its boost phase. In *2017 IEEE Aerospace Conference*, pages 1–8. IEEE, 2017.

[94] Uwe Kiencke and Lars Nielsen. *Automotive Control Systems: For Engine, Driveline, and Vehicle*. Springer, 2005.

[95] Charles C MacAdam. An optimal preview control for linear systems. 1980.

[96] Rajesh Rajamani. *Vehicle dynamics and control*. Springer Science & Business Media, 2011.

[97] Michael Ben-Chaim, Efraim Shmerling, and Alon Kuperman. Analytic modeling of vehicle fuel consumption. *Energies*, 6(1):117–127, 2013.

[98] John B Heywood. *Internal combustion engine fundamentals*. McGraw-Hill Education, 2018.

[99] Alberto Boretti. Comparison of fuel economies of high efficiency diesel and hydrogen engines powering a compact car with a flywheel based kinetic energy recovery systems. *International Journal of Hydrogen Energy*, 35(16):8417–8424, 2010.

[100] HG Zhang, EH Wang, and BY Fan. A performance analysis of a novel system of a dual loop bottoming organic rankine cycle (orc) with a light-duty diesel engine. *Applied energy*, 102:1504–1513, 2013.

[101] Argonne National Laboratory. Conventional vehicle testing, 2023. https://www.anl.gov/taps/conventional-vehicle-testing, last accessed 03 January 2023.

[102] Simona Onori, Lorenzo Serrao, and Giorgio Rizzoni. Hybrid electric vehicles: Energy management strategies. 2016.

[103] Henrik Olsson, Karl Johan Åström, Carlos Canudas De Wit, Magnus Gäfvert, and Pablo Lischinsky. Friction models and friction compensation. *Eur. J. Control*, 4(3):176–195, 1998.

[104] Georg Rill and Abel Arrieta Castro. *Road vehicle dynamics: fundamentals and modeling with MATLAB®*. CRC Press, 2020.

[105] Jon D Demerly and Kamal Youcef-Toumi. Non-linear analysis of vehicle dynamics (navdyn): A reduced order model for vehicle handling analysis. Technical report, SAE Technical Paper, 2000.

[106] UK Vehicle certification agency. Fuel consumption and co_2, 2023. https://www.vehicle-certification-agency.gov.uk/, last accessed 08 January 2023.

[107] Michał Jasiński. A generic validation scheme for real-time capable automotive radar sensor models integrated into an autonomous driving simulator. In *2019 24th International Conference on Methods and Models in Automation and Robotics (MMAR)*, pages 612–617. IEEE, 2019.

[108] Rolf Isermann. *Mechatronic systems: fundamentals*. Springer Science & Business Media, 2007.

[109] Alan Neville Gent and Joseph D Walter. Pneumatic tire. 2006.

[110] Chandrashekhar S Dharankar, Mahesh Kumar Hada, and Sunil Chandel. Numerical generation of road profile through spectral description for simulation of vehicle suspension. *Journal of the Brazilian Society of Mechanical Sciences and Engineering*, 39(6):1957–1967, 2017.

[111] Werner Schiehlen. White noise excitation of road vehicle structures. *Sadhana*, 31(4):487–503, 2006.

[112] Feng Tyan, Yu-Fen Hong, Shun-Hsu Tu, Wes S Jeng, et al. Generation of random road profiles. *Journal of Advanced Engineering*, 4(2):1373–1378, 2009.

[113] B Goenaga, L Fuentes, and O Mora. Evaluation of the methodologies used to generate random pavement profiles based on the power spectral density: An approach based on the international roughness index. *Ingeniería e Investigación*, 37(1):49–57, 2017.

[114] *ISO (International Organization for Standardization) 8608:2016, Mechanical vibration — Road surface profiles — Reporting of measured data*. Available online: https://www.iso.org/standard/71202.html (accessed on 18 Oct 2022).

[115] Tadas Lenkutis, Aurimas Čerškus, Nikolaj Šešok, Andrius Dzedzickis, and Vytautas Bučinskas. Road surface profile synthesis: assessment of suitability for simulation. *Symmetry*, 13(1):68, 2020.

[116] Claude E Shannon. Communication in the presence of noise. *Proceedings of the IRE*, 37(1):10–21, 1949.

[117] DA Crolla and MBA Abdel-Hady. Active suspension control; performance comparisons using control laws applied to a full vehicle model. *Vehicle System Dynamics*, 20(2):107–120, 1991.

[118] Lei Zuo and Samir A Nayfeh. Structured h2 optimization of vehicle suspensions based on multi-wheel models. *Vehicle system dynamics*, 40(5):351–371, 2003.

[119] Niclas Persson. *Event based sampling with application to spectral estimation*. Citeseer, 2002.

[120] Carlo Poloni and Valentino Pediroda. Ga coupled with computationally expensive simulations: tools to improve efficiency. 1997.

[121] SS Kelkar, LL Grigsby, and J Langsner. An extension of parseval's theorem and its use in calculating transient energy in the frequency domain. *IEEE Transactions on Industrial Electronics*, (1):42–45, 1983.

[122] Sankaranarayanan Velupillai and Levent Guvenc. Tire pressure monitoring [applications of control]. *IEEE Control systems magazine*, 27(6):22–25, 2007.

[123] Ajit G Mohite and Anirban C Mitra. Development of linear and non-linear vehicle suspension model. *Materials Today: Proceedings*, 5(2):4317–4326, 2018.

[124] Michael W Sayers. The little book of profiling: basic information about measuring and interpreting road profiles. Technical report, University of Michigan, Ann Arbor, Transportation Research Institute, 1998.

[125] Jorge Hurel, Anthony Mandow, and Alfonso García-Cerezo. Kinematic and dynamic analysis of the mcpherson suspension with a planar quarter-car model. *Vehicle System Dynamics*, 51(9):1422–1437, 2013.

[126] C Gavin McGee, Muhammad Haroon, Douglas E Adams, and Yiu Wah Luk. A frequency domain technique for characterizing nonlinearities in a tire-vehicle suspension system. *J. Vib. Acoust.*, 127(1):61–76, 2005.

[127] Mahesh P Nagarkar, Gahininath J Vikhe Patil, and Rahul N Zaware Patil. Optimization of nonlinear quarter car suspension–seat–driver model. *Journal of advanced research*, 7(6):991–1007, 2016.

[128] Jean Lemaitre. *Handbook of materials behavior models, three-volume set: nonlinear models and properties*. Elsevier, 2001.

[129] Massimo Guiggiani. The science of vehicle dynamics. *Pisa, Italy: Springer Netherlands*, page 15, 2014.

[130] Damien Maher and Paul Young. An insight into linear quarter car model accuracy. *Vehicle system dynamics*, 49(3):463–480, 2011.

[131] Jo Yung Wong. *Theory of ground vehicles*. John Wiley & Sons, 2022.

[132] RK Taylor, LL Bashford, and MD Schrock. Methods for measuring vertical tire stiffness. *Transactions of the ASAE*, 43(6):1415–1419, 2000.

[133] A Galip Ulsoy, Huei Peng, and Melih Çakmakci. *Automotive control systems*. Cambridge University Press, 2012.

[134] Devyani Varshney, Mani Bhushan, and Sachin C Patwardhan. State and parameter estimation using extended kitanidis kalman filter. *Journal of Process Control*, 76:98–111, 2019.

[135] Claudio Maino, Daniela Misul, Alessia Musa, and Ezio Spessa. Optimal mesh discretization of the dynamic programming for hybrid electric vehicles. *Applied Energy*, 292:116920, 2021.

[136] A Gimelli, A Luongo, and M Muccillo. Efficiency and cost optimization of a regenerative organic rankine cycle power plant through the multi-objective approach. *Applied thermal engineering*, 114:601–610, 2017.

[137] Renato Brancati, Massimiliano Muccillo, and Francesco Tufano. Crank mechanism friction modeling for control-oriented applications. In *The International Conference of IFToMM ITALY*, pages 729–737. Springer, 2020.

[138] Alberto Petrillo, Maria Vittoria Prati, Stefania Santini, and Francesco Tufano. Improving the nox reduction performance of an euro vi d scr system in real-world condition via nonlinear model predictive control. *International Journal of Engine Research*, page 14680874211066217, 2021.

[139] Christos E Papadopoulos and Hoi Yeung. Uncertainty estimation and monte carlo simulation method. *Flow Measurement and Instrumentation*, 12(4):291–298, 2001.

[140] Francesco De Nola, Giovanni Giardiello, Barbara Noviello, and Francesco Tufano. A control-oriented and physics-based model of the engine crank mechanism friction for the base calibration: Parametric analysis. In *AIP Conference Proceedings*, volume 2191, page 020060. AIP Publishing LLC, 2019.

[141] Bradley Harding, Christophe Tremblay, and Denis Cousineau. Standard errors: A review and evaluation of standard error estimators using monte carlo simulations. *The Quantitative Methods for Psychology*, 10(2):107–123, 2014.

[142] Robert L Harrison. Introduction to monte carlo simulation. In *AIP conference proceedings*, volume 1204, pages 17–21. American Institute of Physics, 2010.

[143] Quanbo Ge, Teng Shao, Zhansheng Duan, and Chenglin Wen. Performance analysis of the kalman filter with mismatched noise covariances. *IEEE Transactions on Automatic Control*, 61(12):4014–4019, 2016.

[144] Filip Šroubek, Michal Šorel, and Josef Žák. Precise international roughness index calculation. *International Journal of Pavement Research and Technology*, 15(6):1413–1419, 2022.

[145] Guo Xie, Lanlan Sun, Tao Wen, Xinhong Hei, and Fucai Qian. Adaptive transition probability matrix-based parallel imm algorithm. *IEEE Transactions on Systems, Man, and Cybernetics: Systems*, 51(5):2980–2989, 2019.

[146] Zhi Guo, CY Dong, YL Cai, and Z Yu. Time-varying transition probability based imm-srckf algorithm for maneuvering target tracking. *Systems Engineering and Electronics*, 37(1):24–30, 2015.

[147] Elvis Villano, Basilio Lenzo, and Aleksandr Sakhnevych. Cross-combined ukf for vehicle sideslip angle estimation with a modified dugoff tire model: design and experimental results. *Meccanica*, 56(11):2653–2668, 2021.

[148] Howard Dugoff, Paul S Fancher, and Leonard Segel. An analysis of tire traction properties and their influence on vehicle dynamic performance. *SAE transactions*, pages 1219–1243, 1970.

[149] Henrique MT Menegaz, João Y Ishihara, Geovany A Borges, and Alessandro N Vargas. A systematization of the unscented kalman filter theory. *IEEE Transactions on automatic control*, 60(10):2583–2598, 2015.

[150] Simone Battistini, Renato Brancati, Dario Giuseppe Lui, and Francesco Tufano. Enhancing ads and adas under critical road conditions through vehicle sideslip angle estimation via unscented kalman filter-based interacting multiple model approach. In *The International Conference of IFToMM ITALY*, pages 450–460. Springer, 2022.

[151] Vladimír Panáček, Marek Semela, Vladimír Adamec, and Barbora Schüllerová. Impact of usable coefficient of adhesion between tyre and road surface by modern vehicle on its dynamics while driving and braking in the curve. *Transport*, 31(2):142–146, 2016.

[152] Michele Russo, Riccardo Russo, and Agsotino Volpe. Car parameters identification by handling manoeuvres. *Vehicle System Dynamics*, 34(6):423–436, 2000.